SEISMIC MODELING AND IMAGING OF REALISTIC EARTH MODELS USING NEW FULL-WAVE PHASE-SHIFT APPROACH

A Dissertation

Presented to

the Faculty of the Department of Physics

University of Houston

In Partial Fulfillment

of the Requirements for the Degree

Doctor of Philosophy

By

Nelka Chithrani Wijesinghe

May 2014

SEISMIC MODELING AND IMAGING OF REALISTIC EARTH MODELS USING NEW FULL-WAVE PHASE-SHIFT APPROACH

Nelka Chithrani Wijesinghe

APPROVED:

Prof. Donald J. Kouri
Dept. of Physics

Prof. Gemunu Gunaratne
Dept. of Physics

Prof. Wu-Pei Su
Dept. of Physics

Prof. George Reiter
Dept. of Physics

Prof. Evgeny Chesnokov
Dept. of Earth and Atmospheric Sciences

Dean, College of Natural Sciences and Mathematics

Acknowledgments

First of all, I would like to express my sincere gratitude to my research advisor, Professor Donald J. Kouri for getting me started on this interesting research topic and being a wonderful guide throughout my graduate studies. His valuable advice, enthusiastic encouragement, support, mathematical experience, and also his many useful discussions have been a great help for me to broaden my knowledge and understanding in seismic exploration.

Next, I would like to express my special thanks to Dr. Michael D'mello from Intel Corporation for his invaluable discussions and suggestions on computational physics.

A very special thank also goes to Dr. Anne Cecile-Lesage for her guidance and willing support in completing this thesis.

I would like to express my appreciation to Professors Gemunu Gunarathne, Wu-Pei Su, George Reiter, Evgeny Chesnokov, and Bernhard Bodmann for their valuable discussions while serving on my thesis committee.

I am also grateful to Total and Petroleum Geo-Services (PGS) for sponsoring this work and providing access to their high performance computer resources necessary for this research.

I would also like to extend my thanks to Dr. Kaushik Maji for his support in initiating this work. I would also like to thank the fellow students in our research group for their help .

On a more personal note, I would like to thank my husband Iroshan for his patience and whole-hearted support throughout my studies and especially during my dissertation work.

Finally, I would like to thank my family, especially my parents and my brother, for their persistent encouragement and love. Without their support I certainly not be where I am today.

SEISMIC MODELING AND IMAGING OF REALISTIC EARTH MODELS USING NEW FULL-WAVE PHASE-SHIFT APPROACH

An Abstract of a Dissertation

Presented to

the Faculty of the Department of Physics

University of Houston

In Partial Fulfillment

of the Requirements for the Degree

Doctor of Philosophy

By

Nelka Chithrani Wijesinghe

May 2014

Abstract

Seismic modeling is a valuable tool for seismic interpretation of oil and gas reservoirs and is an essential part of seismic inversion algorithms. In this thesis, we have developed and verified the new full-wave phase-shift (FWPS) approach for solving seismic modeling and imaging problems. FWPS approach is based on a new way to generalize the "one-way" acoustic wave equation using a phase-shift structure. Our approach solves the full acoustic wave equation by separating the problem into an equation consisting of two coupled first-order partial differential equations for wave propagation in depth, in which the initial waves are purely one-way, but solving the equations for downgoing initial waves and then for upgoing initial waves, retaining the full two-way nature of the Helmholtz equation. This produces a complete set of linearly independent solutions, that is used to construct the correct, causal full wave solution that includes waves propagating both up and down. The initial conditions for the modeling problem are generated by solving the Lippmann-Schwinger integral equation formally, in a non-iterative fashion and converting the problem into a Volterra integral equation of the second kind. Reflection and wraparound from boundaries are effectively dealt with employing correct absorbing boundary conditions.

We validate the new FWPS method by applying it to forward modeling and inversion. Time snapshot results are given for standard velocity models, as well as a realistic earth velocity model. We compare the realistic earth velocity model results from new FWPS approach to those obtained by finite differences (FD), with correct scattering boundary conditions imposed. We have stabilized our results by using the Feshbach projection-operator technique to remove all the nonphysical exponentially growing evanescent waves, while retaining all of the propagating waves and exponentially decaying evanescent waves. Our approach is easily parallelized to achieve approximate N^2 scaling, where N is the number of coupled equations. We discuss the parallelization techniques used to optimize the algorithm and improve the computational cost. We show the presence of evanescent waves in a realistic earth velocity model by comparing the reflection matrix both with and without decaying evanescent waves.

Contents

List of Figures

List of Tables

Chapter 1

Introduction

1.1 Petroleum Seismology

The main motivation behind petroleum seismology is to have a clear and accurate map of the subsurface structure in the area under exploration before any attempt to drill. This structural map is important to the oil and gas industry because it plays a key role in determining where to drill for hydrocarbon reserves which, in turn can have an enormous global economic, environmental, and political impact. The petroleum industry employs reflection seismology as an aid to study and map the subsurface, which enables it to locate, study and monitor potential underground hydrocarbon reservoirs. Seismology refers to the study of how energy, in the form of seismic waves, propagates through layers of earth's crust and interacts differently with various types of underground formations.

Seismic exploration plays a key role in defining and characterizing existing reservoir wells and in discovering new oil and gas reservoirs. The first known seismic exploration trials were conducted by John C. Karcher and colleagues, who performed a primitive seismic survey and mapped a shallow limestone bed at Belle Isle, Oklahoma in the summer of 1921. Since then, seismic technologies have evolved into ever more sophisticated techniques through the use of digital computer processing, improved energy sources, advanced acoustic receivers (multi-component), three-dimensional, and four-dimensional (time-lapse) seismic surveys.

1.2 Seismic Acquisition

As previously mentioned, petroleum seismology is a method of locating commercial accumulations of hydrocarbon reservoirs by seismically imaging the earth's reflectivity distribution. Oil and gas, being less dense than water, tend to rise through connected pore spaces in the rock until they encounter an impermeable barrier where they become trapped [1]. The exploration for hydrocarbon resources mainly takes place in sedimentary rocks located in the upper few kilometers of the Earth's crust. In a seismic exploration procedure, a manufactured and controlled source of seismic energy generates seismic waves, known as incident waves, that propagate through the subsurface until encountering an interface with significantly different physical properties (*e.g.*, velocity and/or density). Then, a fraction of the source energy is reflected towards the earth's surface to be recorded and acquired as data by a receiver placed on or near the earth's surface. The reflected wave is recorded by the receiver in terms of the Earth's vertical particle velocity (or some function thereof) or pressure change over a certain time span, denoted as a seismic trace. The reflected wave contains information about the source that created it, the medium that the wave has traveled through, and the inhomogeneities (or reflectors) that caused part of the incident wave to return to the surface.

This procedure can be carried out on land or in a marine environment, in which case they are referred to as on-shore and off-shore surveys, respectively. Each of these types of seismic acquisition calls for a proper set of devices to be employed as sources and receivers that best match the type of environment being surveyed. For example, in an on-shore acquisition, a vibrator truck (known as vibroseis) or an explosive device (*e.g.*, dynamite) that generates seismic waves in the earth, can be used as a source and a geophone (device sensitive to ground motion) can be used as receiver. The vibrator truck continuously shakes the ground, starting from a low frequency rumble at about 5 Hz and then progressively sweeping to higher frequencies up to 150 Hz. The sweep time ranges from 20 s to 40 s or so, and the recorded signal from the geophone is cross-correlated with the vibrator truck signal to produce an impulsive source wavelet. Figure 1.1 is a cartoon of an on-shore acquisition.

In an off-shore survey, as shown on Fig. 1.2, a proper source can be an air-gun, which is a device that releases bursts of highly-pressurized air into the water; a proper receiver is an hydrophone. Geophones and hydrophones both measure the earth's or water's response in the form of particle velocity, acceleration, and pressure change. They convert particle movement or acceleration into an electric pulse that is recorded along with it's arrival time. The amplitude of the recorded pulse in the

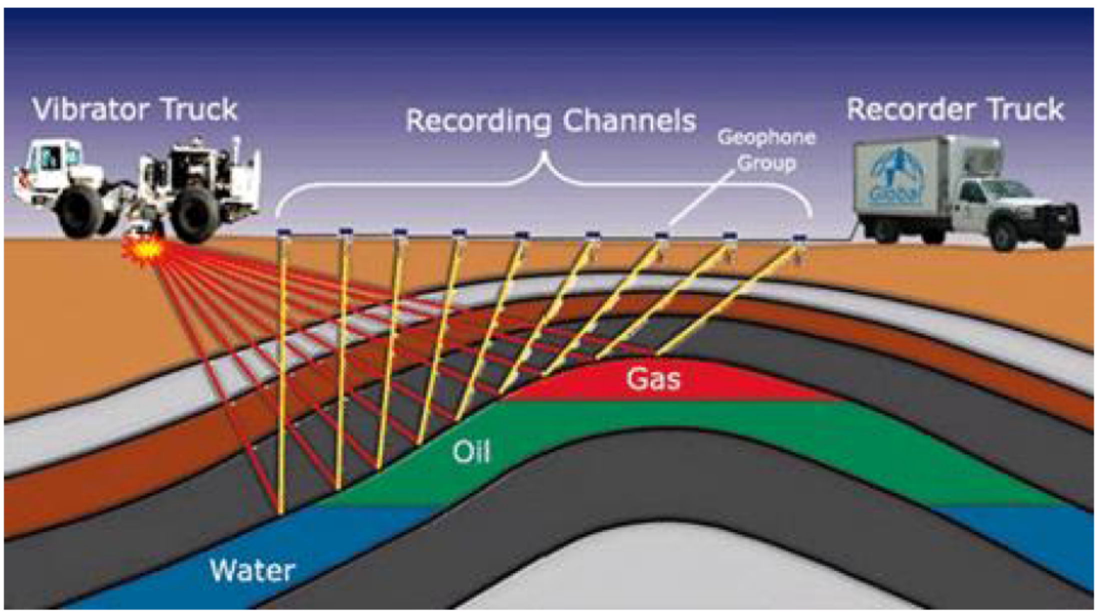

Figure 1.1: On-shore seismic survey that results from a seismic wave from a vibrator truck into a recorder truck containing nine geophones [2].

geophone or hydrophone is proportional to the magnitude of the particle velocity or acceleration.

The recorded seismic data are processed to reveal information about the Earth's subsurface. Ultimately, this information is interpreted to deduce the geological structure and the size and type of possible hydrocarbon accumulations. The quality of the processed seismic data has a direct impact on the ability to find and describe reservoirs. False or inaccurate reservoir prediction can lead to wells drilled in the wrong location; an expensive mistake given that an off-shore deep water well can cost more than 500 million dollars. Such high stakes motivate research into new, more effective seismic data processing algorithms. The two main methods of seismic data processing are seismic modeling and seismic migration. Seismic modeling and seismic migration are, in some sense, inverses of each other [4]. Modeling describes the forward process of propagating waves from sources to scatterers to receivers, generating seismic data. Migration attempts to undo the wave propagation effects to produce an image of the earth.

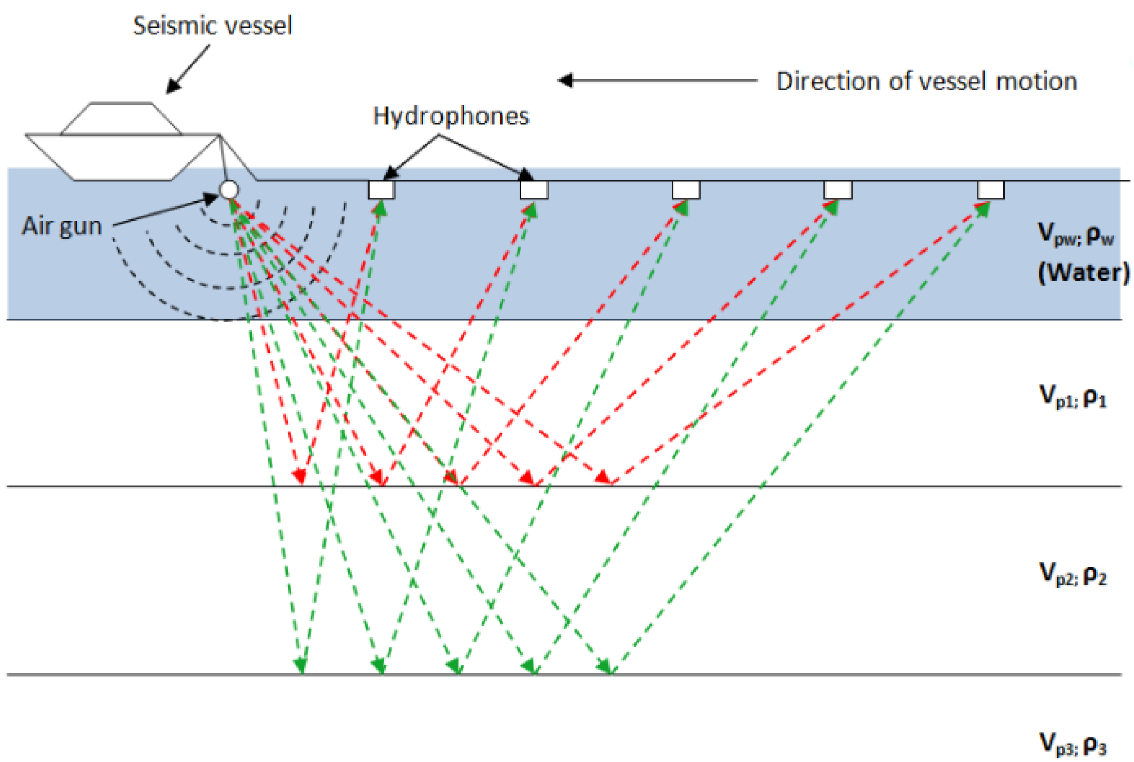

Figure 1.2: Off-shore seismic survey that results from a single shot from an airgun into a streamer containing five hydrophones [3].

1.2.1 Seismic Migration

Migration is a wave-equation-based process used in seismic processing to obtain a model of the subsurface. It involves geometric moving of scattered signals to show the layer boundary or other structure where the seismic wave was reflected rather than where it is picked up. Migration was first used in the 1920's, and today, it has evolved into many variations [5, 6, 7]. Two of the most important migration methods are pre-stack and post-stack migration.

Pre-stack migration is the process in which seismic data is "back propagated" through a velocity model before the stacking sequence occurs. The usual form of pre-stack migration is depth migration. Pre-stack migration requires the information about velocities of the earth's layers. Once the user back propagates the data, there will be some error in the image caused by dipping reflectors or diffractions. The pre-stack depth migration will adjust the model according to the velocities given. Pre-stack migration is often applied only when the layers being observed have complicated velocity profiles, or when the structures are just too complex to see with post-stack migration. Pre-stack migration is an important tool in modeling salt diapirs because of their complexity and this has immediate benefits if the resolution can pick up any hydrocarbons trapped by the diapir.

Post-stack migration is the process of migration in which the data is stacked before it has been migrated. This process is more popular for many reasons, mainly because of its reasonable cost compared to pre-stack migration. As in pre-stack migration, post stack migration is based on the idea that all data elements represent either primary reflections or diffractions. This is done by using an operation involving the rearrangement of seismic information so that reflections and diffractions are plotted at their true locations. The reason that migration is needed is due to the fact that variable velocities and dipping horizons cause the data to record surface positions differently from their subsurface positions. A disadvantage of using post-stack migration compared to pre-stack migration is that it does not give as clear results as pre-stack. Post-stack migration usually gives good results though, when the dip is small and where events with different dips do not interfere on the migrated section.

1.2.2 Seismic Modeling

Seismic modeling is a technique for simulating wave propagation in the Earth. It involves solving the acoustic wave equation in order to predict data that would be recorded by a set of sensors for an assumed velocity model of the subsurface. Seismic modeling is a valuable tool for seismic interpretation and is a essential part of seismic inversion algorithms. Seismic modeling methods can be classified into three main categories [8]: ray-tracing methods, integral-equation methods, and direct methods.

Ray-tracing methods (asymptotic methods) have been frequently used in seismic modeling and imaging. In these methods, the wavefield is considered as a series of certain events, with characteristic travel time and associated amplitude. Raypaths are traced either by solving a certain differential equation that can be extracted from seismic wave equation or by using analytic results within layers and explicit Snell's law calculations (interface based models). They do not take into account the full wavefield [9]; therefore, these methods are approximative. Typically, the full wave equation is replaced by a single, first-order partial differential equation, by factoring the second-order equation, neglecting the effects due to the local variation of the sound velocity. Consequently, only waves traveling in one direction are included. Thus, they are also called "one-way" equations. The one-way equations were originally introduced by Claerbout [10, 11].

The second group of seismic modeling methods are integral-equation methods. Integral-equation methods of seismic modeling are based on an integral representation of the seismic wavefield spreading from point sources (Huygens' principal). There are two forms of integral methods: volume integral and boundary integral. The integral-equation methods are very useful in the derivation of imaging methods based on the Born approximation, due to their particular analytical character (Cohen, 1986 [12] and Weglein *et al.*, 2003 [13]).

The last category of seismic forward modeling methods are the direct methods that involve numerical solution of wave equation. Such methods are also called full-wave equation methods since they implicitly provide the full wave field. Direct methods such as Finite Difference (FD) (Alterman & Karal, 1968 [14], Claerbout, 1985 [11], and Virieux, 1986 [15]) and finite element (Huygens, 1987 [16], Marfurt, 1984 [17], and De Basabe & Sen, 2009 [18]) require the model to be discretized into a finite number of points and therefore sometimes are called grid methods. Psudo-spectral methods (Gazdag, 1981 [19] and Kosloff *et al.*, 1982 [20]) are also examples of the direct method. Direct methods have the ability to accurately model seismic waves in arbitrary heterogeneous media. The primary disadvantage is that these methods are extremely expensive and time consuming compared to the other two methods.

Seismic modeling is useful in a wide range of applications in exploration and earthquake seismology. It plays an important role in almost all aspects of exploration seismology such as seismic data acquisition, processing, interpretation, and reservoir characterization. It increases the reliability of seismic data analysis. In seismic acquisition, seismic forward modeling reduces the risk in seismic exploration by providing quantitative information to design better surveys (*e.g.,* Gjystdal *et al.*, 2007 [21], Laurain *et al.*, 2004 [22], and Robertsson *et al.*, 2007 [23]). In complex geological settings seismic forward modeling can be used to test different acquisition parameters and subsurface models to achieve the optimum data collection strategy. Seismic modeling has been used to test different processing algorithms and flows. Another important role of seismic modeling is to calibrate migration methods (Gray *et al.*, 2001 [24]). Seismic forward modeling can also be used to relate the response of an interpreted geologic model to real data. Also it can be applied in the development of geological models to investigate the structural and stratigraphic problems faced during the seismic interpretation (Chopra & Sayers, 2009 [25]).

1.3 One-way Wave Equation Downward-continuation Seismic Modeling and Migration Methods

In recent years, wavefield downward-continuation seismic methods have been widely applied as the available computational power has steadily increased. Exploration for oil and gas has extended to areas with more complex structures, exhibiting strong lateral variations in seismic velocity. Wavefield downward-continuation enables geophysicists to predict wavefields in the subsurface by propagating a seismic wavefield through an appropriate subsurface velocity model. The essence of wavefield downward-continuation modeling and depth migration methods is a recursive wavefield extrapolation based on one-way wave equations [26]. The term recursive implies that the output wavefield from the last extrapolation is used as the input wavefield for the next extrapolation. Wavefield downward-continuation methods typically show a superior capability for imaging complex structures compared with non-recursive ray-based methods such as diffraction-stack or Kirchhoff migration. It is widely accepted that recursive extrapolators provide a more accurate solution to the wave equation over a wider range of velocities and seismic frequencies [27].

Many algorithms have been developed that fall into the category of recursive wavefield extrapolation. In 1972 Claerbout [10, 11] developed the implicit finite-difference method which used a one-way wave equation which allows energy to propagate only in one-way. This is of course an approximation and breaks down for strongly varying velocity models. The explicit space-frequency extrapolation (often called the f-x) method was introduced by Berkhout in 1982 [26]. He showed that the forward seismic modeling can be elegantly described by a matrix equation, using separate operators for downward and upward traveling waves. Using this model, inverse extrapolation involves one matrix inversion procedure to compensate for the downward propagation effects and one matrix inversion procedure to compensate for the upward propagation effects. He concluded that explicit methods are simple and most suitable for three-dimensional applications.

In 1984, Gazdag and Sguazzero [28] introduced the phase-shift plus-interpolation method (PSPI). Their wave extrapolation procedure consisted of two steps; the wavefield is extrapolated by the phase-shift method using laterally uniform velocity fields and the actual wavefield is computed by interpolation from the reference wavefields. They claimed that PSPI method is unconditionally stable and lends itself conveniently to migration of three-dimensional data.

In 1990 Stoffa *et al.* [29] introduced the split-step Fourier method which takes into account laterally varying velocity by defining a reference slowness (reciprocal of velocity) as the mean slowness in the migration interval and a perturbation term that is spatially varying. However, this method is theoretically accurate only when there are no rapid lateral slowness variations combined with steep angles of propagation.

In 1999 Margrave and Ferguson [30] introduced the non-stationary phase-shift method (NSPI). In their method the symmetric operator is used in a recursive wavefield extrapolation to compute incident and reflected wavefields at any desired depth. In 2008 Shragge [31] presented a novel approach in which downward-continuation was implemented in Riemannian coordinates in the presence of complex geology.

In 2009 Al-Saleh *et al.* [32] introduced a direct downward-continuation method using explicit wavefield extrapolation. Their method downward continues data directly from topography using a recursive space-frequency explicit wavefield-extrapolation method. They confirmed the method's effectiveness in imaging shallow and deep structures beneath rugged topography. Their algorithm is claimed to treat strong lateral velocity variations by using the velocity value at each spatial position to build the wavefield extrapolator in which the depth step usually is kept fixed.

1.4 Generalized Phase-shift Method

A basic part of seismic migration is downward continuation of surface data into the subsurface. The phase-shift method introduced by Gazdag in 1978 [33] for wavefield extrapolation has played a very important role in exploration seismic. Gazdag's method is most useful in situations when the velocity model is function of the depth only, *i.e.*, it is independent of the coordinates transverse to the direction of extrapolation. Therefore, the phase-shift method, as developed, is not theoretically able to treat lateral velocity variations [26]. In a phase-shift method, propagation is modeled by the scalar wave equation, and Fourier transforms are used to decompose the seismic wavefield into plane waves that are exptrapolated from one depth to another by a phase-shift. The Fourier transformed and phase-shifted wavefield is then inverse Fourier transformed and used to estimate reflectivity. For any extrapolation step, the velocity must remain constant in all coordinates. Velocity variation in depth is accommodated by segmenting the subsurface into horizontal intervals of constant velocity and extrapolating through these layers recursively.

In 1987, Kosloff and Kessler [34] showed how the phase-shift method can be generalized for an arbitrary velocity structure in the space-frequency domain. It is instructive to understand how the phase-shift method of Kosloff and Kessler works and how it can be implemented in both the space-frequency domain and wavenumber-frequency domain. Therefore, we highlight the work of Kosloff and Kessler [34] on the phase-shift method.

The Kosloff-Kessler phase-shift method is based on the solution of the temporally transformed acoustic wave equation

$$\frac{\partial^2}{\partial z^2}\tilde{P}(x,z,\omega) = \left(-\frac{\omega^2}{c^2} - \frac{\partial^2}{\partial x^2}\right)\tilde{P}(x,z,\omega), \tag{1.1}$$

where x and z denote horizontal and vertical Cartesian coordinates respectively, $\tilde{P}(x,z,\omega)$ denotes the space-frequency domain pressure field, ω is the angular frequency, and $c(x,z)$ is the velocity field. As suggested by Kosloff and Baysal in 1983 [35], it is convenient to recast Eqn. (1.1) as a set of two first-order coupled equations given by

$$\frac{\partial}{\partial z}\begin{pmatrix} \tilde{P} \\ \frac{\partial \tilde{P}}{\partial z} \end{pmatrix} = \begin{pmatrix} 0 & 1 \\ -\frac{\omega^2}{c^2} - \frac{\partial^2}{\partial x^2} & 0 \end{pmatrix}\begin{pmatrix} \tilde{P} \\ \frac{\partial \tilde{P}}{\partial z} \end{pmatrix}. \tag{1.2}$$

The downward continuation in the migration consists of the solution of Eqn. (1.2) for each frequency at all depths under the initial conditions of the values of $\tilde{P}$ and $\frac{\partial \tilde{P}}{\partial z}$ at the surface $z = 0$ [35]. Equation (1.2) can be expressed in a more compact form

$$\frac{\partial}{\partial z}\begin{pmatrix}\tilde{P} \\ \frac{\partial \tilde{P}}{\partial z}\end{pmatrix} = \left[\tilde{A}\right]\begin{pmatrix}\tilde{P} \\ \frac{\partial \tilde{P}}{\partial z}\end{pmatrix} \tag{1.3}$$

where $[\tilde{P}, \frac{\partial \tilde{P}}{\partial z}]$ denotes a column vector of length $2N_x$ containing first the N_x pressures $\tilde{P}(idx, z, \omega)$ and then the N_x pressure derivatives $\frac{\partial \tilde{P}(idx,z,\omega)}{\partial z}$, for $i = 0, 1, ..., N_x - 1$. The matrix $[\tilde{A}]$ is obtained by comparison to Eqn. (1.2). As with the ordinary phase-shift method, the solution here is propagated in depth increments. Within each increment z to $z + dz$, the velocity is assumed to be invariant in the vertical direction although it may vary horizontally. The solution of Eqn. (1.3) can then be written as

$$\frac{\partial}{\partial z}\begin{pmatrix}\tilde{P} \\ \frac{\partial \tilde{P}}{\partial z}\end{pmatrix}_{z+dz} = \exp[\tilde{A}dz]\begin{pmatrix}\tilde{P} \\ \frac{\partial \tilde{P}}{\partial z}\end{pmatrix}_{z} . \tag{1.4}$$

The solution (1.4) embodies a phase-shift of the eigenvector coefficients of $\tilde{A}$. The evaluation of $\exp[\tilde{A}dz]$ involves approximating $\tilde{A}$ to obtain a phase factor. The exponential is computed via $\exp[i\tilde{a}dz]$ with $\tilde{a}$ being a real, diagonal matrix. This leads to the Kosloff-Kessler generalized phase-shift approach. When the velocity structure is varying arbitrarily, the eigenvalues and eigenvectors of $\tilde{A}$ can no longer be obtained by inspection. It would therefore seem that a matrix diagonalization would have to be performed before each propagation. Kosloff *et al.* used the Chebychev expansion method by Tal-Ezer in 1986 [36]. Their work indicates how the calculation of a matrix exponential can be done without having to resort to expensive matrix diagonalizations. However, the Chebychev expansion method is unstable with absorbing boundaries and also quite expensive, so that it is not suitable for the realistic velocity models used in seismic exploration.

1.5 New Full-wave Phase-shift Approach to Solve the Helmholtz Wave Equation

In 2012 Kouri *et al.* [37] introduced a new and explicit method for solving the scattering problem, using the Helmholtz wave equation, based on a novel method to generalize the "one-way" acoustic wave equation. In this method, the full two-way nature of the Helmholtz equation is included but the equation is converted into a one-way form using a generalized phase-shift structure explained in the previous section. The method consists of two coupled, first-order partial differential equations for wave propagation in the depth variable z. Therefore, this new method is called new full-wave phase-shift approach and it solves the full acoustic wave equation by separating the problem into an equation in which the initial waves are purely one-way, but solving the equations for downgoing initial waves and then again for upgoing initial waves. This produces a complete set of linearly independent solutions, in terms of which one can readily construct the correct, causal full wave solution that includes wave propagating both up and down.

Our approach makes use of some early ideas on the non-iterative solution of the Lippmann-Schwinger equation in quantum scattering (Sams *et al.* [38, 39]). Following the early work of Kosloff and Kessler [34], the second-order Helmholtz wave equation is transferred into two coupled first-order differential equations in the depth variable z as in Eqn. (1.2). Then, a new vector $\mathbf{W}$ is introduced for the pressure and it's derivative,

$$\mathbf{W} = \begin{pmatrix} \tilde{P} \\ \tilde{Q} \end{pmatrix} \tag{1.5}$$

where $\tilde{Q} = \frac{\partial \tilde{P}}{\partial z}$. The coupled, first-order equations can be written in the following form:

$$\frac{\partial}{\partial z}\mathbf{W} = \begin{pmatrix} 0 & 1 \\ -\frac{\omega^2}{c^2} - \frac{\partial^2}{\partial x^2} & 0 \end{pmatrix}\mathbf{W}. \tag{1.6}$$

Kouri *et al.* [40] proposed a new splitting for the Eqn. (1.6) employing the modified Cayley method approach. More precisely, the wave operator in Eqn. (1.6) is decomposed into the sum of two matrices: the first one is a propagator in a reference velocity medium, and the second one is a perturbation which takes into account the vertical and lateral variation of the velocity. This is done by addition and subtraction of the term $-\frac{\omega^2}{c_0^2}$, where c_0 is locally constant reference velocity. Then, Eqn. (1.6) can be written as

$$\frac{\partial}{\partial z}\begin{pmatrix} \tilde{P} \\ \tilde{Q} \end{pmatrix} = \begin{pmatrix} 0 & 1 \\ -\frac{\omega^2}{c_0^2} - \frac{\partial^2}{\partial x^2} & 0 \end{pmatrix}\begin{pmatrix} \tilde{P} \\ \tilde{Q} \end{pmatrix} + \begin{pmatrix} 0 & 0 \\ -\frac{\omega^2}{c^2} + \frac{\omega^2}{c_0^2} & 0 \end{pmatrix}\begin{pmatrix} \tilde{P} \\ \tilde{Q} \end{pmatrix}. \tag{1.7}$$

Now Eqn. (1.7) can be represented as

$$\frac{\partial}{\partial z}\mathbf{W} = \mathbf{MW} + \mathbf{VW}, \tag{1.8}$$

where,

$$\mathbf{M} = \begin{pmatrix} 0 & 1 \\ -\frac{\omega^2}{c_0^2} - \frac{\partial^2}{\partial x^2} & 0 \end{pmatrix}, \quad \mathbf{V} = \begin{pmatrix} 0 & 0 \\ -\frac{\omega^2}{c^2} + \frac{\omega^2}{c_0^2} & 0 \end{pmatrix}, \text{ and } \mathbf{W} = \begin{pmatrix} \tilde{P} \\ \tilde{Q} \end{pmatrix}.$$

Solving the linear, first-order partial differential equations in Eqn. (1.8) we can obtain the simplest new full-wave phase-shift solution

$$\mathbf{W}(z+\Delta z) = \left(\mathbf{I} + \tfrac{\Delta z}{2}\mathbf{V}(z+\Delta z) \right) \exp(\Delta z \mathbf{M}) \left(\mathbf{I} + \tfrac{\Delta z}{2}\mathbf{V}(z) \right) \mathbf{W}(z). \quad (1.9)$$

A complete mathematical derivation of the above equation is given in Chapter 2.

When the pressure $\tilde{P}(x,z)$ and pressure derivative $\tilde{Q}(x,z)$ are known, $\tilde{P}(x, z+\Delta z)$ and $\tilde{Q}(x, z+\Delta z)$ can be calculated by Eqn. (1.9) in a step-by-step process. Discretization of $\tilde{P}(x, z+\Delta z)$ and $\tilde{Q}(x, z+\Delta z)$ leads to $4N_x + 2$ coupled ordinary differential equations in the expansion components of the pressure $\tilde{P}(j\Delta x, z+\Delta z)$ and their derivatives $\tilde{Q}(x, z+\Delta z)$. Here $j = 0.1, ..., 2N_x$ are the indices in a Fourier basis expansion. To solve the coupled differential equations in the modeling problem initial values of pressure $\tilde{P}(j\Delta x, z_0)$ and its derivative $\tilde{Q}(j\Delta x, z_0)$ are produced by considering a complete set of Volterra initial solutions. A Feshbach projection method [41] is applied to stabilize the solution by removing only growing evanescent waves, while retaining all propagating and decaying waves.

An advantage of the new full-wave phase-shift approach to that of Kosloff and Kessler's approach is that by taking the reference velocity c_0 constant by layer, the entire lateral variation of the velocity is included in the perturbation term V in the form of $I + \alpha V$. This makes the computation of the matrix exponential extremely efficient and inexpensive. Another feature of the new full-wave phase-shift approach is it can be readily applied to both seismic modeling and depth migration. This approach also provides ways to apply correct boundary conditions and eliminate exponentially growing evanescent waves while retaining the exponentially decaying evanescent waves.

This research is part of a long-term research project aimed at solving the new full-wave phase-shift approach developed by Kouri *et al.* In this dissertation new full-wave phase-shift approach is applied to seismic modeling and migration in different velocity models. The results are verified by constructing time snapshots of the acoustic wave propagation for these different velocity models. We introduce an easy parallelization of the new FWPS code based on the linearly independent solutions for various frequencies. Detailed analysis of absorbing boundary conditions and ways to improve the Feshbach projection-operator are also given. We have also studied the presence of evanescent waves in a realistic earth velocity model. Furthermore, we present the seismic inversion results obtained using Volterra inverse scattering series and new full-wave phase-shift approach reflection data.

1.6 Outline of the Dissertation

This dissertation is organized as follows.

Chapter 2 describes the procedure to solve the Helmholtz wave equation using the new full-wave phase-shift approach. Detailed descriptions and mathematical derivations regarding the computation of Feshbach projection-operator, absorbing boundary conditions, Volterra initial conditions, matrix exponential, and perturbation matrix are given in this chapter.

Chapter 3 analyzes the use of absorbing boundary conditions in the new full-wave phase-shift approach. Time snapshot results are given for three different velocity models to verify the validity of our new approach.

Chapter 4 discusses the presence of evanescent waves in a realistic earth velocity model.

Chapter 5 includes the results of Volterra inverse scattering for two velocity models with the reflection data obtained by the new full-wave phase-shift approach.

Chapter 6 includes the new modifications to new full-wave phase-shift algorithm. It includes an improved calculation of the Feshbach projection operator and a detailed description on parallelizing the source code. It also describes the optimized computation of the $V_{nn'}$ matrix.

Finally, Chapter 7 concludes with suggestions for future work.

Chapter 2

The New Full-wave Phase-shift Approach

2.1 Introduction

Simulation of wave propagation is important not only in petroleum industry but also in many engineering and scientific disciplines. The basic equation that describes wave propagation problems in the space-frequency domain is the Helmholtz acoustic wave equation. The Helmholtz equation in two-dimensions is defined through the equation

$$\frac{\partial^2}{\partial z^2}\tilde{P}(x,z,\omega) = \left(-\frac{\omega^2}{c^2} - \frac{\partial^2}{\partial x^2}\right)\tilde{P}(x,z,\omega), \tag{2.1}$$

where x and z denote horizontal and vertical Cartesian coordinates respectively, $\tilde{P}(x, z, \omega)$ denotes the space-frequency domain pressure field, ω is the angular frequency, and $c(x, z)$ is the velocity field. Here, z is being considered as the general direction of propagation. Equation (2.1) is a partial differential equation and hence, is difficult to solve. This second-order partial differential equation can be transformed into two coupled, first-order differential equations in the depth variable z as follows:

$$\frac{\partial}{\partial z}\begin{pmatrix} \tilde{P} \\ \frac{\partial \tilde{P}}{\partial z} \end{pmatrix} = \begin{pmatrix} 0 & 1 \\ -\frac{\omega^2}{c^2} - \frac{\partial^2}{\partial x^2} & 0 \end{pmatrix}\begin{pmatrix} \tilde{P} \\ \frac{\partial \tilde{P}}{\partial z} \end{pmatrix}. \tag{2.2}$$

Equation (2.2) is a matrix partial differential equation and can be solved using a standard numerical procedure, such as Runge Kutta method. The accuracy of the solution depends on the numerical scheme adopted, as well as, the determination of the operator $\frac{\partial^2}{\partial x^2}$. The new full-wave phase-shift (FWPS) approach is based on the solution of the Helmholtz wave equation in the space-frequency domain. This new method was developed by Kouri *et al.* and it is based on a new way to generalize the one-way wave equation by decomposing the wave operator into a sum of two matrices. In the following sections, we explain the procedure to solve the new FWPS approach by highlighting the 2012 work of Kouri *et al* [37]. We consider mainly a modeling problem in two-dimensions, but this work can be easily extended into three-dimensions.

2.2 The New Full-wave Phase-shift Approach

First, we define a locally constant reference velocity c_0. Choosing the constant velocity is arbitrary, and the initial choice of c_0 is the minimum velocity at the surface $z = 0$. Then, starting with Eqn. (2.2), after addition and subtraction of $-\frac{\omega^2}{c_0^2}$, the wave operator is separated into the sum of two matrices. We obtain

$$\frac{\partial}{\partial z}\begin{pmatrix} \tilde{P} \\ \tilde{Q} \end{pmatrix} = \begin{pmatrix} 0 & 1 \\ -\frac{\omega^2}{c_0^2} - \frac{\partial^2}{\partial x^2} & 0 \end{pmatrix}\begin{pmatrix} \tilde{P} \\ \tilde{Q} \end{pmatrix} + \begin{pmatrix} 0 & 0 \\ -\frac{\omega^2}{c^2} + \frac{\omega^2}{c_0^2} & 0 \end{pmatrix}\begin{pmatrix} \tilde{P} \\ \tilde{Q} \end{pmatrix} \tag{2.3}$$

by setting $\tilde{Q} = \frac{\partial \tilde{P}}{\partial z}$. Equation (2.3) can be recast as

$$\frac{\partial}{\partial z}\mathbf{W} = \mathbf{M}\mathbf{W} + \mathbf{V}\mathbf{W}, \tag{2.4}$$

where,

$$\mathbf{M} = \begin{pmatrix} 0 & 1 \\ -\frac{\omega^2}{c_0^2} - \frac{\partial^2}{\partial x^2} & 0 \end{pmatrix}, \mathbf{V} = \begin{pmatrix} 0 & 0 \\ -\frac{\omega^2}{c^2} + \frac{\omega^2}{c_0^2} & 0 \end{pmatrix}, \text{ and } \mathbf{W} = \begin{pmatrix} \tilde{P} \\ \tilde{Q} \end{pmatrix}.$$

Separating the coupling operator into two matrices is called "operator splitting" [42, 43]. The two operators $\mathbf{M}$ and $\mathbf{V}$ are chosen to provide an efficient computational scheme. In Eqn. (2.4), the first operator $\mathbf{M}$ generates a propagator in the reference velocity medium, and the second operator $\mathbf{V}$ is a perturbation term which takes into account the vertical and lateral variation of the velocity field. Equation (2.4) is a linear, first-order partial differential equation, which can be exactly solved. Multiplying both sides of Eqn. (2.4) by $\exp(-\mathbf{M}z)$ we obtain

$$\exp(-\mathbf{M}z)\frac{\partial}{\partial z}\mathbf{W} = \exp(-\mathbf{M}z)\mathbf{M}\mathbf{W} + \exp(-\mathbf{M}z)\mathbf{V}\mathbf{W}. \tag{2.5}$$

Using the fact that $\mathbf{M}$ and $\exp(-\mathbf{M}z)$ commute we get

$$\exp(-\mathbf{M}z)\frac{\partial}{\partial z}\mathbf{W} - \mathbf{M}\exp(-\mathbf{M}z)\mathbf{W} = \exp(-\mathbf{M}z)\mathbf{V}\mathbf{W}. \tag{2.6}$$

Since,

$$\frac{\partial}{\partial z}\Bigg(\exp(-\mathbf{M}z)\mathbf{W} \Bigg) = -\mathbf{M}\exp(-\mathbf{M}z)\mathbf{W} + \exp(-\mathbf{M}z)\mathbf{W}, \tag{2.7}$$

Eqn. (2.6) can be simplified into the following form

$$\frac{\partial}{\partial z}\Bigg(\exp(-\mathbf{M}z)\mathbf{W} \Bigg) = \exp(-\mathbf{M}z)\mathbf{V}\mathbf{W}. \tag{2.8}$$

Upon integration Eqn. (2.8) from z up to $z + \Delta z$, where Δz is the grid spacing in the depth variable, we obtain

$$\begin{aligned} &\exp[-(z+\Delta z)\mathbf{M})]\mathbf{W}(x, z+\Delta z) = \\ &\qquad \exp(-z\mathbf{M})\mathbf{W}(x,z) + \int_z^{z+\Delta z} dz' \exp(-z'\mathbf{M})\mathbf{V}(x,z')\mathbf{W}(x,z'). \end{aligned} \tag{2.9}$$

Finally, multiplying the last equation by $\exp[-(z+\Delta z)\mathbf{M})]$ we get

$$\begin{aligned} \mathbf{W}(x, z+\Delta z) &= \exp(\Delta z\mathbf{M})\mathbf{W}(x,z) \\ &\qquad + \int_z^{z+\Delta z} dz' \exp([z+\Delta z - z']\mathbf{M})\mathbf{V}(x,z')\mathbf{W}(x,z'). \end{aligned} \tag{2.10}$$

Equation (2.10) is an exact, formal solution of the full wave equation. Following the work of Judson *et al.* (1991) [44], Eqn. (2.10) can be converted into an explicit form to calculate $\mathbf{W}$ numerically. In this approach Newton-Cotes quadrature is applied to approximate the z-integral. The simple trapezoidal rule is used to discretize the integral inside the solution to the full wave Eqn. (2.10). Then, Eqn. (2.10) can be rearranged to

$$\mathbf{W}(z+\Delta z) = \Bigg(\mathbf{I} - \tfrac{\Delta z}{2}\mathbf{V}(z+\Delta z) \Bigg)^{-1} \exp(\Delta z\mathbf{M}) \Bigg(\mathbf{I} + \tfrac{\Delta z}{2}\mathbf{V}(z) \Bigg)\mathbf{W}(z), \tag{2.11}$$

where $\mathbf{I}$ is a 2×2 identity matrix.

The operator $(\mathbf{I}-\frac{\Delta z}{2}\mathbf{V}(z+\Delta z))$ must be inverted to get an exact solution. Because of the structure of $\mathbf{V}$, the computation of the inverse in Eqn. (2.11) is analytical and straightforward:

$$\left(\ \mathbf{I}-\tfrac{\Delta z}{2}\mathbf{V}(z+\Delta z)\ \right)^{-1}=\left(\ \mathbf{I}+\tfrac{\Delta z}{2}\mathbf{V}(z+\Delta z)\ \right). \tag{2.12}$$

Finally, we obtain the recursion expression

$$\mathbf{W}(z+\Delta z)=\left(\ \mathbf{I}+\tfrac{\Delta z}{2}\mathbf{V}(z+\Delta z)\ \right)\exp(\Delta z\mathbf{M})\left(\ \mathbf{I}+\tfrac{\Delta z}{2}\mathbf{V}(z)\ \right)\mathbf{W}(z), \tag{2.13}$$

which is the simplest new FWPS approach solution. When the pressure $\tilde{P}(x,z)$ and pressure derivative $\tilde{Q}(x,z)$ are known, $\tilde{P}(x,z+\Delta z)$ and $\tilde{Q}(x,z+\Delta z)$ can be calculated by Eqn. (2.13) in a step by step process.

Equation (2.13) consists of coupled first order differential equations that cannot be solved analytically further. To get the solution of pressure and its derivative at each depth, $\tilde{P}(x,z)$ and $\tilde{Q}(x,z)$ are discretized using a finite grid along the x direction. This discretization is convenient since seismic data includes discrete time histories at discrete points on the earth. When discretized, $\tilde{P}(x,z)$ and $\tilde{Q}(x,z)$ become $\tilde{P}(j\Delta x,z)$ and $\tilde{Q}(j\Delta x,z)$, where $j=0,\pm1,\pm2,...,\pm N_x$. Now the coupled equations are converted into a set of $2\times(2N_x+1)$ coupled differential equations. In order to solve these coupled equations in (2.13) further, the matrix exponential and the perturbation term should also be calculated in the discretized version. Also, for the seismic modeling problem, initial values of pressure and its derivative at each x grid point for the initial z_0 (surface values) are needed. Next sections of this chapter discuss the procedures mentioned above.

2.3 Computation of the Matrix Exponential and the Perturbation Matrix

2.3.1 Computation of the Matrix Exponential

The structure of the matrix $\mathbf{M}$ in Eqn. (2.4) is given by

$$\mathbf{M} = \begin{pmatrix} 0 & 1 \\ -\frac{\omega^2}{c_0^2} - \frac{\partial^2}{\partial x^2} & 0 \end{pmatrix} = \begin{pmatrix} 0 & \mathbf{I} \\ \mathbf{S} & 0 \end{pmatrix}. \tag{2.14}$$

In the Fourier basis $\frac{\exp(2\pi inx/L)}{\sqrt{L}}$, the matrix $\mathbf{M}$ is of the size $2\times(2N_x+1)*2\times(2N_x+1)$ and not diagonal. The submatrix $\mathbf{S}$ in the Fourier basis is diagonal and given by

$$\mathbf{S} = \begin{pmatrix} (-\frac{\omega^2}{c_1^2} + (\frac{-2\pi N_x}{L})^2) & 0 & \dots & 0 \\ 0 & (-\frac{\omega^2}{c_2^2} + (\frac{2\pi(-N_x+1)}{L})^2) & \dots & 0 \\ \vdots & \vdots & \ddots & \vdots \\ 0 & 0 & \dots & (-\frac{\omega^2}{c_N^2} + (\frac{2\pi N_x}{L})^2) \end{pmatrix}. \tag{2.15}$$

Here c_j are the constant reference velocities and they are all set to c_0. L is equal to $2N_x\Delta x$ and it is the length of the finite grid, where Δx is the grid spacing along x direction. The eigenvalues of the submatrix $\mathbf{S}$ are its diagonal elements:

$$\lambda_j = -\frac{\omega^2}{c_j^2} + \left(\frac{2\pi k}{L}\right)^2 \tag{2.16}$$

where $j = 1, 2, ..., (2N_x + 1)$ and $k = (-N_x + j - 1)$. The eigenvalues of the $\mathbf{S}$ matrix are pure real. The eigenvalues of the matrix $\mathbf{M}$ can be determined using the eigenvalues of the submatrix $\mathbf{S}$ [34, 45] and are given by $\pm\sqrt{\lambda_j}$, where $j =$

$1, 2, ..., 2N_x + 1$. The corresponding eigenvectors $\Psi_j^{\pm}$ are given by,

$$(\Psi_j^{\pm})_{j'} = 1\delta_{j,j'} \pm \sqrt{\lambda_j}\delta_{(2N_x+1+j),(2N_x+1+j')}. \tag{2.17}$$

Using these eigenvectors, a matrix $\mathbf{T}$ of the size $(4N_x+2)\times(4N_x+2)$ is defined with its columns consisting of the eigenvectors of matrix $\mathbf{M}$. Then the exponential term can be written as [46]:

$$\exp(\mathbf{M}\Delta z) = \mathbf{T}\exp(\Lambda\Delta z)\mathbf{T}^{-1}, \tag{2.18}$$

where,

$$\exp(\Lambda\Delta z) = \begin{pmatrix} e^{(\sqrt{\lambda_1}\Delta z)} & 0 & \ldots & & & & & 0 \\ 0 & e^{(\sqrt{\lambda_2}\Delta z)} & 0 & \ldots & & & & \\ \vdots & & \ddots & & & & & \\ & & & e^{(\sqrt{\lambda_{2N_x+1}}\Delta z)} & 0 & \ldots & & \\ & & & & e^{(-\sqrt{\lambda_1}\Delta z)} & 0 & \ldots & \\ & & & & & \ddots & 0 & \\ 0 & & & & & & e^{(-\sqrt{\lambda_{2N_x+1}}\Delta z)} & \end{pmatrix}.$$

It can be seen from Eqn. (2.18) that computation of the matrix exponential is simply applying a phase-shift. Therefore, the computation of the matrix exponential is inexpensive (saves computer time and storage) in new FWPS method and is efficient to be used in many problems involving very large matrices. This advantage is due to the fact that entire lateral variation of the velocity is included in $\mathbf{V}$, by taking c_0 constant.

2.3.2 Computation of the Perturbation Term in the Fourier Basis

In order to carry out computation of solutions to the new FWPS approach, the operator $\mathbf{V}$ in Eqn. (2.13) has to be expanded in a Fourier basis. First, matrix $\mathbf{A}$ is defined as

$$\mathbf{A} = \mathbf{M} + \mathbf{V}, \tag{2.19}$$

where,

$$\mathbf{A} = \begin{pmatrix} 0 & \mathbf{I} \\ -\frac{\omega^2}{c^2} - \frac{\partial^2}{\partial x^2} & 0 \end{pmatrix} = \begin{pmatrix} 0 & \mathbf{I} \\ \mathbf{K} & 0 \end{pmatrix}. \tag{2.20}$$

Here, $\mathbf{I}$ represents the identity operator and it can be written in the Fourier basis as

$$\frac{1}{L}\int_0^L dx e^{i(n'-n)2\pi x/L} = \delta_{nn'}. \tag{2.21}$$

To obtain the Fourier basis matrix of $\mathbf{K}$, first $\frac{1}{c^2(x,z)}$ is expanded in the Fourier basis as

$$\frac{1}{c^2(x,z)} = \sum_{n=-N_x}^{N_x} S_n \frac{\exp(2\pi i n x/L)}{\sqrt{L}}, \tag{2.22}$$

where

$$S_n = \frac{1}{\sqrt{L}}\int_0^L dx \frac{\exp(-2\pi i n x/L)}{c^2(x,z)}. \tag{2.23}$$

Then,

$$\begin{aligned}
&\frac{1}{L}\int_0^L dx \frac{1}{c^2(x,z)} e^{i(n'-n)2\pi x/L} \\
&= \sum_{n''=-N_x}^{N_x} S_{n''} \int_0^L dx \frac{\exp(-2\pi n x/L)}{\sqrt{L}} \frac{\exp[2\pi(n'+n'')x/L]}{L} \\
&= \sum_{n''=-N_x}^{N_x} \frac{S_{n''}}{\sqrt{L}} \delta_{n,n''+n'}
\end{aligned} \tag{2.24}$$

and

$$\frac{1}{L}\int_0^L dx e^{-2\pi i n x/L}\left(\mathbf{K}\right) e^{2\pi i n' x/L} = \delta_{nn'}\left(\frac{2\pi n'}{L}\right)^2 - \omega^2 \sum_{n''=-N_x}^{N_x} \frac{S_{n''}}{\sqrt{L}} \delta_{n,n''+n'}. \tag{2.25}$$

The choice of simplest splitting used by Kouri *et al.* is

$$\mathbf{K} = \mathbf{K}_0 + \mathbf{V_1} \tag{2.26}$$

with

$$\begin{aligned}
\frac{1}{L}\int_0^L dx e^{-2\pi i n x/L}\left(\mathbf{K}_0\right) e^{2\pi i n' x/L} &= \frac{1}{L}\int_0^L dx e^{-2\pi i n x/L}\left(-\frac{\omega^2}{c_0^2} - \frac{\partial^2}{\partial x^2}\right) e^{2\pi i n' x/L} \\
&= \delta_{nn'}\Big[\left(\frac{2\pi n}{L}\right)^2 - \omega^2 S_0\Big],
\end{aligned} \tag{2.27}$$

and

$$\begin{aligned}
\frac{1}{L}\int_0^L dx e^{-2\pi i n x/L}\left(\mathbf{V}_1\right) e^{2\pi i n' x/L} &= \frac{1}{L}\int_0^L dx e^{-2\pi i n x/L}\left(\frac{\omega^2}{c_0^2} - \frac{\omega^2}{c^2(x,z)}\right) e^{2\pi i n' x/L} \\
&= \omega^2\left(S_0\delta_{nn'} - \sum_{n''=-N_x}^{N_x} \frac{S_{n''}}{\sqrt{L}} \delta_{n,n''+n'}\right).
\end{aligned} \tag{2.28}$$

2.4 Method for Finding Initial Conditions for New FWPS Approach Using Volterra Solutions

In order to initiate the computation of solutions to the new FWPS approach, the correct surface values of $\tilde{P}(x, z_0, \omega)$ and $\tilde{Q}(x, z_0, \omega)$ should be provided. But the correct $\tilde{P}(x, z_0, \omega)$ and $\tilde{Q}(x, z_0, \omega)$ that produce the desired solution need the measurement of reflections produced by the inhomogeneities in the velocity model, which can only be attained by solving the forward problem . Following is the method used by Kouri *et al.* to provide these initial conditions. It is started with deriving the Lippmann-Schwinger solution of the Helmholtz wave equation.

The two dimensional Helmholtz equation in the space-frequency domain can be written as

$$[\nabla^2 + \frac{\omega^2}{c^2(x,z)}]P(x,z,\omega) = 0, \tag{2.29}$$

where

$$\frac{1}{c^2} = \frac{1}{c_0^2}[1 - V(x,z)] \tag{2.30}$$

in terms of constant reference velocity c_0 and a perturbation $V(x, z)$. Then, the Helmholtz equation can be rewritten as

$$[\nabla^2 + \frac{\omega^2}{c_0^2(x,z)}]P(x,z,\omega) = \frac{\omega^2}{c_0^2}V(x,z)P(x,z,\omega) \tag{2.31}$$

in terms of c_0 and $V(x, z)$. An integral equation corresponding to Eqn. (2.31) is given by

$$\begin{aligned}P^+(x,z,\omega) &= P_0^+(x,z,\omega)\\ &+ \int_{z_0}^{z_1} dz' \int_0^L dx' G_0^+(x,x',z,z',\omega)k^2 V(x',z')P^+(x',z',\omega),\end{aligned} \tag{2.32}$$

where $k = \omega/c_0$. This was obtained using the causal free-space Green's function

$$G_0^+(x,x',z,z',\omega) = -\frac{i}{2}\sum_n \frac{1}{k_n}\frac{\exp(2in\pi x/L)}{\sqrt{L}}\frac{\exp(-2in\pi x'/L)}{\sqrt{L}}\exp(ik_n|z-z'|) \tag{2.33}$$

which satisfies the equation

$$[\nabla^2 + k^2]G_0^+(x,x',z,z',\omega) = \delta(x-x')\delta(z-z'). \tag{2.34}$$

The dispersion relation of k_n in Eqn. (2.33) is given by

$$k_n = \sqrt{-\frac{\omega^2}{c_0^2} + (\frac{2\pi n}{L})^2}. \tag{2.35}$$

Equation (2.32) is the Lippmann-Schwinger equation. The pressure field $P_0^+(x,z,\omega)$ represents a wavefield in the reference medium and the integral represents a scattered wavefield due to the perturbation. At this point compact support is assumed for $V(x,z)$ on the $[z_0,\, z_1]$ domain.

Expanding the pressure terms in Eqn. (2.32) in the Fourier basis $\frac{\exp(2\pi inx/L)}{\sqrt{L}}$

$$P^+(x,z,n,\omega) = \sum_{n'} \frac{\exp(2\pi in'x/L)}{\sqrt{L}} P^+(n',z,n,\omega), \tag{2.36}$$

and using Eqn. (2.33),

$$\sum_{n'} \frac{\exp(2\pi i n' x/L)}{\sqrt{L}} P^+(n', z, n, \omega) =$$
$$\exp(ik_n z)\frac{\exp(2\pi i n x/L)}{\sqrt{L}} - \frac{ik^2}{2}\sum_{n'} \frac{1}{k_{n'}} \frac{\exp(2\pi i n' x/L)}{\sqrt{L}} \int_{z_0}^{z_1} dz' \exp(ik_{n'}|z-z'|)$$
$$\int_0^L dx' \frac{\exp(-2\pi i n' x'/L)}{\sqrt{L}} V(x', z') \sum_{n''} \frac{\exp(2\pi i n'' x'/L)}{\sqrt{L}} P^+(n'', z', n, \omega) \qquad (2.37)$$

can be obtained. Multiplying both sides of Eqn. (2.37) by $\frac{\exp(-2\pi i n' x/L)}{\sqrt{L}}$ and integrating over x, we get

$$\begin{aligned} P^+(n', z, n, \omega) &= \exp(ik_n z)\delta_{nn'} - \frac{ik^2}{2}\sum_{n''} \frac{1}{k_{n'}} \int_{z_0}^{z_1} dz' \exp(ik_{n'}|z-z'|) \\ & \quad V(n', n'', z') P^+(n'', z', n, \omega). \end{aligned} \qquad (2.38)$$

Equation (2.38) is the causal Lippmann-Schwinger solution of the acoustic wave equation in the Fourier basis. It has the form of an inhomogeneous Fredholm integral equation of the second kind. In Eqn. (2.38), the first index n' corresponds to the dependence in the lateral variation x and the second index n corresponds to dependence on the lateral position of the source x_0.

To solve Eqn. (2.38), the information of $P^+(n'', z', n, \omega)$ is needed in all the regions where the perturbation is nonzero. This problem is resolved by transforming Eqn. (2.38) into an inhomogeneous Volterra integral equation of the second kind. This transformation follows the work of Sams and Kouri [38, 39] and Smith *et al.* [47].

The absolute value appearing in the argument of the Green's function can be eliminated by writing the integral over z' in terms of an integral from z_0 to z plus an integral from z to z_1:

$$\begin{aligned}
&P^+(n',z,n,\omega) = \delta_{nn'}\exp(ik_n z) \\
&\quad -\frac{ik^2}{2}\sum_{n''}\frac{1}{k_{n'}}\int_{z_0}^{z} dz' \exp(ik_{n'}(z-z'))V(n',n'',z')P^+(n'',z',n,\omega) \\
&\quad -\frac{ik^2}{2}\sum_{n''}\frac{1}{k_{n'}}\int_{z}^{z_1} dz' \exp(ik_{n'}(z'-z))V(n',n'',z')P^+(n'',z',n,\omega). \qquad (2.39)
\end{aligned}$$

Introducing a new matrix notation,

$$(\mathbf{P}^+(z))_{n'n} = P^+(n',z,n,\omega). \qquad (2.40)$$

Eqn. (2.39) can be written as

$$\begin{aligned}
\mathbf{P}^+(z) = \mathbf{e}^+(z) \quad &- \quad \frac{ik^2}{2}\mathbf{k}^{-1}\mathbf{e}^+(z)\int_{z_0}^{z} dz'\mathbf{e}^-(z')\mathbf{V}(z')\mathbf{P}^+(z') \\
&- \quad \frac{ik^2}{2}\mathbf{k}^{-1}\mathbf{e}^-(z)\int_{z}^{z_1} dz'\mathbf{e}^+(z')\mathbf{V}(z')\mathbf{P}^+(z'). \qquad (2.41)
\end{aligned}$$

The $\mathbf{e}^+$ and $\mathbf{e}^-$ are diagonal downgoing (+) and upcoming (-) matrices of plane waves having the following form:

$$\mathbf{e}^{\pm} \quad = \quad \begin{pmatrix} \exp(\pm ik_0 z) & 0 & \dots & 0 \\ 0 & \exp(\pm ik_1 z) & \dots & 0 \\ \vdots & \vdots & \ddots & \vdots \\ 0 & 0 & \dots & \exp(\pm ik_{2N_x} z) \end{pmatrix}. \qquad (2.42)$$

$\mathbf{k}^{-1}$ in Eqn. (2.42) is also a diagonal matrix with elements $\delta_{nn'}/k_n$:

$$\mathbf{k}^{-1} \quad = \quad \begin{pmatrix} \frac{1}{k_0} & 0 & \dots & 0 \\ 0 & \frac{1}{k_1} & \dots & 0 \\ \vdots & \vdots & \ddots & \vdots \\ 0 & 0 & \dots & \frac{1}{k_{2N_x}} \end{pmatrix}. \qquad (2.43)$$

The physical solution for $z \le z_0$ is given by

$$\mathbf{P}^+(z) = \mathbf{e}^+ + \mathbf{e}^-\mathbf{r}(\omega), \tag{2.44}$$

where $\mathbf{r}(\omega)$ is the reflection amplitude matrix given by

$$\mathbf{r}(\omega) = -\frac{ik^2}{2}\mathbf{k}^{-1}\int_{z_0}^{z_1} dz'\mathbf{e}^+(z')\mathbf{V}(z')\mathbf{P}^+(z'). \tag{2.45}$$

Adding and subtracting the following term,

$$-\frac{ik^2}{2}\mathbf{k}^{-1}\mathbf{e}^-(z)\int_{z_0}^{z_1} dz'\mathbf{e}^+(z')\mathbf{V}(z')\mathbf{P}^+(z'),$$

Eqn. (2.41) can be simplified into:

$$\begin{aligned}\mathbf{P}^+(z) = \mathbf{e}^+(z) + \mathbf{e}^-(z)\mathbf{r}(\omega) \quad &- \quad \frac{ik^2}{2}\mathbf{k}^{-1}\mathbf{e}^+(z)\int_{z_0}^{z} dz'\mathbf{e}^-(z')\mathbf{V}(z')\mathbf{P}^+(z') \\ &+ \quad \frac{ik^2}{2}\mathbf{k}^{-1}\mathbf{e}^-(z)\int_{z_0}^{z} dz'\mathbf{e}^+(z')\mathbf{V}(z')\mathbf{P}^+(z').\end{aligned} \tag{2.46}$$

Assume a solution of the form

$$\mathbf{P}^+(z) = \mathbf{P}_1(z) + \mathbf{P}_2(z)\mathbf{r}(\omega). \tag{2.47}$$

Then,

$$\begin{aligned}\mathbf{P}_1(z) = \mathbf{e}^+(z) \quad &- \quad \frac{ik^2}{2}\mathbf{k}^{-1}\mathbf{e}^+(z)\int_{z_0}^{z} dz'\mathbf{e}^-(z')\mathbf{V}(z')\mathbf{P}_1(z') \\ &+ \quad \frac{ik^2}{2}\mathbf{k}^{-1}\mathbf{e}^-(z)\int_{z_0}^{z} dz'\mathbf{e}^+(z')\mathbf{V}(z')\mathbf{P}_1(z')\end{aligned} \tag{2.48}$$

and

$$\begin{aligned}\mathbf{P}_2(z) = \mathbf{e}^-(z) \quad &- \quad \frac{ik^2}{2}\mathbf{k}^{-1}\mathbf{e}^+(z)\int_{z_0}^{z} dz'\mathbf{e}^-(z')\mathbf{V}(z')\mathbf{P}_2(z') \\ &+ \quad \frac{ik^2}{2}\mathbf{k}^{-1}\mathbf{e}^-(z)\int_{z_0}^{z} dz'\mathbf{e}^+(z')\mathbf{V}(z')\mathbf{P}_2(z')\end{aligned} \tag{2.49}$$

are required to satisfy Eqn. (2.47). Now the reflection amplitude matrix is

$$\begin{aligned}\mathbf{r}_{n'n}(\omega) &= \Big([\underline{\mathbf{1}} + \frac{ik^2}{2}\mathbf{k}^{-1}\int_{z_0}^{z_1} dz'\mathbf{e}^{+}(z')\mathbf{V}(z')\mathbf{P}_2(z')]^{-1} \\ &\quad [-\frac{ik^2}{2}\mathbf{k}^{-1}\int_{z_0}^{z_1} dz'\mathbf{e}^{+}(z')\mathbf{V}(z')\mathbf{P}_1(z')]\Big)_{n'n}, \end{aligned} \tag{2.50}$$

in terms of $\mathbf{P}_1(z)$ and $\mathbf{P}_2(z)$. It indicates a dense operator, with each column describing the full angular dependence of reflection associated with x-wave number k_n. The two integral Eqns. (2.48) and (2.49) are the desired Volterra equations. The initial values of $\mathbf{P}_1$ and its derivatives with respect to z, $\mathbf{Q}_1$ are determined by the fact that for z less than or equal to z_0, the solution is equal to $\mathbf{e}^{+}$. Therefore, the form of the initial pressure and its derivative will be

$$\mathbf{P}_1(z_0) = \begin{pmatrix} \exp(+ik_0z_0) & 0 & \dots & 0 \\ 0 & \exp(+ik_1z_0) & \dots & 0 \\ \vdots & \vdots & \ddots & \vdots \\ 0 & 0 & \dots & \exp(+ik_{2N_x}z_0) \end{pmatrix} \tag{2.51}$$

and

$$\mathbf{Q}_1(z_0) = \begin{pmatrix} +ik_0\exp(+ik_0z_0) & 0 & \dots & 0 \\ 0 & +ik_1\exp(+ik_1z_0) & \dots & 0 \\ \vdots & \vdots & \ddots & \vdots \\ 0 & 0 & \dots & +ik_{2N_x}\exp(+ik_{2N_x}z_0) \end{pmatrix}. \tag{2.52}$$

Using Eqns. (2.51) and (2.52), $\mathbf{P}_1(z)$ and $\mathbf{Q}_1(z)$ can be calculated for any z value. Then $\mathbf{P}_2(z)$ and $\mathbf{Q}_2(z)$ can be obtained by complex conjugation. Now using these Volterra solutions the desired Lippmann-Schwinger solution can be calculated using the well defined transformation in (2.48) and (2.49) and the reflection matrix $\mathbf{r}_{n'n}(\omega)$ computed from Eqn. (2.50).

2.5 Absorbing Boundary Conditions

Numerical calculations for solving Helmholtz equation require a bounded or finite volume which leads to artificial reflections from the boundary. Also using Fourier method, which has periodic properties leads to wraparounds from the artificial boundaries. Those are fundamental problems which arise in the numerical simulation of the wave phenomena. These reflection and wraparound waves will interfere with the true seismic waves as they propagate into the modeled region, and will lead to artificial reflections not observed in the actual seismic experiment. Therefore, an efficient method must be introduced to remove the unwanted reflections and wraparounds.

In 1986, Kosloff *et al.* [48] introduced a method of absorbing boundary conditions which can be used both for acoustic and elastic wave equations. In their method, the wave amplitude is attenuated at the grid boundary region based on a simple modification of the wave equation. The modified two dimensional acoustic wave equation in the space-time domain can be written as:

$$\frac{\partial}{\partial t}\begin{pmatrix} \tilde{P} \\ \frac{\partial \tilde{P}}{\partial t} \end{pmatrix} = \begin{pmatrix} -\gamma & 1 \\ c^2\nabla^2_{xz} & -\gamma \end{pmatrix}\begin{pmatrix} \tilde{P} \\ \frac{\partial \tilde{P}}{\partial t} \end{pmatrix}. \tag{2.53}$$

Here, γ is the reduction function of the form $\gamma = a/\cosh^2(\alpha n)$ where a is a constant,

α is a decay factor and n is the distance in number of grid points from the boundary. Kouri *et al.* followed a similar principle as in Eqn. (2.53) to introduce an reduction function to implement absorbing boundary conditions in new FWPS approach. Introducing an absorbing potential in the space-frequency domain, Eqn. (2.2) can be written as

$$\frac{\partial}{\partial z}\begin{pmatrix} \tilde{P} \\ \frac{\partial \tilde{P}}{\partial z} \end{pmatrix} = \begin{pmatrix} -\gamma & 1 \\ \left[-\frac{\omega^2}{c^2} - \frac{\partial^2}{\partial x^2}\right] & -\gamma \end{pmatrix}\begin{pmatrix} \tilde{P} \\ \frac{\partial \tilde{P}}{\partial z} \end{pmatrix}. \tag{2.54}$$

As explained section 2.2, operator splitting can be applied to write the matrix on the right hand side of the Eqn. (2.54) in terms of two matrices

$$\mathbf{M} = \begin{pmatrix} 0 & 1 \\ -\frac{\omega^2}{c_0^2} - \frac{\partial^2}{\partial x^2} & 0 \end{pmatrix}, \tilde{\mathbf{V}}_{\mathbf{Ab}} = \begin{pmatrix} -\gamma & 0 \\ V_{Ab} & -\gamma \end{pmatrix},$$

$$\begin{pmatrix} -\gamma & 1 \\ -\frac{\omega^2}{c^2} - \frac{\partial^2}{\partial x^2} & -\gamma \end{pmatrix} = \mathbf{M} + \tilde{\mathbf{V}}_{\mathbf{Ab}}. \tag{2.55}$$

Here, $V_{Ab} = -\frac{\omega^2}{c^2} + \frac{\omega^2}{c_0^2}$. There is no change made in the matrix $\mathbf{M}$. Following the same procedure applied to get Eqn. (2.11), a new equation with absorbing boundary conditions can be obtained:

$$\mathbf{W}(z+\Delta z) = \left(\mathbf{I} - \frac{\Delta z}{2}\tilde{\mathbf{V}}_{\mathbf{Ab}}(z+\Delta z)\right)^{-1}\exp(\Delta z\mathbf{M})\left(\mathbf{I} + \frac{\Delta z}{2}\tilde{\mathbf{V}}_{\mathbf{Ab}}(z)\right)\mathbf{W}(z). \tag{2.56}$$

The matrix inversion in Eqn. (2.56) can be done analytically as before,

$$\mathbf{D}_{Ab} = \begin{pmatrix} (1+\frac{\Delta z}{2}\gamma)^{-1} & 0 \\ \left[\frac{\Delta z}{2}(1+\frac{\Delta z}{2}\gamma)^{-1}V_{Ab}(1+\frac{\Delta z}{2}\gamma)^{-1}\right] & (1+\frac{\Delta z}{2}\gamma)^{-1} \end{pmatrix}. \tag{2.57}$$

Therefore, the new FWPS approach solution with the absorbing boundary becomes

$$\mathbf{W}(z+\Delta z) = \mathbf{D}_{Ab}(z+\Delta z)\exp(\Delta z\mathbf{M})\left(\mathbf{I} + \tfrac{\Delta z}{2}\tilde{\mathbf{V}}_{\mathbf{Ab}}(z) \right)\mathbf{W}(z). \tag{2.58}$$

One can also use the Helmholtz equation with damping terms,

$$\frac{\partial^2}{\partial t^2}\tilde{P}(x,z,t) = c^2\frac{\partial^2}{\partial x^2}\tilde{P}(x,z,t) - 2\gamma\frac{\partial}{\partial t}\tilde{P}(x,z,t) - \gamma^2\tilde{P}(x,z,t), \tag{2.59}$$

and directly transform the Eqn. (2.59) to the frequency domain by using a standard time-frequency Fourier transform. Transformation of Eqn. (2.59) to the frequency-space domain yields the form

$$\begin{aligned}\frac{\partial}{\partial z}\begin{pmatrix} \tilde{P} \\ \frac{\partial \tilde{P}}{\partial z} \end{pmatrix} &= \begin{pmatrix} 0 & 1 \\ \left[-\frac{1}{c^2}(\omega^2 - \gamma^2 + i2\gamma\omega) - \frac{\partial^2}{\partial x^2}\right] & 0 \end{pmatrix}\begin{pmatrix} \tilde{P} \\ \frac{\partial \tilde{P}}{\partial z} \end{pmatrix} \\ &= \mathbf{H}_{Ab}\begin{pmatrix} \tilde{P} \\ \frac{\partial \tilde{P}}{\partial z} \end{pmatrix}.\end{aligned} \tag{2.60}$$

Next, simply write the matrix $\mathbf{H}_{Ab}$ as $\mathbf{M}$ plus $\mathbf{V}$ to cast Eqn. (2.4).

$$\mathbf{H}_{Ab} = \mathbf{M} + \mathbf{V}_{Ab} = \begin{pmatrix} 0 & 1 \\ -\left[\frac{\partial^2}{\partial x^2} + \frac{\omega^2}{c_0^2}\right] & 0 \end{pmatrix} + \begin{pmatrix} 0 & 0 \\ \left[\frac{\omega^2}{c_0^2} - \frac{1}{c^2}\left(\omega^2 - \gamma^2 + i2\omega\gamma\right)\right] & 0 \end{pmatrix}. \tag{2.61}$$

Again only the perturbation term is modified due to applying absorbing boundary conditions. In that case, the working equation with absorbing boundaries is

$$\begin{aligned}\mathbf{W}(z+\Delta z) &= \left(\mathbf{I} + \tfrac{\Delta z}{2}\mathbf{V}_{Ab}(z+\Delta z) \right) \\ &\quad \exp(\Delta z\mathbf{M})\left(\mathbf{I} + \tfrac{\Delta z}{2}\mathbf{V}_{Ab}(z) \right)\mathbf{W}(z).\end{aligned} \tag{2.62}$$

2.6 Feshbach Projection-operator Method to Remove Growing Evanescent Waves in the New FWPS Approach

Another difficulty in solving the Helmholtz acoustic wave equation using a complete basis expansion is the occurrence of evanescent waves or exponentially growing/decaying waves. To get a stable solution for the wave equation there should be a method to filter the exponentially growing evanescent waves. For example, global filtering, proposed by Kosloff and Baysal [35], is a method of removing evanescent waves by eliminating all the Fourier components that satisfy the condition $k_n = 2\pi n/L > \omega/c_{max}$, where c_{max} is the highest velocity between the depth step z and $z + \Delta z$. But their method also removed all the decaying evanescent waves, consequently removing the steep dip events in low-velocity regions. In contrast, the stabilizing method proposed by Kouri *et al.* only removes the exponentially growing evanescent waves while retaining all the propagating and exponentially decaying waves.

It is clearly observed from the Eqn. (2.16) that the eigenvalues of the matrix $\mathbf{M}$ are either purely real or purely imaginary depending on the values of $\{\lambda_i\}$s. The pure imaginary waves include wave numbers k_n^2 satisfying the relation $\omega^2/c_0^2 > (\frac{2\pi n}{L})^2$. These imaginary eigen values correspond to the propagating waves with a simple phase-shift. The pure real waves include wave numbers k_n^2 satisfying the relation $\omega^2/c_0^2 < (\frac{2\pi n}{L})^2$. They are associated with the exponentially growing or decaying evanescent waves. These evanescent waves can be generated experimentally from seismic sources that generate spherical waves or when the acoustic wave is crossing a velocity interface at an angle beyond the critical angle [49]. The negative real eigenvalues lead to an exponential decay as z increases and the positive real eigen values grow exponentially. Therefore, we have to eliminate the exponentially growing solution on grounds of energy conservation to obtain a numerically stable and accurate solution to the wave equation. To overcome this problem Kouri *et al.* have constructed and applied Feshbach projection-operator method in the solution of the new FWPS approach.

The Feshbach projection-operator approach was first introduced in nuclear physics [41]. It was later used in molecular quantum scattering [50]. In this method two projection-operators Π and $\mathbf{X}$ are constructed so that Π contains all the propagating waves (both upward and downward) and the decaying evanescent waves and $\mathbf{X}$ contains the growing evanescent waves.

These two operators satisfy the following properties:

$$\Pi^2 = \Pi, \quad \mathbf{X}^2 = \mathbf{X}, \quad \Pi + \mathbf{X} = 1, \quad \Pi\mathbf{X} = \mathbf{X}\Pi = 0. \tag{2.63}$$

The eigenvalues $\mathbf{M}$ are (for a constant reference velocity c_0)

$$\lambda_k = \pm\sqrt{-\frac{\omega^2}{c_0^2} + \left(\frac{2\pi j}{L}\right)^2}; \quad k = 1, 2, ..., (2N_x + 1) \ ; \quad j = (-N_x + k - 1). \tag{2.64}$$

The k^{th} eigenvector can be written as

$$\Psi_{\pm,k} = N_k \begin{pmatrix} 0 \\ 0 \\ \vdots \\ 1 \\ 0 \\ \vdots \\ \pm\sqrt{-\frac{\omega^2}{c_0^2} + \left(\frac{2\pi j}{L}\right)^2} \\ 0 \\ \vdots \end{pmatrix}, \tag{2.65}$$

where N_k is the normalization constant and the value 1 is at the k^{th} position and the value $\left(\pm\sqrt{-\frac{\omega^2}{c_0^2} + \left(\frac{2\pi j}{L}\right)^2}\right)$ is at the $(2N_x + k + 1)^{th}$ position of the eigenvector. The biorthogonal complement $\xi_{\pm,k}$ of $\Psi_{\pm,k}$ is

$$\xi_{\pm,k} = \frac{1}{2N_k}\left(0\ 0\ \ldots\ 1\ 0\ 0 \ldots\ \left(\pm\frac{1}{\sqrt{-\frac{\omega^2}{c_0^2} + \left(\frac{2\pi j}{L}\right)^2}}\right)\ 0\ \ldots\right). \tag{2.66}$$

Using the closure relationship Eqn. (2.63) for a complete set of states, along with their biorthogonal complements, the identity operator can be written in terms of the projection-operators, Π and $\mathbf{X}$,

$$\begin{aligned} \mathbf{I} &= \sum_{\pm,k} \Psi_{\pm,k}\xi_{\pm,k} = \left(\sum_{\pm,k_1} \Psi_{\pm,k_1}\xi_{\pm,k_1} + \sum_{\pm,k_2} \Psi_{\pm,k_2}\xi_{\pm,k_2}\right) \\ &= \left(\sum_{\pm,k_1} \Psi_{\pm,k_1}\xi_{\pm,k_1} + \sum_{-,k_2} \Psi_{-,k_2}\xi_{-,k_2}\right) + \sum_{+,k_2} \Psi_{+,k_2}\xi_{+,k_2} = \Pi + \mathbf{X}. \end{aligned} \tag{2.67}$$

Here, k_1 and k_2 run over eigenstates with imaginary and real eigenvalues, respectively. $(\pm, k_1)$ corresponds to propagating waves, $(-, k_2)$ denotes decaying components and $(+, k_2)$ growing components. The explicit form of Π is

$$\Pi = \begin{pmatrix} \mathbf{I}_1 & 0 \\ 0 & \mathbf{I}_1 \end{pmatrix} + \begin{pmatrix} \frac{1}{2}\mathbf{I}_2 & -\frac{1}{2}\frac{1}{\sqrt{-\frac{\omega^2}{c_0^2}+\left(\frac{2\pi j}{L}\right)^2}}\mathbf{I_2} \\ -\frac{1}{2}\sqrt{-\frac{\omega^2}{c_0^2}+\left(\frac{2\pi j}{L}\right)^2}\mathbf{I}_2 & \frac{1}{2}\mathbf{I_2} \end{pmatrix}, \tag{2.68}$$

where $\mathbf{I}_1$ and $\mathbf{I}_2$ are identity operators that only span the imaginary-eigenvalue and real-eigenvalue subspaces respectively.

The Feshbach projection-operator applied to Eqn. (2.62) can be written as:

$$\begin{aligned} \mathbf{I}(z+\Delta z)\mathbf{W}(z+\Delta z) = \mathbf{I}(z+\Delta z)\left(\mathbf{I} + \tfrac{\Delta z}{2}\mathbf{V}_{Ab}(z+\Delta z) \right) \\ \mathbf{I}(z+\Delta z)\exp(\Delta z\mathbf{M})\mathbf{I}(z)\left(\mathbf{I} + \tfrac{\Delta z}{2}\mathbf{V}_{Ab}(z) \right)\mathbf{I}(z)\mathbf{W}(z), \end{aligned} \tag{2.69}$$

or,

$$\begin{aligned} \left(\Pi(z+\Delta z)+\mathbf{X}(z+\Delta z)\right)\mathbf{W}(z+\Delta z) = \left(\Pi(z+\Delta z)+\mathbf{X}(z+\Delta z)\right) \\ \left(\mathbf{I} + \tfrac{\Delta z}{2}\mathbf{V}_{Ab}(z+\Delta z) \right)\left(\Pi(z+\Delta z)+\mathbf{X}(z+\Delta z)\right) \\ \exp(\Delta z\mathbf{M})\left(\Pi(z)+\mathbf{X}(z)\right)\left(\mathbf{I} + \tfrac{\Delta z}{2}\mathbf{V}_{\mathbf{Ab}}(z) \right)\left(\Pi(z)+\mathbf{X}(z)\right)\mathbf{W}(z). \end{aligned} \tag{2.70}$$

By applying $\Pi(z+\Delta z)$ from the left and throwing away all the terms containing $\mathbf{X}$ as an approximation, we get

$$\begin{aligned} \Pi(z+\Delta z)\mathbf{W}(z+\Delta z) \simeq \Pi(z+\Delta z)\left(\mathbf{I} + \tfrac{\Delta z}{2}\mathbf{V}_{Ab}(z+\Delta z) \right) \\ \Pi(z+\Delta z)\exp(\Delta z\mathbf{M})\Pi(z)\left(\mathbf{I} + \tfrac{\Delta z}{2}\mathbf{V}_{\mathbf{Ab}}(z) \right)\Pi(z)\mathbf{W}(z). \end{aligned} \tag{2.71}$$

Equation (2.71) is the our new working equation with Feshbach projection-operator and absorbing boundary conditions applied. If our reference velocity c_0 does not change along the z-direction, we have $\Pi(z + \Delta z) = \Pi(z)$.

Chapter 3

Computational Results

3.1 Testing of Absorbing Boundary Conditions for the New FWPS Approach

3.1.1 Introduction

Whenever we solve a partial differential equation numerically by a volume discretization, we must truncate the computational grid in some way, and the key question is how to perform this truncation without introducing significant artifacts: wraparounds and reflections from boundaries, into the computation since these undesired artifacts eventually override the actual seismic signals which propagate in the modeled region. Some problems are naturally truncated, *e.g.*, for periodic structures where periodic boundary conditions can be applied. Some problems involve solutions that are rapidly decaying in space, so that the truncation is irrelevant as long as the computational grid is large enough.

However, some of the most difficult problems to truncate involve wave equations, where the solutions are oscillating and typically decay with distance r only as $\frac{1}{r^{(d-1)/2}}$ in d-dimensions. The slow decay means that simply truncating the grid with hard-wall (Dirichlet or Neumann) or periodic boundary conditions will lead to unacceptable artifacts from boundary reflections. Therefore, wave equations require something different: an absorbing boundary that will somehow absorb waves that strike it, without any reflection. Applying a absorbing boundary is very important in wave-equation forward modeling and migration, as the absorbing boundary condition may effect the total computational cost and quality of the results.

In the following sections we describe how to apply absorbing boundary condition proposed by Kosloff *et al.* [48] to the new FWPS method solution and analyze its effectiveness in new FWPS approach on several velocity models.

3.1.2 Background

The first attempts at using absorbing boundaries for wave equations involved absorbing boundary conditions. First, Lysmer *et al.* [51] proposed a "viscous boundary" which absorbs reflecting waves effectively. Next, Lysmer *et al.* [52] proposed a "transmitting boundary" which absorbs body waves and surface waves on the lateral infinite boundary. Those absorbing boundary conditions are dependent upon frequency. Smith [53] proposed a "non reflecting boundary" which can be achieved by averaging the solution of two problems; one involving fixed boundary conditions and one involving free boundary conditions. In 1985, Kays proposed absorbing boundary conditions for acoustic media [54]. There are also several other methods for constructing absorbing boundaries proposed by Randall [55] and Higdon [56].

On the other hand, Kosloff *et al.* [48] proposed a method, which absorbed radiating waves from the interior of the finite grid. They showed the method applied to the Schrodinger equation and acoustic wave equation in two-dimensions and three-dimensions. It is based on a gradual reduction of the amplitudes in a strip of nodes along the boundaries of the grid. Since this method appears extremely simple and robust, and can be applied to a wide variety of time-dependent problems, we have followed a similar method to implement absorbing boundary conditions in to our solution of new FWPS approach to remove the unwanted reflections and wraparound effects.

3.1.3 Absorbing Boundary Conditions for New FWPS Approach

In Kosloff's method, the wave amplitude is attenuated at the grid boundary region based on a simple modification of the wave equation. The modified two dimensional acoustic wave equation in the space-time domain can be written as:

$$\frac{\partial}{\partial t}\begin{pmatrix} \tilde{P} \\ \frac{\partial \tilde{P}}{\partial t} \end{pmatrix} = \begin{pmatrix} -\gamma & 1 \\ c^2\nabla^2_{xz} & -\gamma \end{pmatrix}\begin{pmatrix} \tilde{P} \\ \frac{\partial \tilde{P}}{\partial t} \end{pmatrix}. \tag{3.1}$$

Here, γ is the reduction function of the form $\gamma = a/\cosh^2(\alpha n)$ where a is a constant, α is a decay factor, and n is the distance in number of grid points from the boundary. γ should be chosen so that it should be small enough to avoid reflections and large enough to eliminate transmissions.

Kouri *et al.* [37] followed a similar principle as in Eqn. (3.1) to introduce a reduction function to implement absorbing boundary conditions in new FWPS approach. The derivation of absorbing boundaries in the new FWPS approach is given in Chapter 2, Section 2.5. Following the method of Kosloff, the new FWPS method solution with the absorbing boundary conditions becomes:

$$\mathbf{W}(z+\Delta z) = \mathbf{D}_{Ab}(z+\Delta z)\exp(\Delta z\mathbf{M})\left(\ \mathbf{I} + \tfrac{\Delta z}{2}\tilde{\mathbf{V}}_{\mathbf{Ab}}(z)\ \right)\mathbf{W}(z) \tag{3.2}$$

with

$$\mathbf{D}_{Ab} = \begin{pmatrix} (1+\frac{\Delta z}{2}\gamma)^{-1} & 0 \\ \left[\frac{\Delta z}{2}(1+\frac{\Delta z}{2}\gamma)^{-1}V_{Ab}(1+\frac{\Delta z}{2}\gamma)^{-1}\right] & (1+\frac{\Delta z}{2}\gamma)^{-1} \end{pmatrix}. \tag{3.3}$$

One can also use the Helmholtz equation with damping terms, and directly transform the equation to the frequency domain by using a standard time-frequency Fourier transform. In that case, the absorbing potential enters in Eqn. (3.1). Then, transforming Eqn. (3.1) including the damping terms to the frequency-space domain yields the form

$$\begin{aligned} \frac{\partial}{\partial z}\begin{pmatrix} \tilde{P} \\ \frac{\partial \tilde{P}}{\partial z} \end{pmatrix} &= \begin{pmatrix} 0 & 1 \\ \left[-\frac{1}{c^2}(\omega^2 - \gamma^2 + i2\gamma\omega) - \frac{\partial^2}{\partial x^2}\right] & 0 \end{pmatrix}\begin{pmatrix} \tilde{P} \\ \frac{\partial \tilde{P}}{\partial z} \end{pmatrix} \\ &= \mathbf{H}_{Ab}\begin{pmatrix} \tilde{P} \\ \frac{\partial \tilde{P}}{\partial z} \end{pmatrix}, \end{aligned} \tag{3.4}$$

with matrix $\mathbf{H}_{Ab}$ written in the following format:

$$\mathbf{H}_{Ab} = \mathbf{M} + \mathbf{V} = \begin{pmatrix} 0 & 1 \\ -\left[\frac{\partial^2}{\partial x^2} + \frac{\omega^2}{c_0^2}\right] & 0 \end{pmatrix} + \begin{pmatrix} 0 & 0 \\ \left[\frac{\omega^2}{c_0^2} - \frac{1}{c^2}\left(\omega^2 - \gamma^2 + i2\omega\gamma\right)\right] & 0 \end{pmatrix}. \tag{3.5}$$

To reduce the extension of the numerical grid, in the new FWPS solution the absorbing potential γ is introduced in the z and x coordinates of the subsurface velocity model in the form of a reduction/damping function. Therefore, in our implementation of absorbing boundary conditions γ consists of two parts, γ_x and γ_z so that $\gamma = \gamma_x + \gamma_z$.

Figure 3.1 shows the shape of the damping function $\gamma = a/\cosh^2(\alpha n)$ at $a = 5.0$ and $\alpha = 0.10$. Figure 3.2 shows enlarged sections of γ with different α values. In Fig. 3.2(a), $\alpha = 0.18$ with 20 absorbing grid points and in Fig. 3.2(b), $\alpha = 0.10$ with 35 absorbing grid points. Figure 3.2 indicates that by reducing α in the damping function one must increase the length of the damping region.

By introducing the damping function γ in the perturbation matrix $\mathbf{V}$, the value of $P(x, z, w)$ is slightly reduced at each depth step in a strip of grid points on left, right and bottom of the velocity model. The amplitude reduction in each strip is gradually tapered from a zero value in the interior boundary. We do not introduce an absorbing boundary conditions at the top of the model as in the new FWPS approach, since we only deal with downgoing waves when initiating the wave propagation.

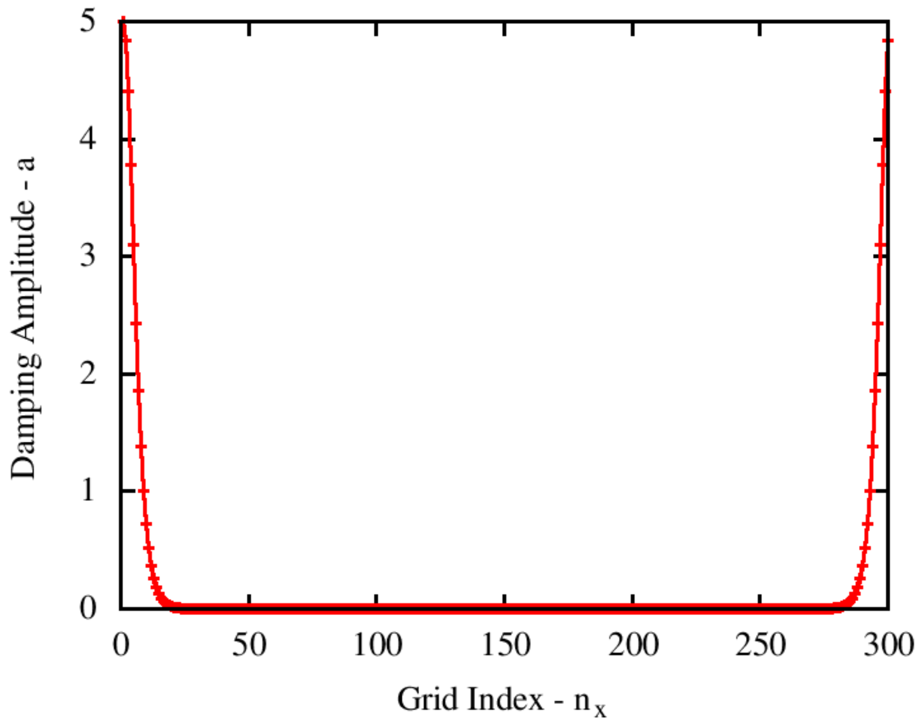

Figure 3.1: Damping function γ at $a = 5.0$ and $\alpha = 0.10$.

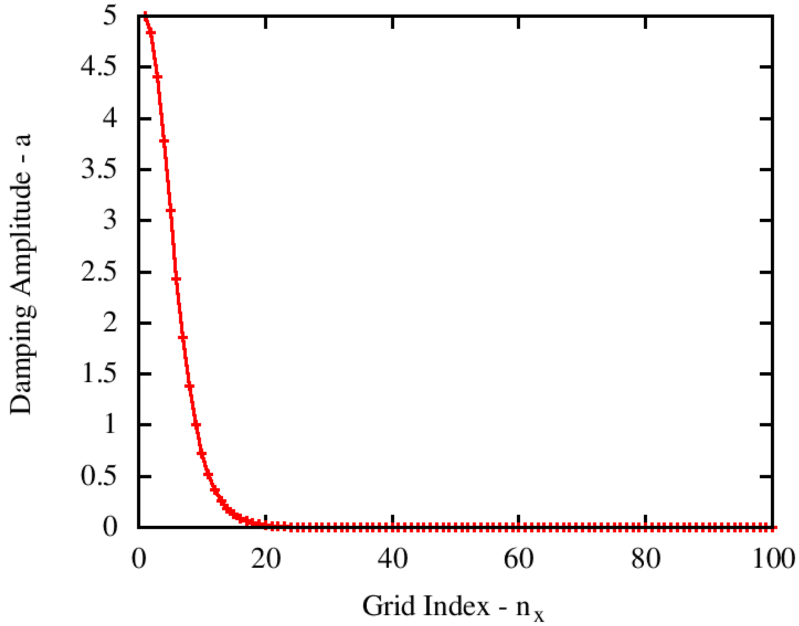

(a)

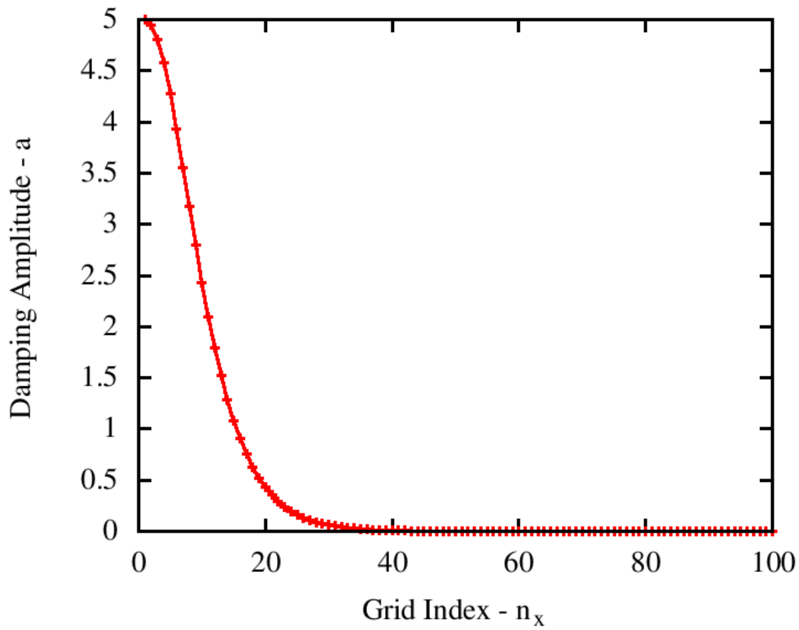

(b)

Figure 3.2: Damping function with different absorbing boundary conditions. (a) γ at $a = 5.0$ and $\alpha = 0.18$. (b) γ at $a = 5.0$ and $\alpha = 0.10$.

3.2 Producing Snapshots with the New FWPS Approach

3.2.1 The Source Function

The mathematical formula for the source function is given by

$$S(t)\delta(x-x_j)\delta(z) = -\sqrt{\frac{2}{\pi}}\sigma\gamma(\sigma - 2\sigma\gamma(\sigma t-\tau)^2)\exp(-\gamma(\sigma t-\tau)^2)\delta(x-x_j)\delta(z), \tag{3.6}$$

where

$\sigma = 1.5 f_{max}$

f_{max} is the maximum frequency (we have used $f_{max} = 20$ Hz)

$\tau = 1$

$\gamma = 8.$

The time-dependance of the source function is given by a Ricker wavelet, a standard source used in the oil and gas industry. Ricker wavelet is a zero-phase wavelet with a central peak and two smaller side lobes. The source function in time and frequency domain are shown in Fig. 3.3. The spatial structure of the source is a Dirac delta function located at $x = x_j$ and $z = 0$.

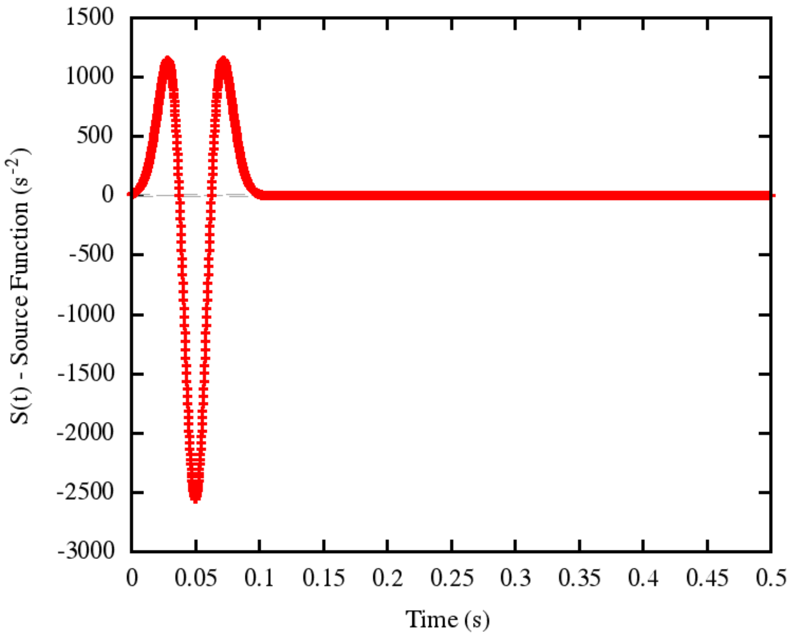

(a)

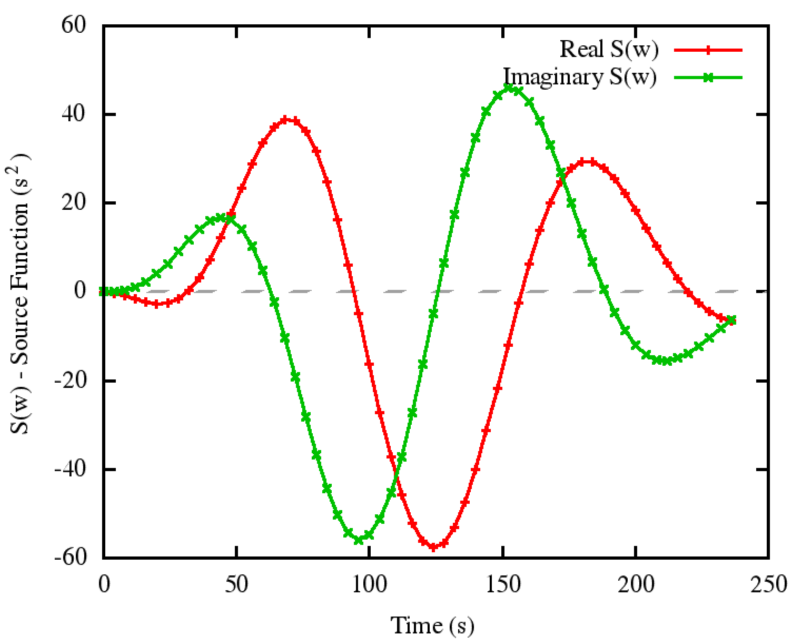

(b)

Figure 3.3: Source function (a) in time domain $S(t)$. (b) in frequency domain $S(\omega)$.

3.2.2 Creating Snapshots in New FWPS Approach

Generating snapshots at different time steps is helpful to analyze the accuracy of the modeling approach. In order to produce snapshots, the pressure values must be calculated in the time domain. We started our derivation by Fourier transforming the acoustic wave equation in to the frequency domain to obtain the Helmholtz equation. Therefore, to produce snapshots, we have to inverse Fourier transform the resulting pressure values into time domain, weighted by the contribution of each frequency to the source. In order to do that, we must return to the full acoustic wave equation and solve it for the case that contains the frequency domain source.

The non-homogeneous acoustic wave equation in the space frequency domain can be written as

$$\frac{\omega^2}{c^2}\tilde{P}(x,z,\omega) + \frac{\partial^2 \tilde{P}(x,z,\omega)}{\partial z^2} + \frac{\partial^2 \tilde{P}(x,z,\omega)}{\partial x^2} = -\hat{S}(\omega)\delta(x-x_j)\delta(z), \tag{3.7}$$

where $\hat{S}$ is the source function in the frequency domain. To include the spatial character of the source properly, $\delta(x-x_j)$ in the Fourier basis can be written as

$$\delta(x-x_j) = \sum_{n=-\infty}^{+\infty} \frac{\exp(2\pi i n(x-x_j)/L)}{L}. \tag{3.8}$$

The (causal) Lippmann-Schwinger solution of Eqn. (3.7) is

$$\tilde{P}(x,z,\omega) = -\hat{S}(\omega)\int_{-\infty}^{+\infty} dz' \int_{-\frac{L}{2}}^{\frac{L}{2}} dx' G^{+}(x,x',z,z',\omega)\delta(x'-x_j)\delta(z'). \tag{3.9}$$

$G^{+}(x,x',z,z',\omega)$ also satisfies a Lippmann-Schwinger equation of the form

$$G^{+}(\mathbf{r},\mathbf{r}',\omega) = G_0^{+}(\mathbf{r},\mathbf{r}',\omega) + \int d\mathbf{r}'' G_0^{+}(\mathbf{r},\mathbf{r}'',\omega)\mathbf{V}(\mathbf{r}'')G^{+}(\mathbf{r}'',\mathbf{r}',\omega). \tag{3.10}$$

The new vector notation denotes: $\mathbf{r} = (x, z)$, $\mathbf{r'} = (x', z')$ and $\mathbf{r}'' = (x'', z'')$. Here, $G_0^+(\mathbf{r}, \mathbf{r'}, \omega)$ satisfies

$$(\frac{\omega^2}{c_0^2} + \frac{\partial^2}{\partial z^2} + \frac{\partial^2}{\partial x^2})G_0^+(\mathbf{r}, \mathbf{r'}, \omega) = \delta(\mathbf{r} - \mathbf{r'}). \tag{3.11}$$

Substituting

$$(\frac{\omega^2}{c^2} + \frac{\partial^2}{\partial z^2} + \frac{\partial^2}{\partial x^2})G^+(x, x', z, z', \omega) = \delta(x - x')\delta(z - z') \tag{3.12}$$

in Eqn. (3.7) gives

$$\begin{aligned}\tilde{P}(x, z, \omega) = &-\hat{S}(\omega) \int_{-\infty}^{+\infty} dz' \int_{-\frac{L}{2}}^{\frac{L}{2}} dx' G_0^+(x, x', z, z', \omega)\delta(x' - x_j)\delta(z') \\ &-\hat{S}(\omega) \int_{-\infty}^{+\infty} dz'' \int_{-\frac{L}{2}}^{\frac{L}{2}} dx'' G_0^+(x, x'', z, z'', \omega)\mathbf{V}(x'', z'')\tilde{P}(x'', z'', \omega).\end{aligned} \tag{3.13}$$

Integrating over x' and z' leads to

$$\begin{aligned}\tilde{P}(x, z, \omega) = &-\hat{S}(\omega)G_0^+(x, x_j, z, 0, \omega) \\ &-\hat{S}(\omega) \int_{-\infty}^{+\infty} dz'' \int_{-\frac{L}{2}}^{\frac{L}{2}} dx'' G_0^+(x, x'', z, z'', \omega)\mathbf{V}(x'', z'')\tilde{P}(x'', z'', \omega).\end{aligned} \tag{3.14}$$

We can show that

$$-\hat{S}(\omega)G_0^+(x, z, x_j, 0, \omega) = -\hat{S}(\omega)\frac{-i}{2} \sum_{n=-\infty}^{\infty} \frac{\exp(ik_n|z|)}{k_n} \frac{\exp(2\pi in(x - x_j))}{L}, \tag{3.15}$$

with

$$k_n = \sqrt{-\frac{\omega^2}{c_0^2} + (\frac{2\pi n}{L})^2}. \tag{3.16}$$

Next, multiplying $P^+(x, z, n, \omega)$ by $\frac{-i}{2k_n}\frac{exp(-2\pi nx_j/L)}{\sqrt{L}}$ and summing over n leads to

$$P^+(x, z, \omega) = \frac{-i}{2} \sum_{n=-N_x}^{N_x} \frac{1}{k_n} \frac{\exp(-2\pi inx_j/L)}{\sqrt{L}} P^+(x, z, n, \omega). \tag{3.17}$$

Finally, the time domain pressure is calculated by Fourier transforming from frequencies to time, weighting the $P^+(x, z, \omega)$ with the Fourier coefficients of the acoustic source dependence $\hat{S}(\omega)$:

$$P^+(x, z, t) = \int_{\omega_{min}}^{\omega_{max}} d\omega \hat{S}(\omega) \exp(i\omega t) P^+(x, z, \omega). \tag{3.18}$$

3.3 Computational Results

3.3.1 Introduction

In the following sections we demonstrate the new FWPS approach by applying it to forward modeling. First, we present the effect of absorbing boundary conditions in new FWPS approach. Next, we produce snapshot results for several different velocity models using a Ricker Wavelet for the time-dependance of the source. We have presented the snapshot results with and without absorbing boundary conditions applied.

3.3.2 Velocity Models

We have used several velocity models to test our new FWPS approach to solve the Helmholtz acoustic wave equation. The first and simplest velocity model is a two-dimensional homogeneous velocity model with a uniform velocity equal to 2000 m/s. The second model is an arbitrary varying velocity structure called steep velocity model which is shown in Fig. 3.4(a). In the steep model the lightly shaded region has velocity 4500 m/s and the dark region has velocity 2000 m/s. The third velocity model is a realistic earth velocity model which consists of a portion of the BP P-wave velocity model. It is also an arbitrary varying velocity structure with a complex shaped high velocity region and slow velocity varying sediment layers. The BP P-wave velocity model is shown in Fig. 3.4(b). In each case, the model size was 601 points along the z-direction and $2N_x+1 = 301$ grid points along the x-direction. For the BP P-wave velocity model only, a low velocity part at the bottom has been added to provide compact support in z. We have used grid spacings $dz = 1.5$ m and $dx = 10$ m. The reference velocity was chosen to be $c_0 = 2000.0$ m/s for the homogeneous and steep velocity models. For the BP P-wave velocity model the reference velocity was $c_0 = 1492.0$ m/s, the velocity of the sea water layer.

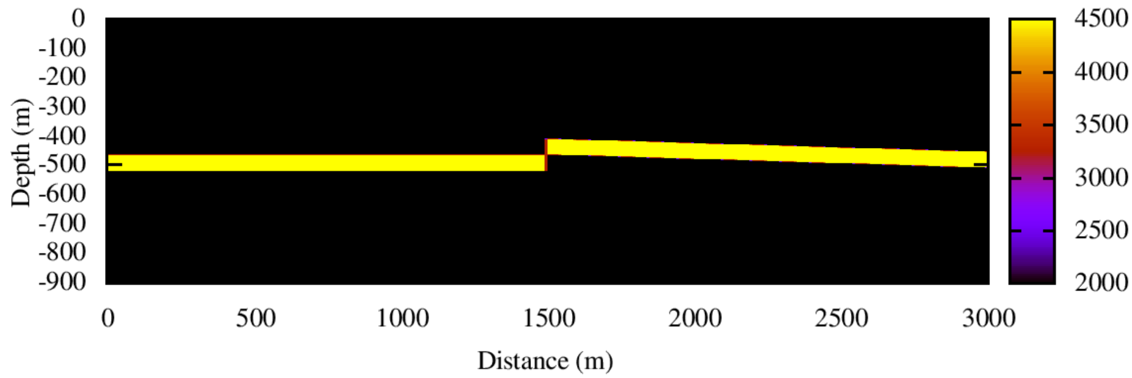

(a)

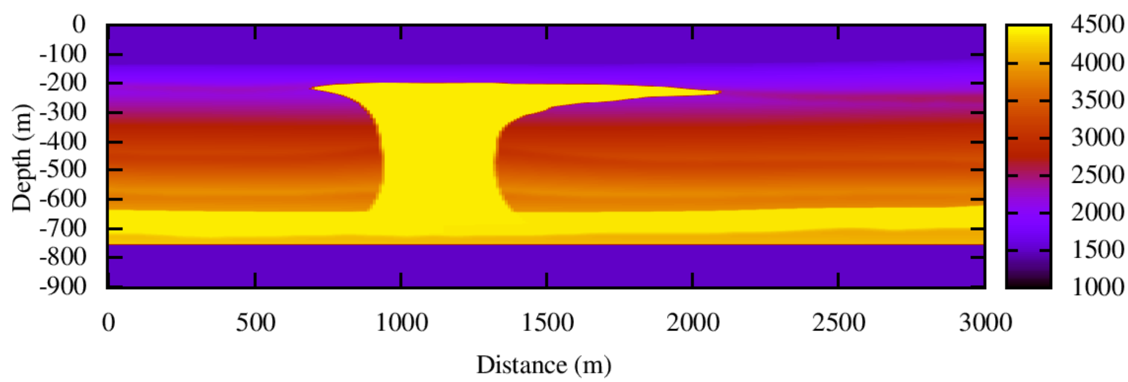

(b)

Figure 3.4: P-wave velocity models. We have plotted the wave velocity against (Depth, Distance). Color bar shows the wave velocity values in m/s. (a) Steep velocity model. (b) BP P-wave velocity model.

3.3.3 Absorbing Boundary Conditions Results

We have used both Eqns. (3.2) and (3.5) to implement the boundary conditions in the new FWPS solution. We found them both to provide almost the same results. But to demonstrate the effectiveness of the absorbing boundary condition we primarily use the formalism given in (3.5), since compared to (3.2) it doesn't involve many γ inversions, hence saving some computational time. To present the results, we have used the propagating wavefield in the frequency domain, $P(x, z, \omega)$. In all the figures, the frequency dependance pressure wavefield data are normalized by the largest value of the corresponding data field.

Figure 3.5 displays the pressure wavefield $P(x, z, \omega)$ at frequency 50.91 Hz for the homogeneous velocity medium without absorbing boundary conditions applied. It clearly displays strong, unwanted boundary effects.

Figure (3.6) shows the pressure wave field $P(x, z, \omega)$ for the homogeneous velocity medium with different absorbing boundary conditions. In those figures we have kept the damping amplitude value $a = 5.0$ and changed the α values. Figures 3.6(a) and 3.6(b) have α values 0.18 and 0.07 respectively. These α values correspond to employing ~ 20 and ~ 50 grid points in the absorbing boundary region. It can be seen from those graphs that fewer artificial reflections are produced when decreasing α, and in turn increasing the damping region. Figures 3.6(a) and 3.6(b) indicate a clear improvement compared to Fig. 3.5.

Next, we have applied the absorbing boundary conditions for the steep velocity model as similarly to the homogeneous case. Figure 3.7 displays the pressure

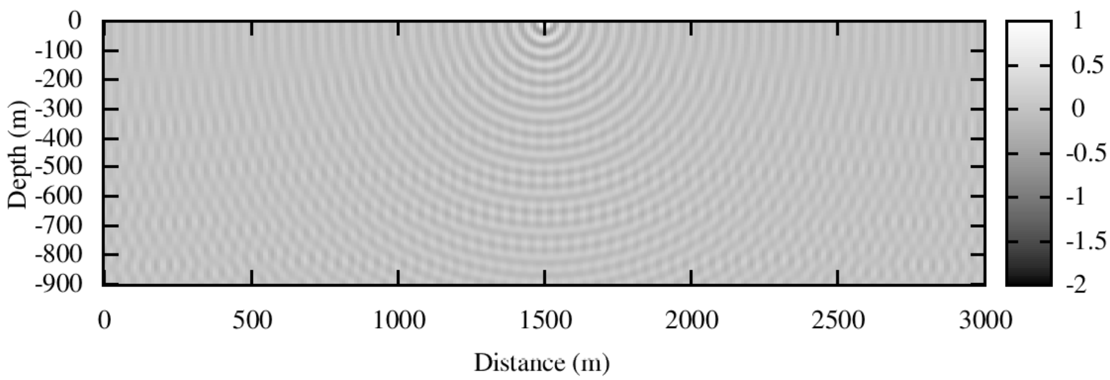

Figure 3.5: Pressure wavefield for the homogeneous model at 50.91 Hz without absorbing boundary conditions applied. We have plotted the pressure amplitude against (Depth, Distance). Grayscale bar shows the values of normalized pressure wavefield data.

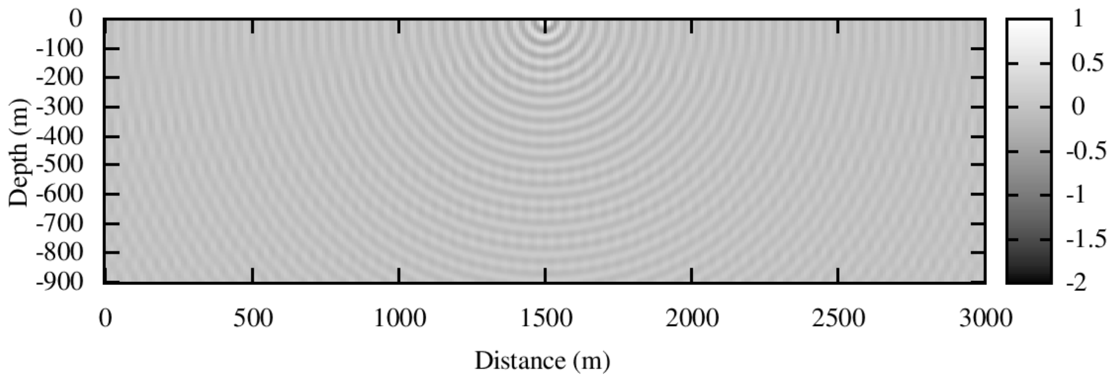

(a)

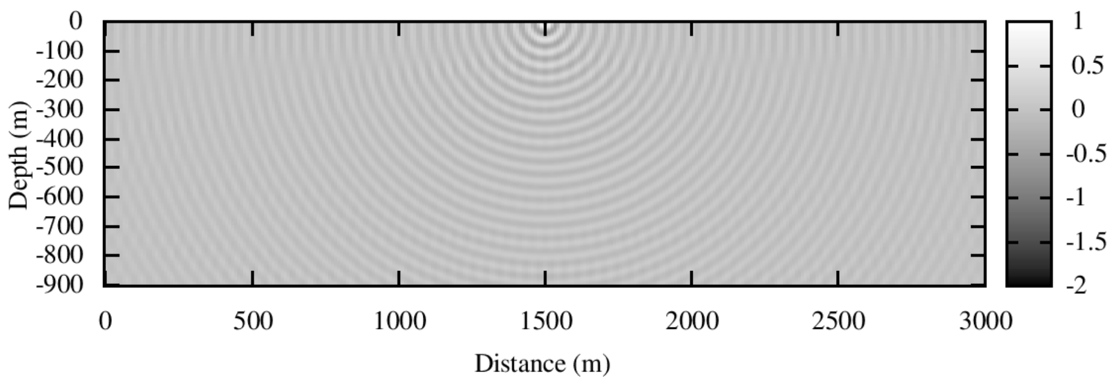

(b)

Figure 3.6: Pressure wavefield for homogeneous model at 50.91 Hz for different absorbing boundary conditions. We have plotted the pressure amplitude against (Depth, Distance). In both figures, grayscale bar shows the values of normalized pressure wavefield data. (a) $\alpha = 0.18$. (b) $\alpha = 0.07$.

wavefield $P(x, z, \omega)$ at frequency 50.91 Hz for the steep velocity medium without any absorbing boundary conditions applied. Figure 3.8 displays the pressure wave field $P(x, z, \omega)$ at frequency 50.91 Hz for the steep velocity medium with different absorbing boundary conditions applied. We have kept the damping amplitude value $a = 5.0$ and changed the α values. Figures 3.8(a) and 3.8(b) have α values 0.18 and 0.07 respectively correspond to employing ~ 20 and ~ 50 grid points in the absorbing boundary region. The two sets of graphs for the steep velocity model show improvement as in the previous homogeneous case.

Using Kosloff's method of absorbing boundary conditions we were able to effectively dealt with the boundary effects in new FWPS solution . It shows that well known seismic techniques can be easily applied in new FWPS method solution to reduce artificial reflections. The solution to avoiding boundary effects used to be to enlarge the numerical mesh, thus delaying the side reflections and wraparound longer than the range of times involved in the modeling. Obviously this solution considerably increases the computation time. Thus choosing Kosloff's method, at the same time we were able to save some computational time.

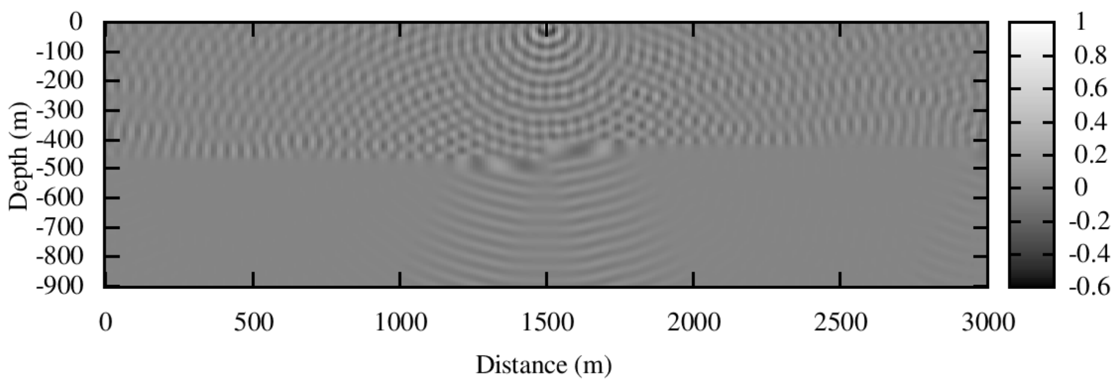

Figure 3.7: Pressure wavefield for the steep velocity model at 50.91 Hz without absorbing boundary conditions applied. We have plotted the normalized pressure amplitude against (Depth, Distance). Grayscale bar shows the values of normalized pressure wavefield data.

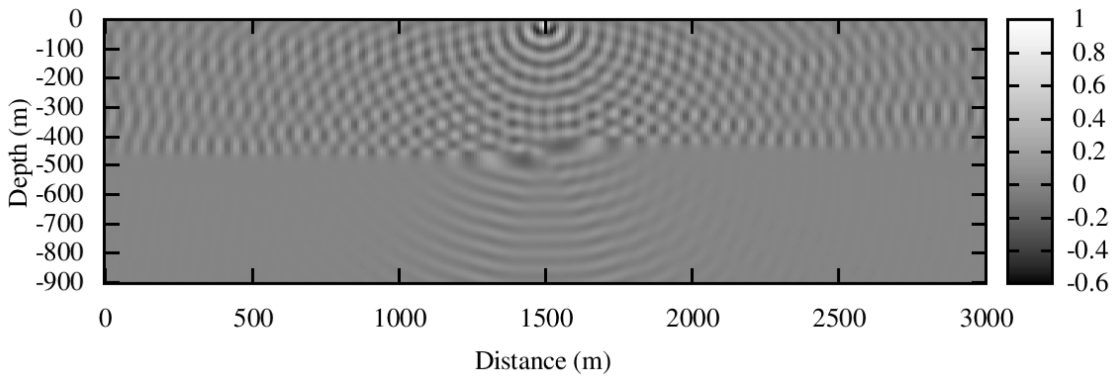

(a)

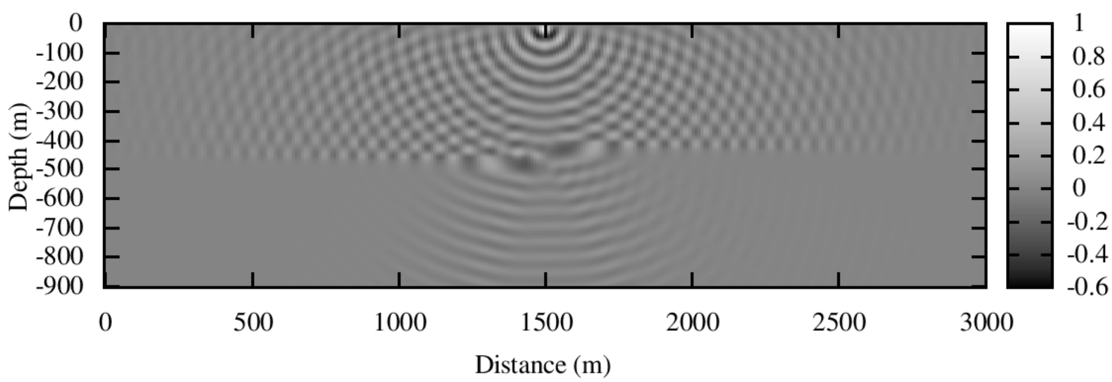

(b)

Figure 3.8: Pressure wavefield for the steep velocity model at 50.91 Hz for different absorbing boundary conditions. We have plotted the pressure amplitude against (Depth, Distance). In both figures, grayscale bar shows the values of normalized pressure wavefield data. (a) $\alpha = 0.18$. (b) $\alpha = 0.07$.

3.3.4 New FWPS Approach Modeling Results

In this section we verify the new FWPS approach by applying it to forward modeling. We present the results for the three different velocity models given in Section 3.3.2. To produce snapshots, we have used the source function given in Eqn. (3.6). We have Fourier transformed the time dependent source $S(t)$ to the frequency domain $\hat{S}(\omega)$ and set a cutoff frequency for which the value of $\hat{S}(\omega)$ is very small. For this time domain source function, we have taken a frequency range from $\frac{0.001}{2\pi}$ Hz to $\frac{300}{2\pi}$ Hz. We have computed solutions for 80 different frequencies lying in this range, with a constant interval $\Delta\omega = \frac{4}{2\pi}$ Hz. The larger the number of frequencies taken into account in the calculation, over a given frequency range, clearer the snapshot. To obtain snapshots, after finding $P^+(n', z, n, \omega)$, we have calculated $P^+(x, z, n, \omega)$ by using Eqn. (2.36). Then, frequency dependent pressure values $P^+(x, z, \omega)$ were calculated by Eqn. (3.3). Finally the snapshots $P^+(x, z, t)$ were obtained using Eqn. (3.4). The time step was chosen to obey the stability condition, the Courant Friedriches Lewy condition (CFL condition) [57]. It is chosen to be less than a value determined by the CFL condition to obtain clear snapshots for the wave propagation at different times. Define

$$\alpha = \frac{c}{(dx/dt)} = \frac{2}{\pi}, \tag{3.19}$$

where c is the maximum velocity in the propagating medium, dt is the time step, dx is the maximum grid spacing and α is the Courant number. We have used $\alpha < 0.2$ for our work.

3.3.5 Snapshots for Homogeneous Velocity Model Without Absorbing Boundary Conditions Applied

The snapshots for the homogeneous velocity model at times 0.2 s to 0.5 s are shown in the following figures from Fig. 3.9(a) to Fig. 3.9(d). No absorbing boundary conditions are applied when obtaining these snapshots. Unwanted artifacts are clearly seen in these figures. We have normalized the wavefield amplitude data of each figure by the largest value of the amplitude of that particular data set.

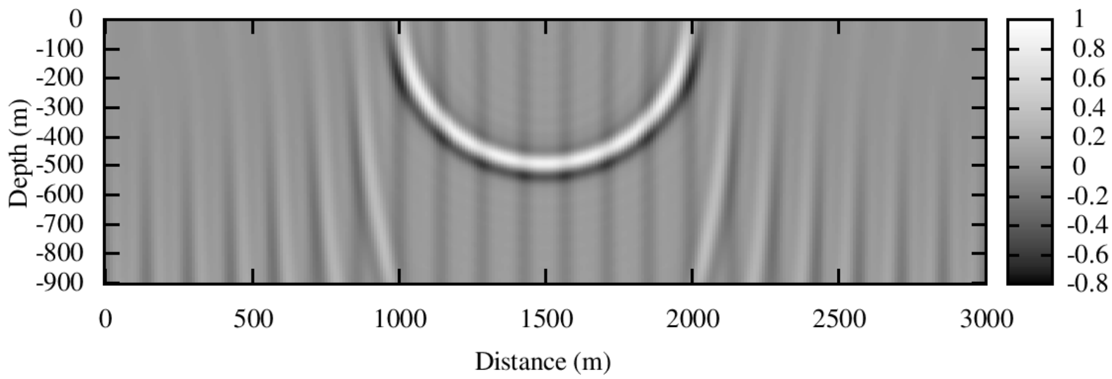

(a)

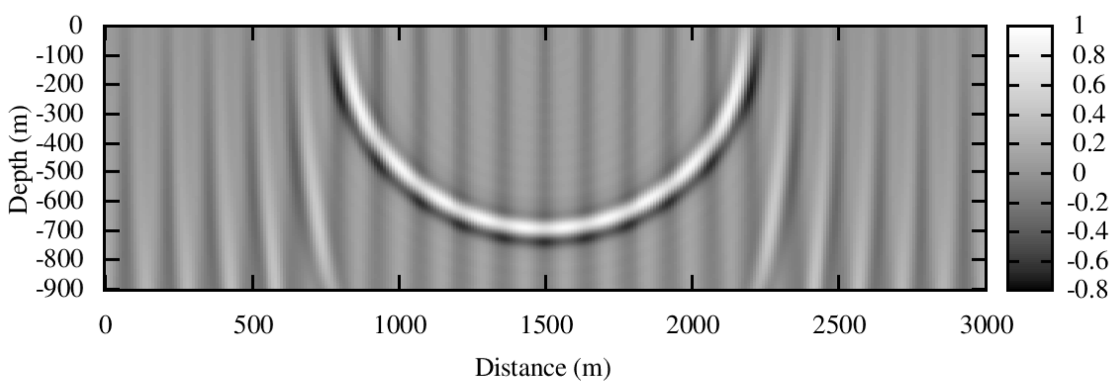

(b)

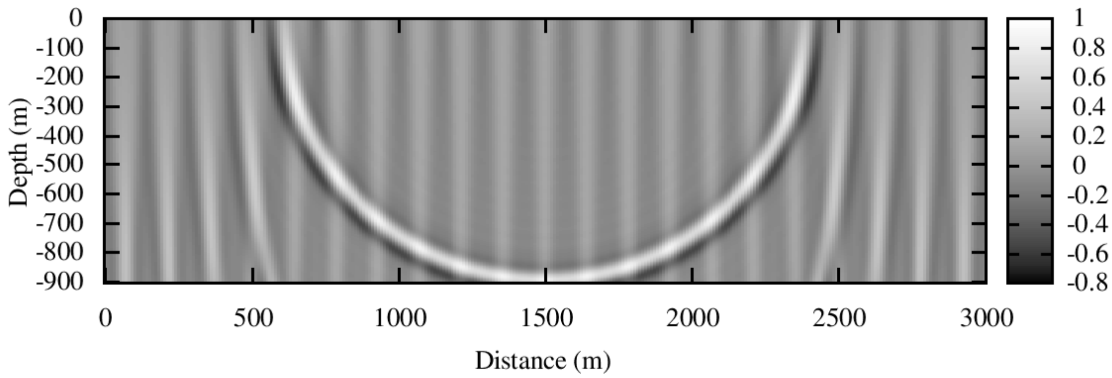

(c)

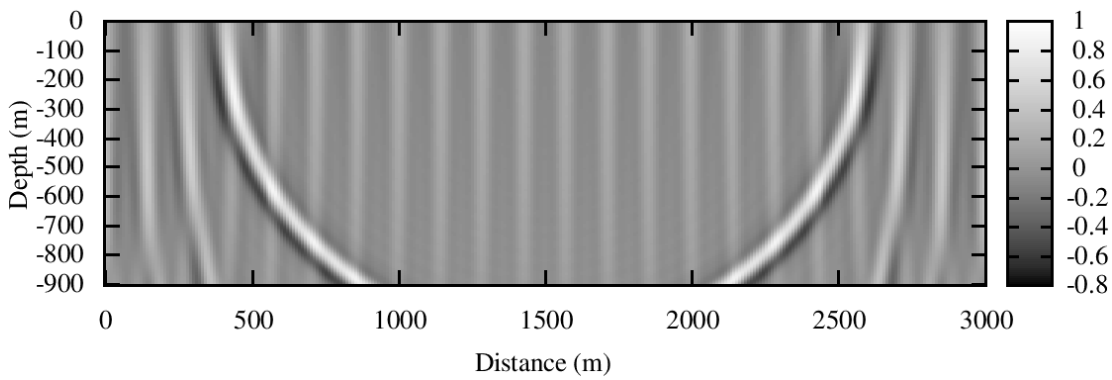

(d)

Figure 3.9: Snapshots for the homogeneous velocity model using new FWPS approach without absorbing boundary conditions applied. We have plotted the pressure amplitude against (Depth, Distance). In each of the figures, grayscale bar shows the values of normalized pressure wavefield amplitudes. (a) $t = 0.20$ s. (b) $t = 0.30$ s. (c) $t = 0.40$ s. (d) $t = 0.50$ s.

3.3.6 Snapshots for Homogeneous Velocity Model with Absorbing Boundary Conditions Applied

The snapshots for the homogeneous velocity model at times 0.2 s to 0.5 s are shown in the following figures from Fig. 3.10(a) to Fig. 3.10(d). We have used 50 points of absorbing region when obtaining these snap shots. We have normalized the wavefield amplitude data of each figure by the largest value of the amplitude of that particular data set.

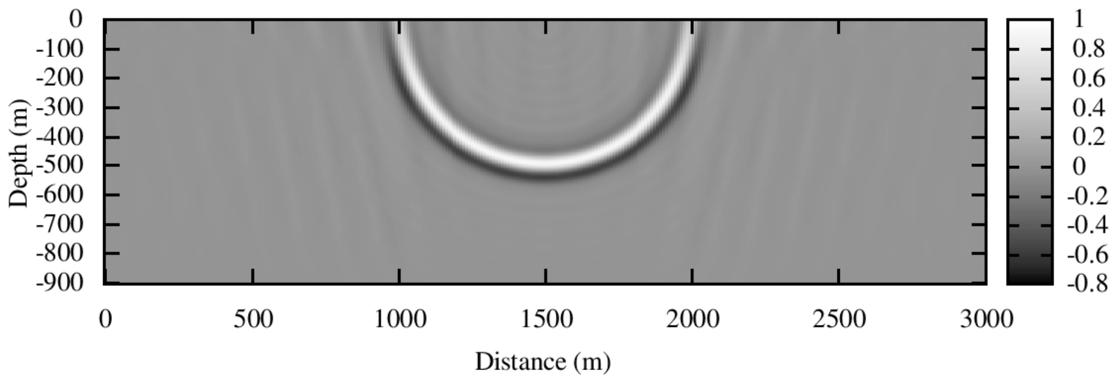

(a)

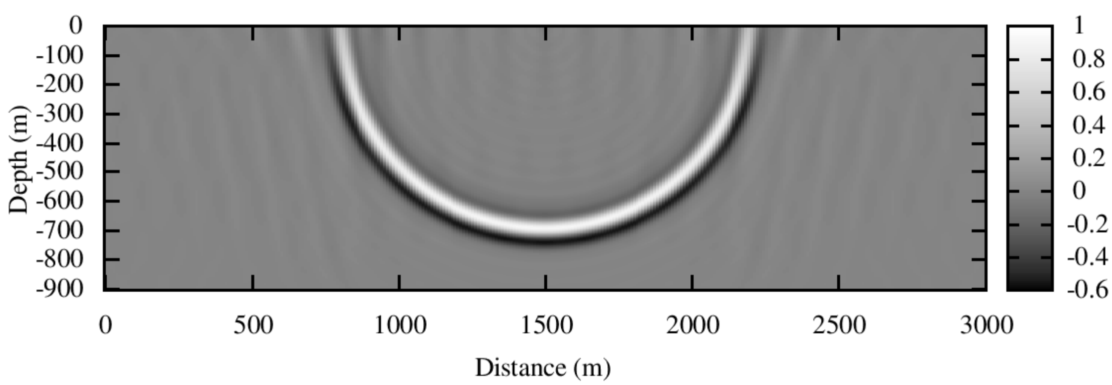

(b)

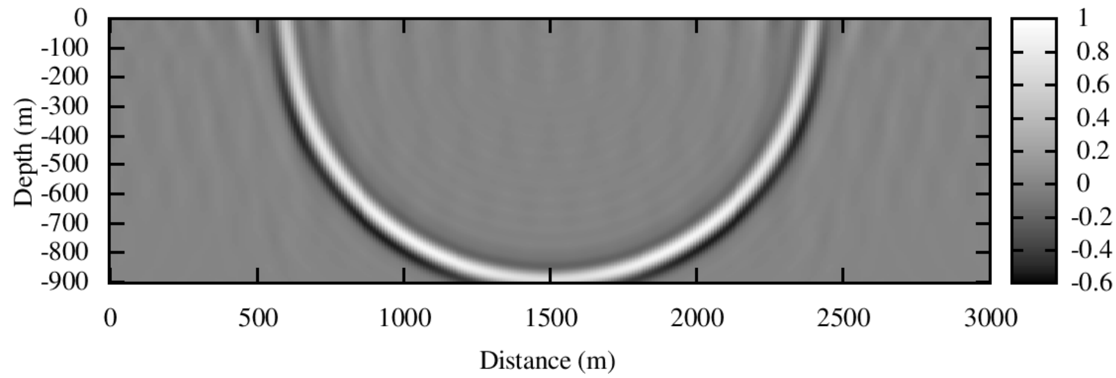

(c)

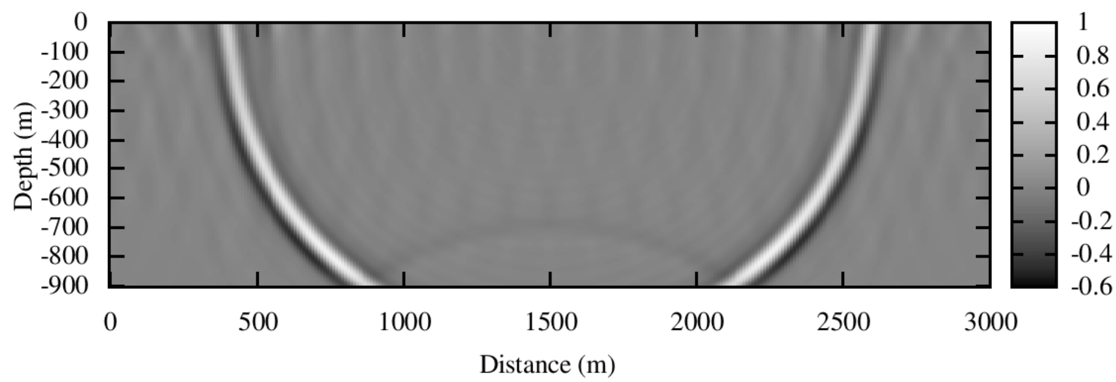

(d)

Figure 3.10: Snapshots for the homogeneous velocity model using new FWPS approach with absorbing boundary conditions applied. We have plotted the pressure amplitude against (Depth, Distance). In each of the figures, grayscale bar shows the values of normalized pressure wavefield amplitudes. (a) $t = 0.20$ s. (b) $t = 0.30$ s. (c) $t = 0.40$ s. (d) $t = 0.50$ s.

3.3.7 Snapshots for Steep Velocity Model with Absorbing Boundary Conditions Applied

The snapshots for the steep velocity model at times 0.10 s to 0.50 s are shown in the following figures from Fig. 3.11(a) to Fig. 3.11(e). We have used 50 points of absorbing region when obtaining these snap shots. We have normalized the wavefield amplitude data of each figure by the largest value of the amplitude of that particular data set.

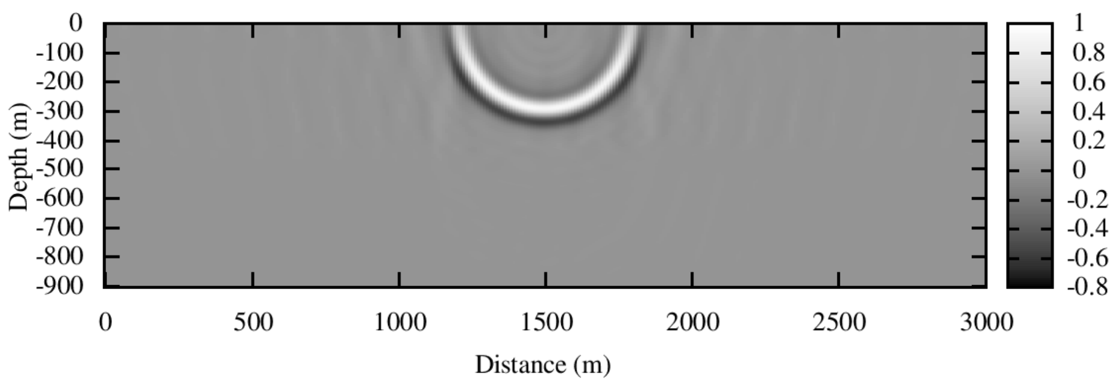

(a)

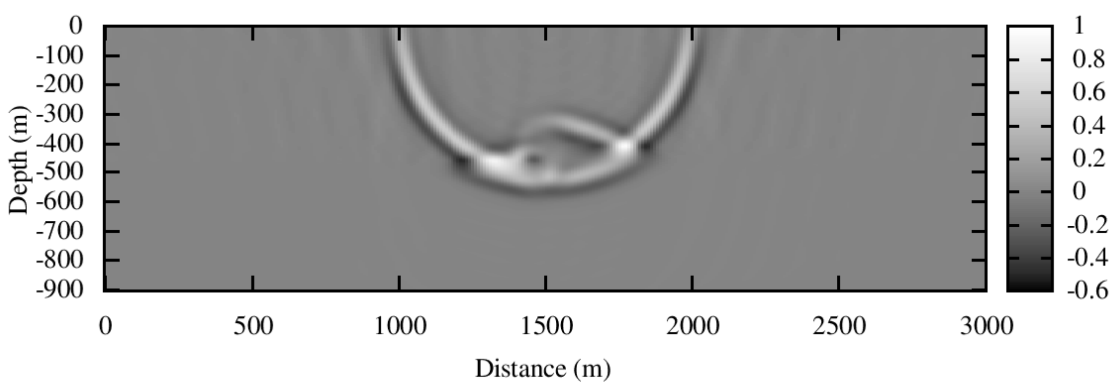

(b)

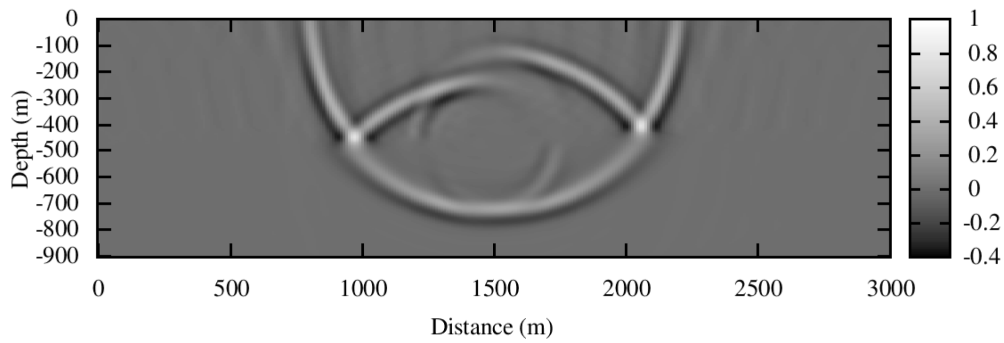

(c)

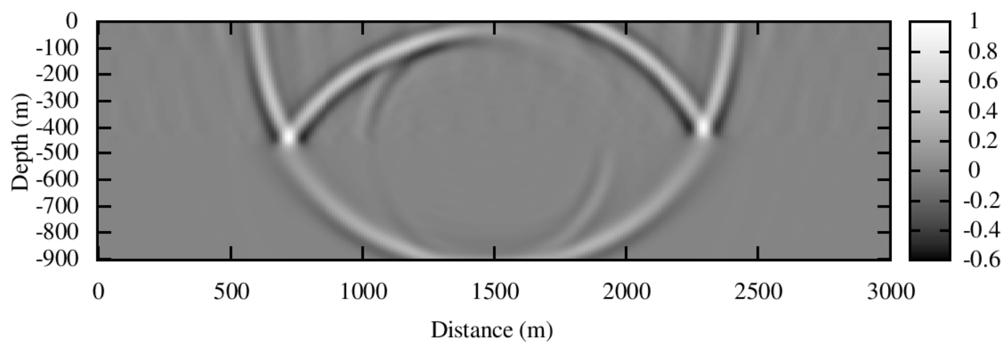

(d)

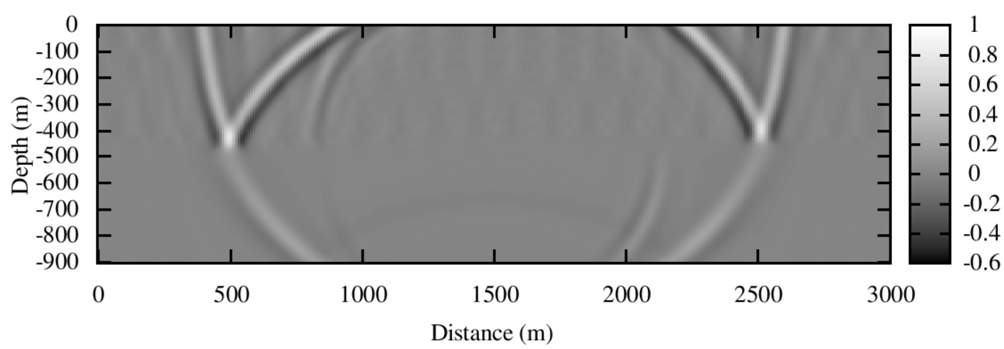

(e)

Figure 3.11: Snapshots for the steep velocity model using new FWPS approach with absorbing boundary conditions applied. We have plotted the pressure amplitude against (Depth, Distance). In each of the figures, grayscale bar shows the values of normalized pressure wavefield amplitudes. (a) $t = 0.10$ s. (b) $t = 0.20$ s.(c) $t = 0.30$ s. (d) $t = 0.40$ s. (e) $t = 0.50$ s.

3.3.8 Snapshots for BP P-wave Velocity Model with Absorbing Boundary Conditions Applied

The snapshots for the substantially more complicated BP P-wave velocity model at times 0.20 s to 0.30 s are shown in the following figures from Fig. 3.12(a) to Fig. 3.12(c). We have used 50 points of absorbing region when obtaining these snap shots. We have normalized the wavefield amplitude data of each figure by the largest value of the amplitude of that particular data set. The low velocity part at the bottom has been removed when presenting the results.

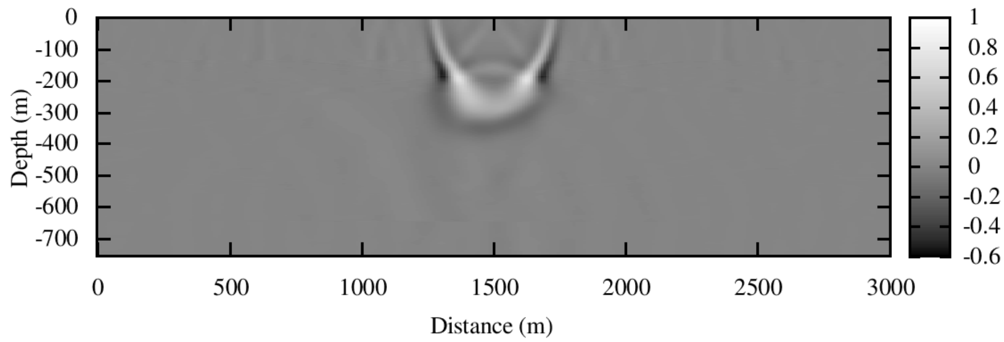

(a)

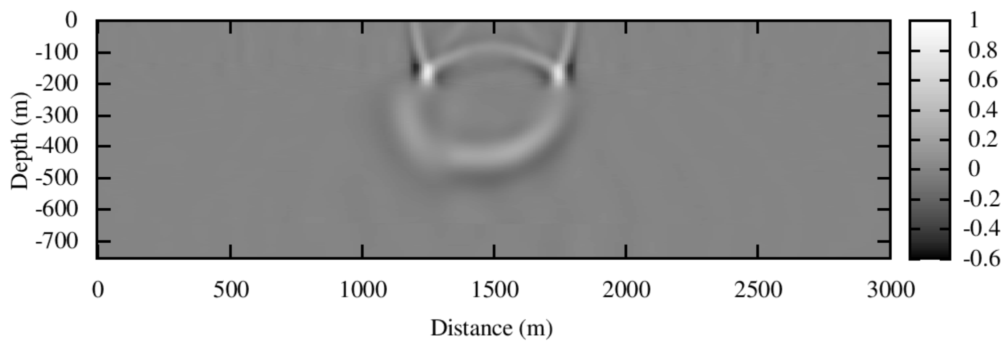

(b)

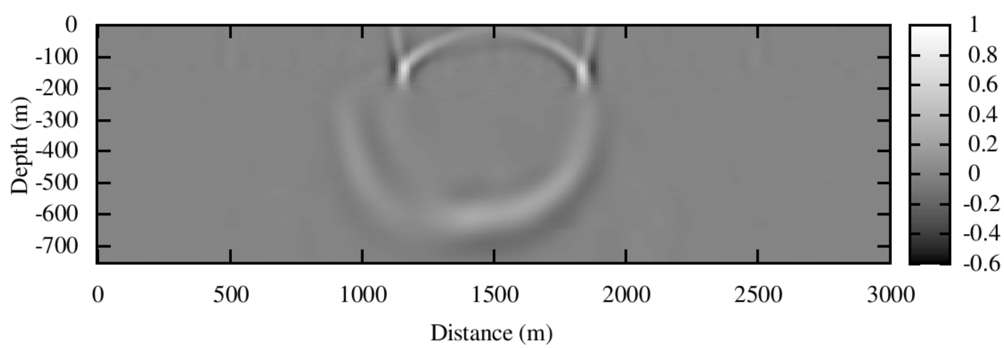

(c)

Figure 3.12: Snapshots for the BP P-wave velocity model using new FWPS approach. We have plotted the pressure amplitude against (Depth, Distance). In each of the figures, grayscale bar shows the values of normalized pressure wavefield amplitudes. (a) $t = 0.20$ s. (b) $t = 0.25$ s. (c) $t = 0.30$ s.

3.3.9 Snapshots for BP P-wave Velocity Model Obtained Using Finite Difference Method

The snapshots for the BP P-wave velocity model obtained using finite difference (FD) method are shown in the following figures from Fig. 3.13(a) to Fig. 3.13(c). We have normalized the wavefield amplitude data of each figure by the largest value of the amplitude of that particular data set.

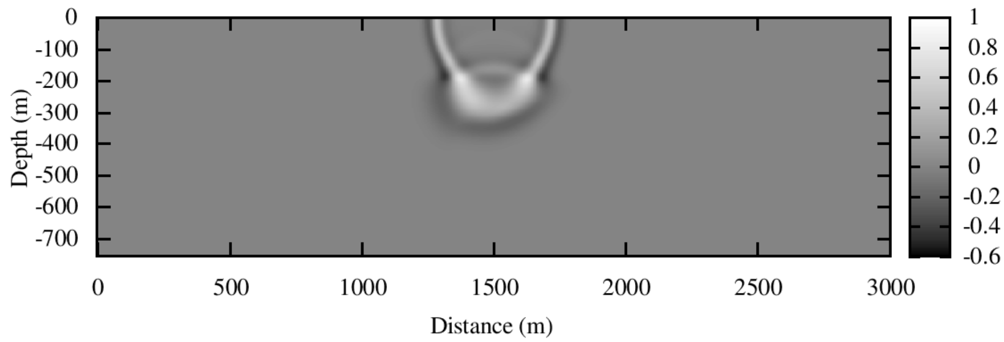

(a)

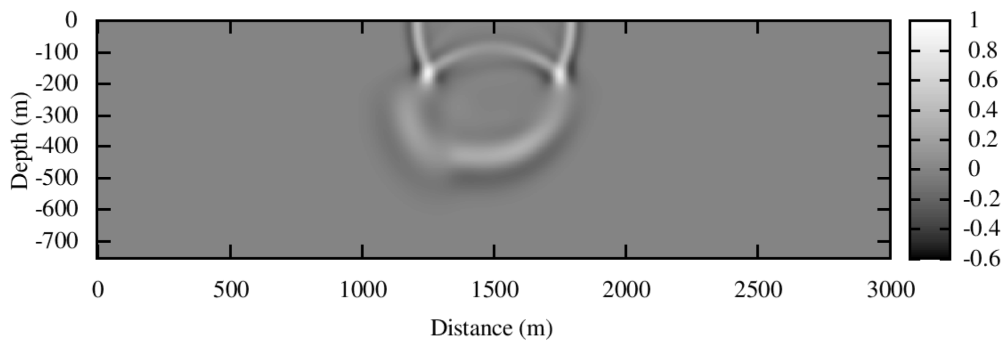

(b)

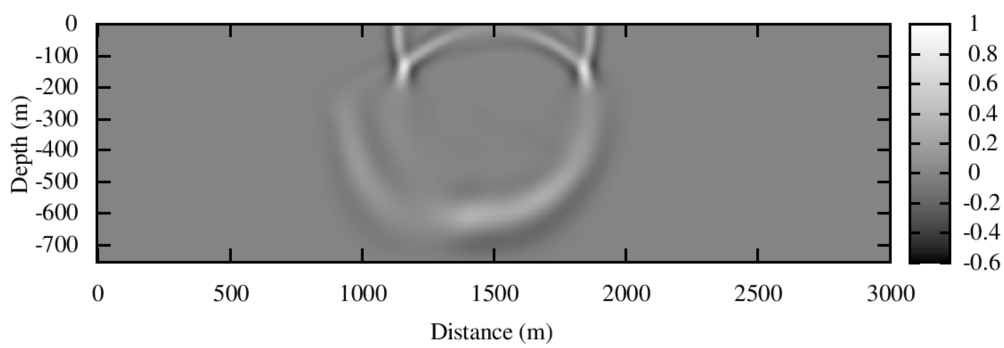

(c)

Figure 3.13: Snapshots for the BP P-wave velocity model using FD method. We have plotted the pressure amplitude against (Depth, Distance). In each of the figures, grayscale bar shows the values of normalized pressure wavefield amplitudes. (a) $t = 0.20$ s. (b) $t = 0.25$ s. (c) $t = 0.30$ s.

From Fig. 3.11 and Fig. 3.12, it is clearly visible that the scattering at the boundaries are correctly treated by the new FWPS approach. Furthermore, Fig. 3.11 show both up and down propagating waves, validating the full-wave propagation in new FWPS approach. To further validate the new FWPS results, in Fig. 3.13, we present the FD snapshot results for the BP P-wave velocity model. Comparing Fig. 3.12 to that of Fig. 3.13 we observe the snapshot results are very similar. This further demonstrates that new FWPS approach provides a accurate solution to the full-wave equation. Our method produces accurate travel times and treats the reflector locations in complex geologic structures correctly, providing kinamatically correct results. However, it does not provide the same amplitude as in FD method. The amplitude errors in one-way wave type wave equations are usually related to their failure to conserve energy [58]. Therefore, introduction of a new term associated with the amplitudes as in "true-amplitude phase-shift method" may be needed to get the correct dynamics [58, 59, 60].

Chapter 4

Evanescent Waves in the BP P-wave Velocity Model

4.1 Introduction

If we carry out the full formal solution to the wave equation, we must mathematically include waves for which $\omega^2/c_0^2 < (\frac{2\pi n}{L})^2$ to satisfy the requirement for completeness of the basis. At least some of these states are needed to describe the distortion of the pressure wave caused by lateral inhomogeneity in the acoustic velocity. They also are required to describe the source correctly. This leads to the occurrence of exponentially growing and decaying waves. The physical reason for instability is the amplification caused by the growing evanescent waves that leads to a rapid "blow-up" of the solution, making it necessary to suppress these unwanted wave modes in one-way extrapolation algorithms. Kosloff and Baysal [35] suggested suppressing all of the evanescent waves in the wavenumber domain by using the Fourier transform and a simple ideal cutoff filter for a background with depth-only dependent velocity and a zero offset source-receiver configuration. This strategy lead to the removal of some propagating waves along with the evanescent waves and, as a result, poor imaging of steep reflectors. Sandberg and Beylkin [61] extended this method to suppresses evanescent modes in an arbitrary laterally varying background by introducing spectral projectors to remove the evanescent modes, hence, leaving all propagating modes intact in a variable background. This is computationally intensive as it requires matrix diagonalizations to construct the projectors. It does, however, deliver a correct image.

In physical reality, both solutions with harmonic oscillations (propagating waves) and exponentially decaying (evanescent) waves with depth are present. Therefore, removing all the evanescent waves affects the resolution and consequently the final image. Thus it is useful to seek a less costly method to filter out only the exponentially growing evanescent waves. It is clearly observed from the Eqn. (2.16) that the eigenvalues of the matrix $\mathbf{M}$ are either purely real or purely imaginary depending on the values of $\{\lambda_i\}$s. The pure real waves include wave numbers k_n^2 satisfying the relation $\omega^2/c_0^2 < (\frac{2\pi n}{L})^2$. They are the wave numbers associated with the exponentially growing or decaying evanescent waves. The negative real eigenvalues lead to an exponential decay as z increases and the positive real eigenvalues grow exponentially. The stabilizing method (Feshbach projection-operator method) proposed by Kouri *et al.* requires no expensive diagonalization and only removes the exponentially growing evanescent waves corresponding to these positive real eigenvalues while retaining all the propagating and exponentially decaying waves. With the use of this method, now we are able to identify the significance of the evanescent waves in realistic earth models.

4.2 Computational Results

To test the significance of the evanescent waves we have used the BP P-wave velocity model shown in Fig.3.4(b). The model size is 601 points along the z-direction and $2N_x + 1 = 301$ grid points along the x-direction. We have added 150 points of sea water layer to the bottom of the z-direction to provide compact support for the velocity model. We have used grid spacings $dz = 1.5$ m and $dx = 10$ m. The initial reference velocity was $c_0(z_0) = 1492.0$ m/s and the minimum velocity for each layer was used to calculate the projection matrix at each depth step z.

The snapshots including both propagating and decaying evanescent waves are shown in Fig. 3.12(a) to Fig. 3.12(c). The snapshots including only propagating waves for times $t = 0.20$ s, $t = 0.25$ s and $t = 0.30$ s are shown in Fig. 4.1(a) to Fig. 4.1(c). Figure (4.2)(a) to Fig. (4.2)(c) show the difference of above two sets of snapshot figures. These snapshots, show propagation of decaying evanescent waves. Although the amplitude of the evanescent wave is less than that of the propagating wave, there is still a significant contribution from them. Removing all these decaying evanescent waves would indeed affect the quality of the final result.

To validate our results, we also include the reflection amplitude $r_{n,n'}$ data for a single frequency of 43.64 Hz. Figure (4.3) contain the reflection amplitude $r_{n,n'}$

for the case with both propagating and decaying evanescent waves. Figure (4.4) contain the reflection amplitude $r^0_{n,n'}$ for the case with only propagating waves. Figure (4.5) contain the difference of reflection amplitudes $r_{n,n'} - r^0_{n,n'}$. Here, the index n' corresponds to the dependence in the lateral variation x and the second index n corresponds to the dependence on the lateral position of the source x_0. Note from Figure (4.4) the contribution of evanescent waves are due to the large wave numbers corresponding to the larger values of $\pm N_x$. For comparison we also include reflection amplitude $r_{n,n'}$ data for a smaller frequency of 14.55 Hz. The reflection amplitudes are shown in Fig. (4.6) and Fig. (4.8).

Our new FWPS approach yields a stable solution that suppresses only growing evanescent waves. Our study of decaying evanescent waves shows that they are important physically and that their presence is not just a theoretical artifact. Their presence can be observed in the wave propagation of realistic BP earth model.

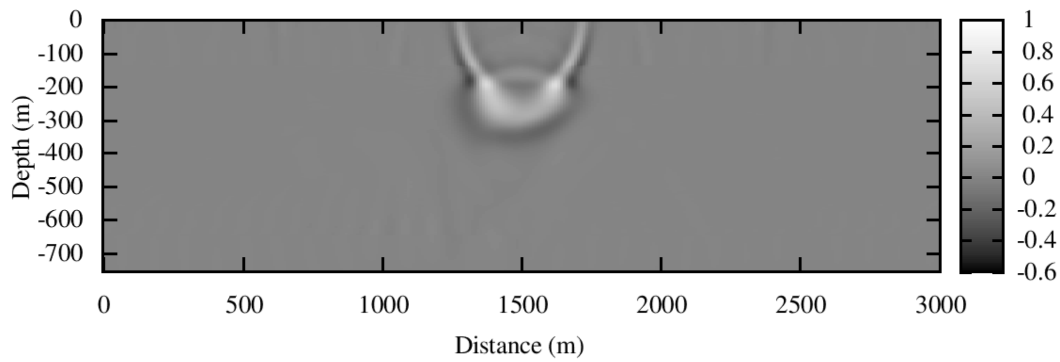

(a)

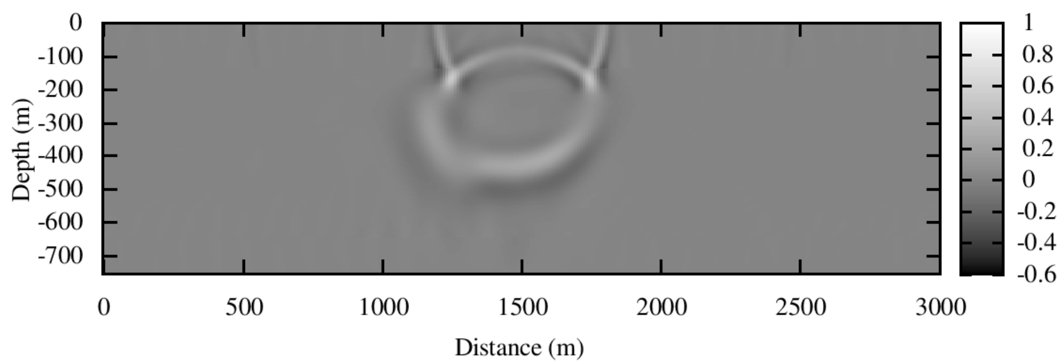

(b)

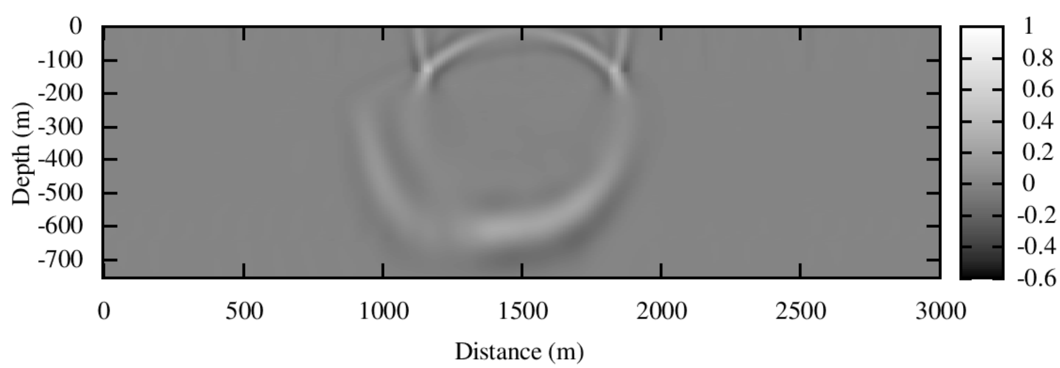

(c)

Figure 4.1: Snapshot with only propagating waves at (a) $t = 0.20$ s. (b) $t = 0.25$ s. (c) $t = 0.30$ s. We have plotted the pressure amplitude against (Depth, Distance). In each of the figures, grayscale bar shows the normalized pressure wavefield amplitude values.

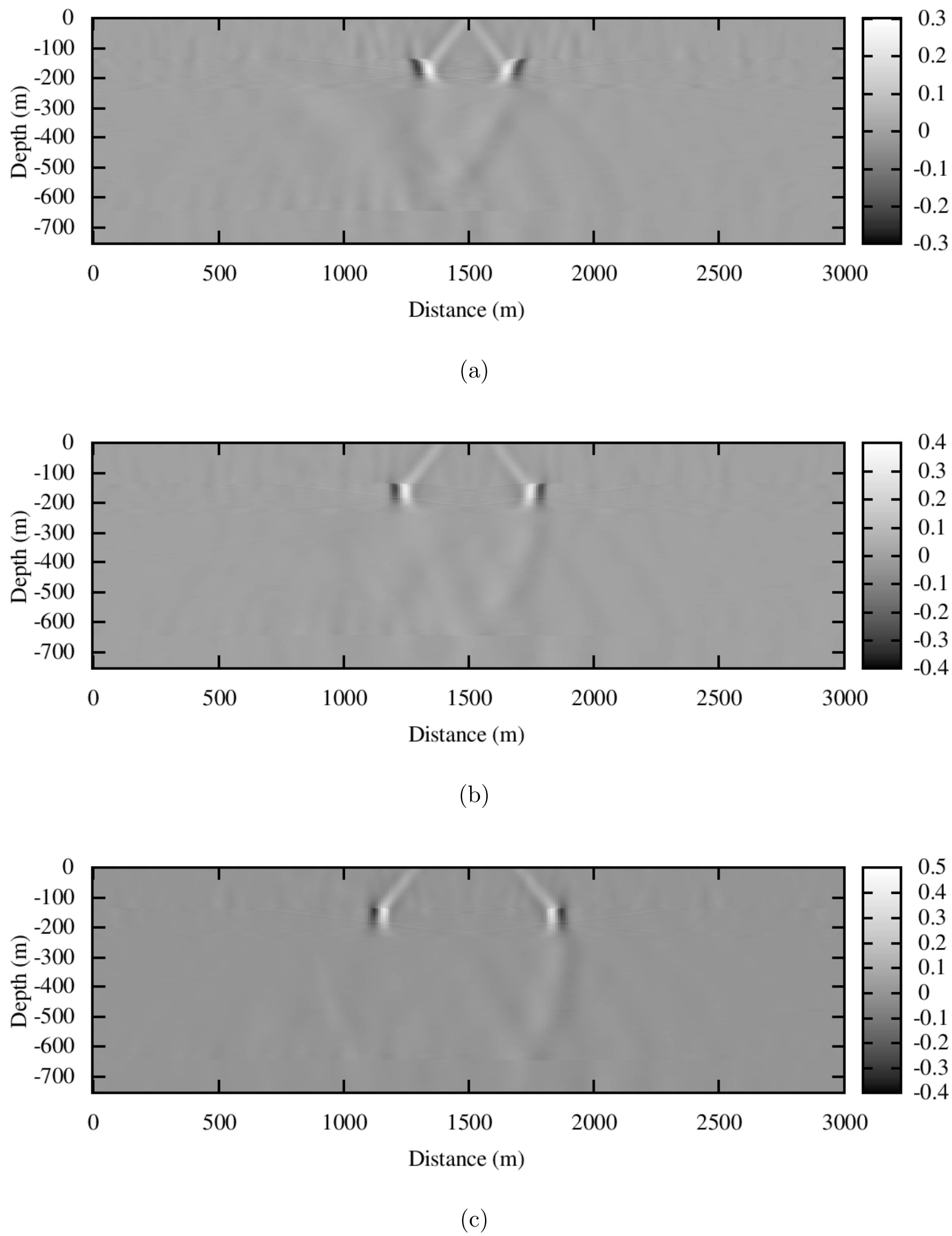

Figure 4.2: Difference of snapshot figures Fig. 3.12(a)-(c) and Fig. 4.1(a)-(c) at (a) t = 0.20 s. (b) t = 0.25 s. (c) t = 0.30 s. We have plotted the pressure amplitude difference against (Depth, Distance). In each of the figures, grayscale bar shows the normalized pressure wavefield amplitude values.

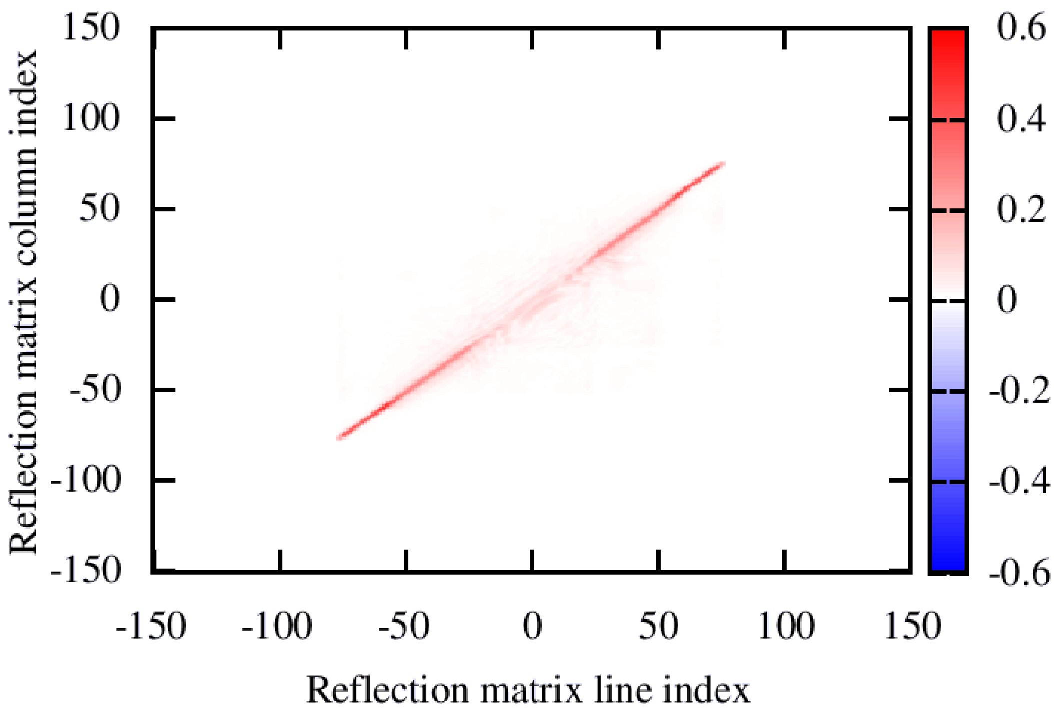

Figure 4.3: Reflection amplitude ($\mathbf{r}_{n,n'}$) data with both propagating and decaying evanescent waves at $f = 43.64$ Hz, plotted against (Column index, Line index). Color bar shows the values of dimensionless reflection amplitude $\mathbf{r}_{n,n'}$.

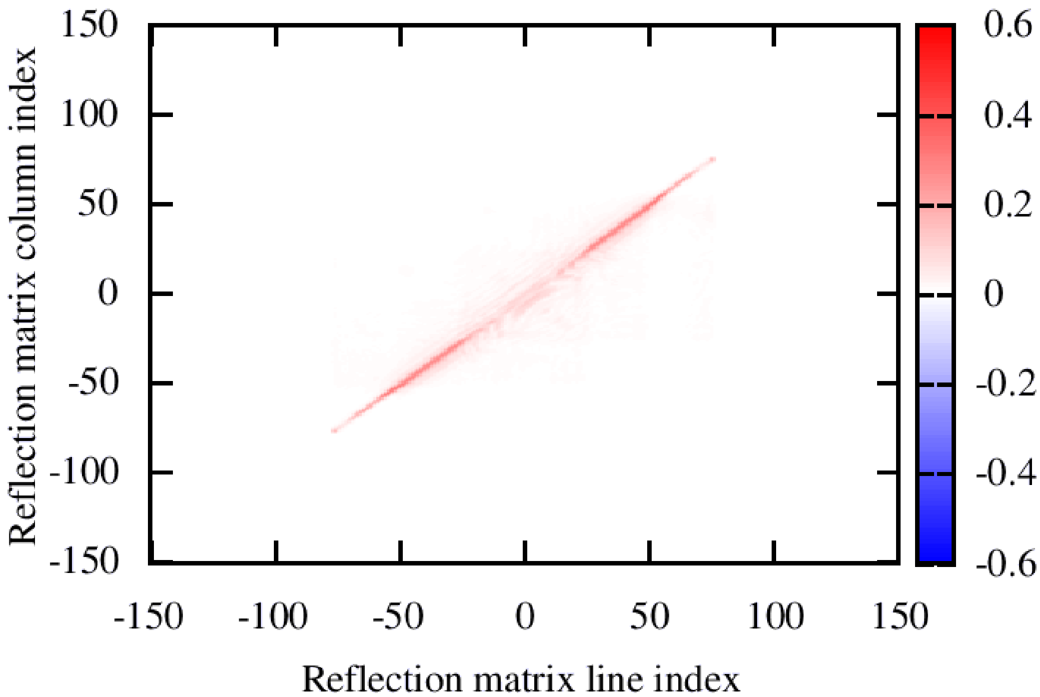

Figure 4.4: Reflection amplitude ($r^0_{n,n'}$) data with only propagating waves at f = 43.64 Hz, plotted against (Column index, Line index). Color bar shows the values of dimensionless reflection amplitude $r^0_{n,n'}$.

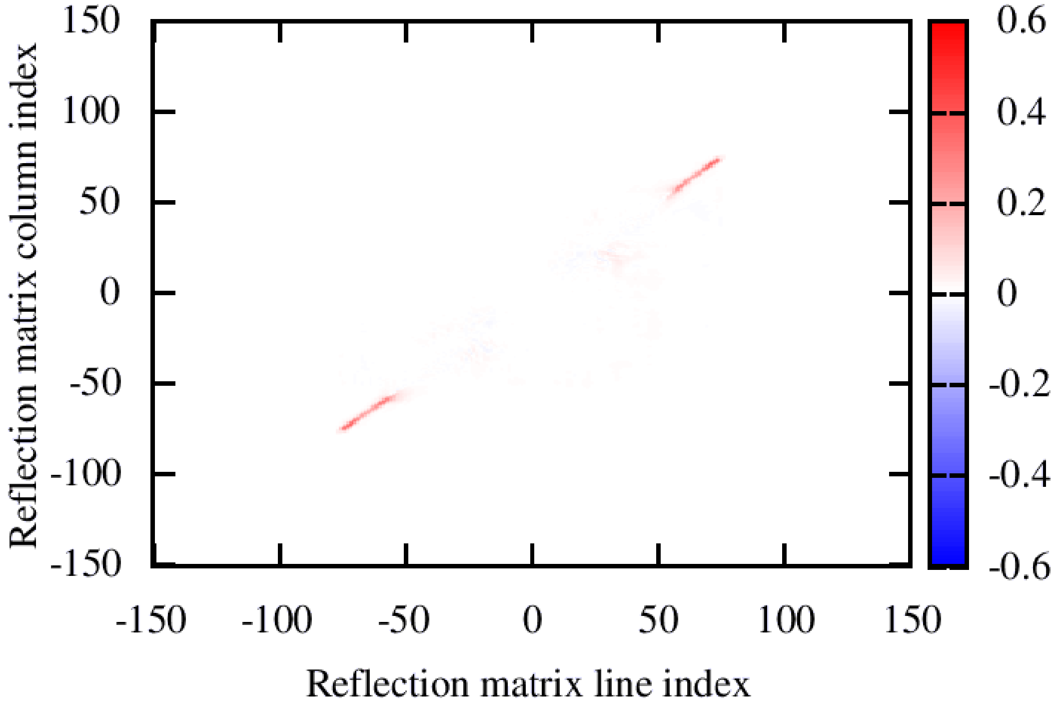

Figure 4.5: Difference of reflection amplitudes $r_{n,n'} - r^0_{n,n'}$ at $f = 43.64$ Hz, plotted against (Column index, Line index). Color bar shows the values of $r_{n,n'} - r^0_{n,n'}$.

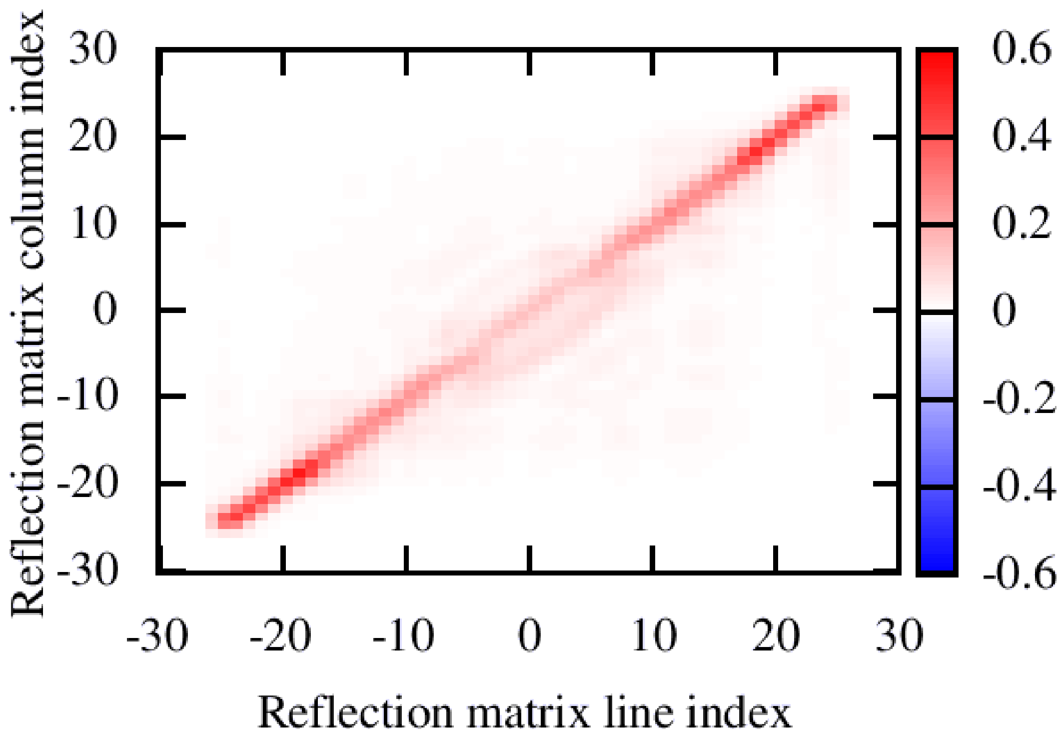

Figure 4.6: Reflection amplitude $\mathbf{r}_{n,n'}$ data with both propagating and decaying evanescent waves at $f = 14.55$ Hz, plotted against (Column index, Line index). Color bar shows the values of dimensionless reflection amplitude $\mathbf{r}_{n,n'}$.

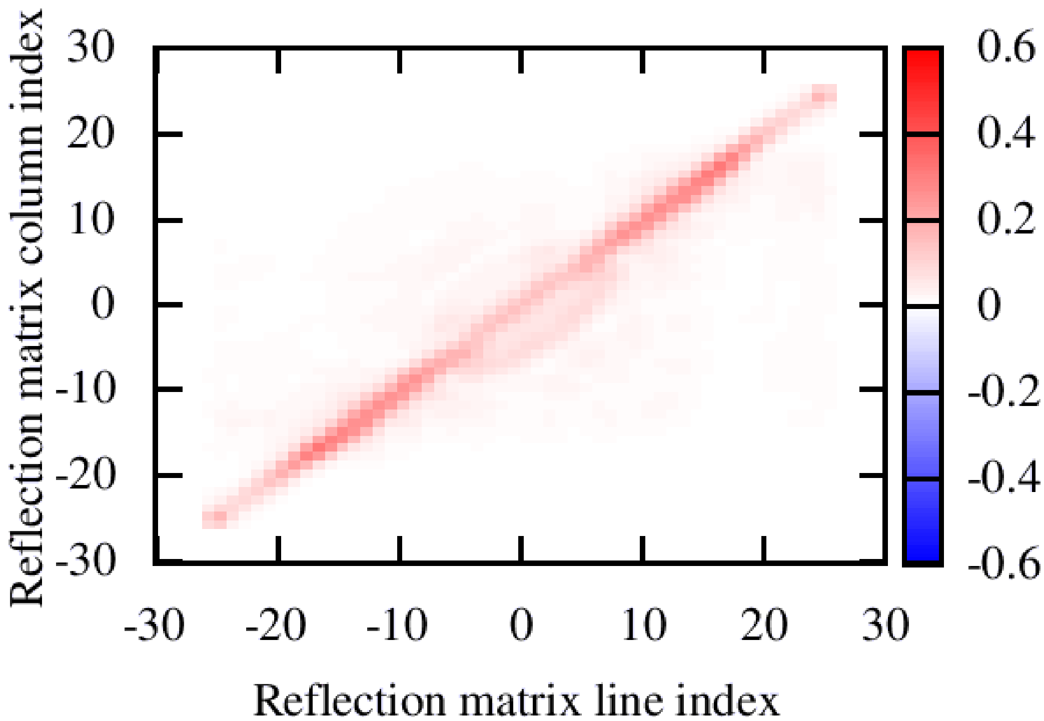

Figure 4.7: Reflection amplitude ($r^0_{n,n'}$) data with only propagating waves at $f =$ 14.55 Hz, plotted against (Column index, Line index). Color bar shows the values of dimensionless reflection amplitude $r^0_{n,n'}$.

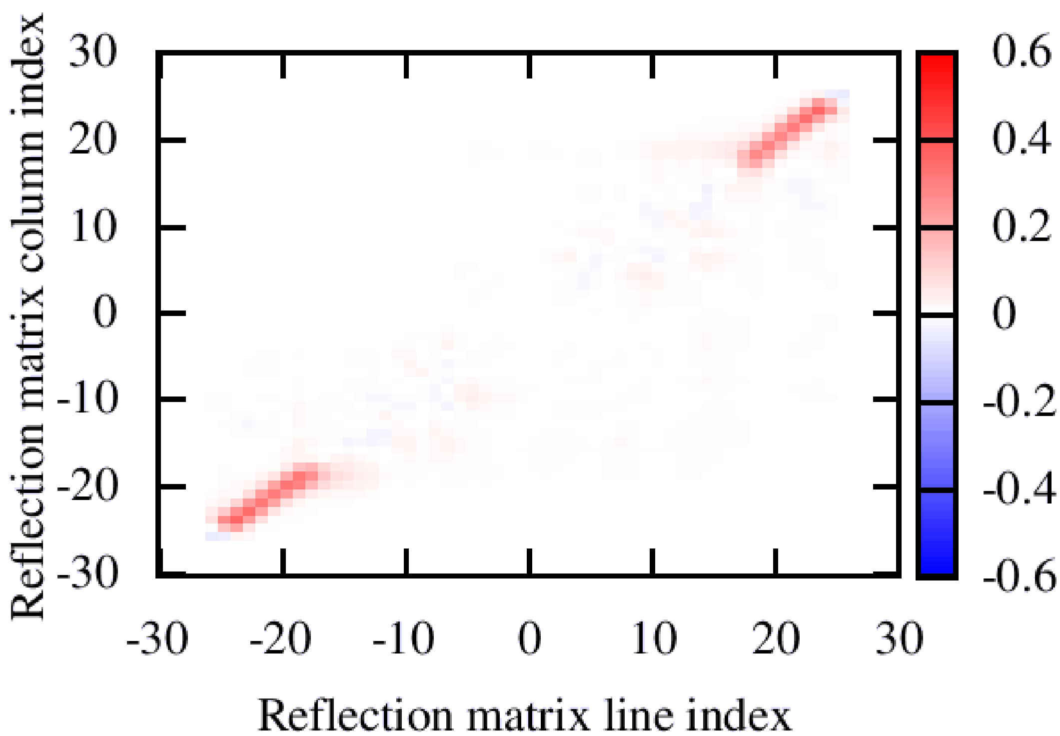

Figure 4.8: Difference of reflection amplitudes $r_{n,n'} - r^0_{n,n'}$ at $f = 14.55$ Hz, plotted against (Column index, Line index). Color bar shows the values of $r_{n,n'} - r^0_{n,n'}$.

Chapter 5

Seismic Imaging Using Volterra Inverse Scattering Series and New FWPS Approach.

5.1 Introduction

Inverse scattering method studies the scattered wavefield measured near the surface to determine the earth's subsurface properties. From the end of 1970s, with the development of inverse scattering research on wave equation, this theory was introduced into the field of seismic exploration. Moses and Prosser [62, 63] first brought forward the inverse scattering series method (ISS). Later, Bleistein and Cohen [64, 65, 66] discussed the relationship between inverse scattering theory and seismic imaging problem.

There are mainly two types of inverse scattering methods: linear approximation methods [67, 64] and optimization methods [68, 69]. Currently, Weglein and co-workers have employed the inverse scattering theory [70], which has a significant advantage in comparison to other data inversion methods (*e.g.,* full waveform inversion [68, 69]). Their work on ISS is based on the early work of Jost and Kohn [71], Moses [62], Razavy [72] and Prosser [63]. The ISS is a direct method for seismic inversion[73]. It uses the Born-Neumann series solution of the acoustic Lippmann-Schwinger equation and requires no prior information of the actual wave propagation in the subsurface. Their approach, however, is limited by the finite radius of convergence of the Born-Neumann series of the acoustic Lippmann Schwinger equation.

Kouri *et al.* [74], have developed a one-dimensional Volterra inverse scattering series (VISS) which possesses advantages over ISS. Also, their method achieves imaging and inversion in one procedure. Their method is inspired by the early work of renormalization transformation of the Lippmann-Schwinger equation into a Volterra equation by Sams and Kouri [38]. In 2003, Kouri and Vijay [75] proposed a method to formulate the acoustic scattering solution in terms of a Volterra kernel to overcome the convergence limitation of the Born-Neumann series solution of the Lippmann-Schwinger integral equation. In their method [75], the inverse series was derived for both reflection and transmission data. Lesage, Jie *et al.* [74], provides the extension of this approach to a more practical case involving only reflection data measured near the surface, which is more useful in the oil and gas industry.

The following section gives a detailed derivation of the Volterra inverse scattering series (VISS) based on the renormalization of the Lippmann-Schwinger equation.

We employ the reflection data computed by the new FWPS approach in VISS to validate seismic imaging. The detailed derivation of computing reflection data based on Volterra Lippmann-Schwinger equations is given in chapter 2.

5.2 Volterra Inverse Scattering Series

The definitions of terms in this section are found in chapter 2. The causal Green's function is given by

$$G^{+}_{0,\omega}(xz|x'z') \equiv G^{+}_{0,\omega} = \frac{-ik^2}{2}\sum_{n_x}\frac{1}{k_{n_x}}\varphi_{n_x}(x)\varphi^{*}_{n_x}(x')e^{ik_{n_x}|z-z'|} \tag{5.1}$$

where $\varphi_n(x)$ are the lateral Fourier basis functions defined by

$$\varphi_n(x) = \frac{e^{2\pi inx/L}}{\sqrt{L}} = \varphi^{*}(-n)(x). \tag{5.2}$$

The Volterra Green's function is given by

$$\widetilde{G}_{0,\omega}(xz|x'z') \equiv \widetilde{G}_{0,\omega} = k^2\sum_{n_x}\frac{1}{k_{n_x}}\varphi_{n_x}(x)\varphi^{*}_{n_x}(x')sin[k_{n_x}(z-z')]\eta(z-z') \tag{5.3}$$

where $\eta(z-z')$ is the Heaviside function. If G is a general Green's function, then

$$Gf \equiv \int_0^L dx'\int_{-\infty}^{\infty} dz' G(xz|x'z')f(x'z'). \tag{5.4}$$

The causal Green's function can be expressed in terms of the Volterra Green's function by adding an (operator) solution of the homogeneous Helmholtz equation:

$$\begin{aligned} G^{+}_{0,\omega} &= \widetilde{G}_{0,\omega} - \frac{ik^2}{2}\sum_{n_x}\frac{1}{k_{n_x}}\varphi_{n_x}(x)\phi_{-k_{n_x}}(z)\varphi^{*}_{n_x}(x')\phi^{*}_{-k_{n_x}}(z') && (5.5)\\ &= \widetilde{G}_{0,\omega} - \frac{ik^2}{2}\sum_{n_x}\frac{1}{k_{n_x}}\varphi_{n_x}\phi_{-k_{n_x}}\varphi^{*}_{n_x}\phi^{*}_{-k_{n_x}}. && (5.6)\end{aligned}$$

The causal solution of the acoustic, frequency domain equation (solution of the LS equation) for the initial incident wave vector can be denoted in an abstract form by the symbol:

$$P_\omega^+(n_x^0, k_{n_x^0}) \tag{5.7}$$

where $k_{n_x^0}$ is the initial incident wave vector. Here, $P_\omega^+(n_x^0, k_{n_x^0})$ is only Fourier expanded in the source position dependence compared to chapter 2. Then the LS equation in Volterra abstract form can be written exactly as

$$\begin{aligned} P_\omega^+(n_x^0, k_{n_x^0}) &= \varphi_{n_x^0}\phi_{k_{n_x^0}} + \widetilde{G}_{0,\omega} V P_\omega^+(n_x^0, k_{n_x^0}) \\ &- \frac{ik^2}{2}\sum_{n_x}\frac{1}{k_{n_x}}\varphi_{n_x}\phi_{-k_{n_x}}\varphi_{n_x}^*\phi_{-k_{n_x}}^* V P_\omega^+(n_x^0, k_{n_x^0}). \end{aligned} \tag{5.8}$$

Equation (5.8) is shown in an abstract form with the integrations are suppressed. The general form of $\widetilde{G}_{0,\omega}$ with the integrations is given in Eqn. (5.4). The complex basis functions $\varphi_{n_x}^*$ and $\phi_{-k_{n_x}}^*$ in last term of Eqn. (5.8) are functions of x' and z' respectively, which also needed to be integrated over. The reflection matrix elements are defined in abstract form by

$$r(n_x, -k_{n_x}|n_x^0, k_{n_x^0}) = -\frac{ik^2}{2k_{n_x}}\varphi_{n_x}^*\phi_{-k_{n_x}}^* V P_\omega^+(n_x^0, k_{n_x^0}). \tag{5.9}$$

Equation (5.8) can be expressed using the reflection matrix elements as

$$\begin{aligned} P_\omega^+(n_x^0, k_{n_x^0}) &= \varphi_{n_x^0}\phi_{k_{n_x^0}} + \widetilde{G}_{0,\omega} V P_\omega^+(n_x^0, k_{n_x^0}) \\ &+ \sum_{n_x}\varphi_{n_x}\phi_{-k_{n_x}} r(n_x, k_{n_x}|n_x^0, k_{n_x^0}). \end{aligned} \tag{5.10}$$

Next, the LS is re-normalized by factoring out the reflection amplitudes. To do this, define

$$P_\omega^+(n_x^0, k_{n_x^0}) = P_{1,\omega}(n_x^0, k_{n_x^0}) + \sum_{n_x} P_{2,\omega}(n_x, -k_{n_x}) r(n_x, -k_{n_x}|n_x^0, k_{n_x^0}). \tag{5.11}$$

By comparing (5.11) and (5.10) we observe

$$\begin{aligned} P_{1,\omega}(n_x^0, k_{n_x^0}) &= \varphi_{n_x^0}\phi_{k_{n_x^0}} + \widetilde{G}_{0,\omega} V P_{1,\omega}(n_x^0, k_{n_x^0}) && (5.12) \\ P_{2,\omega}(n_x, -k_{n_x}) &= \varphi_{n_x}\phi_{-k_{n_x}} + \widetilde{G}_{0,\omega} V P_{2,\omega}(n_x, -k_{n_x}). && (5.13) \end{aligned}$$

We stress that both $P_{2,\omega}(n_x, -k_{n_x})$ and $P_{1,\omega}(n_x^0, k_{n_x^0})$ satisfy Volterra integral equations. The iteration of the Volterra equations, yields

$$\begin{aligned} P_{1,\omega}(n_x^0, k_{n_x^0}) &= \sum_{m=0} (\widetilde{G}_{0,\omega} V)^m \varphi_{n_x^0}\phi_{k_{n_x^0}}, && (5.14) \\ P_{2,\omega}(n_x, -k_{n_x}) &= \sum_{m=0} (\widetilde{G}_{0,\omega} V)^m \varphi_{n_x}\phi_{-k_{n_x}}. && (5.15) \end{aligned}$$

Recalling equations (5.9)-(5.11),

$$\begin{aligned} r(n_x, -k_{n_x}|n_x^0, k_{n_x^0}) &= -\frac{ik^2}{2k_{n_x}} \int_0^L dx' \int_{-\infty}^{\infty} dz' \varphi_{n_x}^* \phi_{-k_{n_x}}^* V[\sum_{m=0} (\widetilde{G}_{0,\omega} V)^m \varphi_{n_x^0}\phi_{k_{n_x^0}} \\ &+ \sum_{n_x}\sum_{m=0} (\widetilde{G}_{0,\omega} V)^m \varphi_{n_x}\phi_{-k_{n_x}} r(n_x, -k_{n_x}|n_x^0, k_{n_x^0})]. && (5.16) \end{aligned}$$

Next, write the perturbation as a sum of orders of the data:

$$V(xz) = \sum_{j=1} V_j(xz). \tag{5.17}$$

The first order results is then

$$r(n_x, -k_{n_x}|n_x^0, k_{n_x^0}) = -\frac{ik^2}{2k_{n_x}} \int_0^L dx' \int_{-\infty}^{\infty} dz' \varphi_{n_x}^* \phi_{-k_{n_x}}^* V_1(x', z') \varphi_{n_x^0}\phi_{k_{n_x^0}} \tag{5.18}$$

It is instructive to consider the first order expression. We now specialize the incident wave vector to be along the positive z axis. Then it follows that:

$$k_0 = k = \frac{\omega}{c_0} \tag{5.19}$$

and equation (5.18) becomes

$$\begin{aligned} r(n_x, -k_{n_x}|0, k_0) &= -\frac{ik^2}{2k_{n_x}} \int_0^L dx' \int_{-\infty}^{\infty} dz' \varphi_{n_x}^* \phi_{-k_{n_x}}^* V_1(x', z') \varphi_0 \phi_{k_0} \\ \phi_0 &= \frac{1}{\sqrt{L}} \end{aligned} \tag{5.20}$$

But we observe that

$$V_{1,n_x}(z') = \int_0^L dx' \varphi_{n_x}^* V_1(x'z') \tag{5.21}$$

Therefore,

$$r(n_x, -k_{n_x}|0, k_0) = -\frac{ik^2}{2k_{n_x}} \int_{-\infty}^{\infty} dz' \phi_{-k_{n_x}}^* V_{1,n_x}(z') \phi_{k_0} / \sqrt{L} \tag{5.22}$$

Therefore, inverse Fourier transforming equation (5.22) yields the n_x Fourier component of V_1. Thus,

$$V_1(xz) = \sum_{n_x} \varphi_{n_x} V_{1,n_x}(z). \tag{5.23}$$

5.3 Computational Results

Figure 5.1 shows the two velocity models $c(x,z)$, we have used to test the imaging or inversion of two-dimensional VISS. Both velocity models present challenging velocity variations in lateral and vertical directions. Figure 5.1(a) is a steep velocity model with slanted layer boundaries. Figure 5.1(b) is a widely used realistic earth velocity model (BP P-wave model) with arbitrarily varying velocities including a salt domain. For both velocity models we have used $dx = 10$ m and dz= 1.5 m as grid spacings. In each case, we have used $2N_x + 1 = 301$ grid points along the x-direction and 601 grid points along the z-direction. For the BP P-wave velocity model, a low velocity part at the bottom has been added to provide compact support in z. Reflection data for the inversion was obtained by new FWPS approach. We have computed $\mathbf{r}_{n',n}(\omega)$ for 500 frequencies lying in a frequency range from $0.001/2\pi$ Hz to $250/2\pi$ Hz with a constant frequency interval $\Delta\omega = 0.5/2\pi$ Hz using new FWPS approach. For these results we have only used the reflection data corresponding to the normally incident waves ($n_x^0 = 0$).

Figure 5.2 compares the velocity perturbation $V(x,z) = 1 - c_0^2/c^2(x,z)$ and VISS first order result $V_1(x,z)$ for the steep velocity model. The amplitude for this case is $V_0 = 0.3$ with $c_0 = 2000.0$ m/s and $c_{max} = 2900$ m/s. As seen in Figure 5.2(b), high accuracy can be observed in the x-direction. The depth of the first reflecting boundary is well predicted while the next reflecting boundary is predicted at an earlier depth than in Figure 5.2(a). There are unwanted artifacts appearing in the sharp boundary of the steep model. When sharp boundaries are present in the the

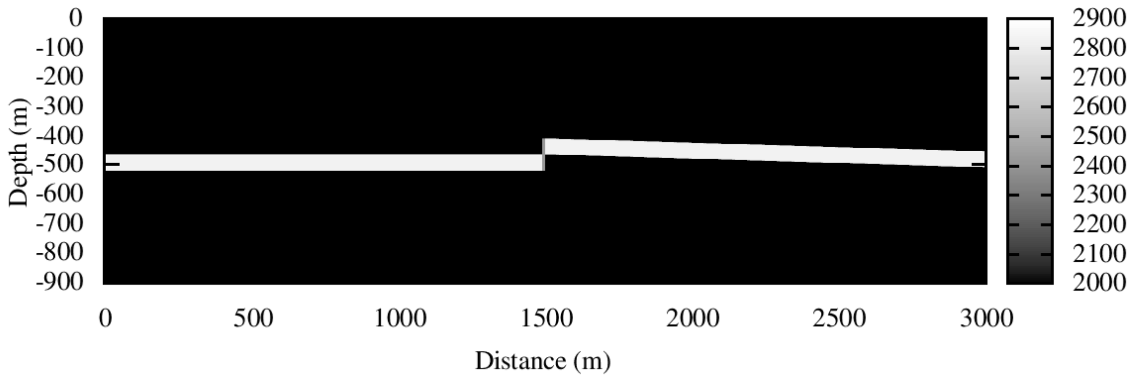

(a)

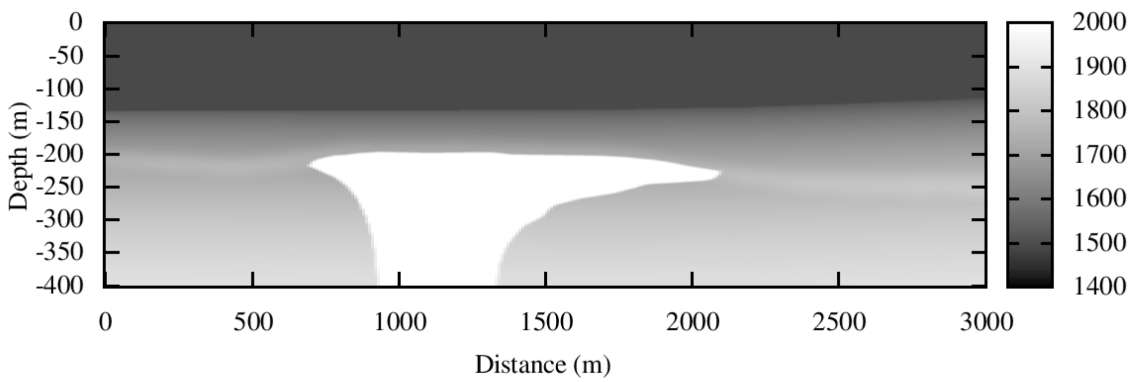

(b)

Figure 5.1: P-wave velocity models. We have plotted the wave velocity against (Depth, Distance). Grayscale bar shows the wave velocity values in m/s. (a) Steep velocity model. (b) BP P-wave velocity model.

velocity perturbation that needs to be inverted, the first order term results in Gibbs oscillations due to the numerical truncation of the Fourier integral (Eqn. 5.22). To filter out the oscillations, we have used the Lanczos averaging method [76]. Therefore, to capture the sharp boundaries, larger frequency ranges have to be used.

Figure 5.3 compares the velocity perturbation $V(x,z) = 1 - c_0^2/c^2(x,z)$ and VISS first order result $V_1(x,z)$ for the BP P-wave velocity model. We have computed $\mathbf{r}_{n',n}(\omega)$ for a reference velocity c_0=1492 m/s using the new FWPS approach. Although the general geological structure is reproduced well, the layer positions are not well predicted. Also the inversion doesn't capture reflector dips having angles larger than 45^0. This is due to the fact that the reflection data used in the inversion corresponds only to the normally incident waves ($n_x^0 = 0$). Figure 5.4 shows the reflection data corresponding to the normally incident waves ($n_x^0 = 0$) for the steep velocity model that were used for the inversion. The high accuracy in the inversion results, is also a good indicator for the accuracy of the FWPS method.

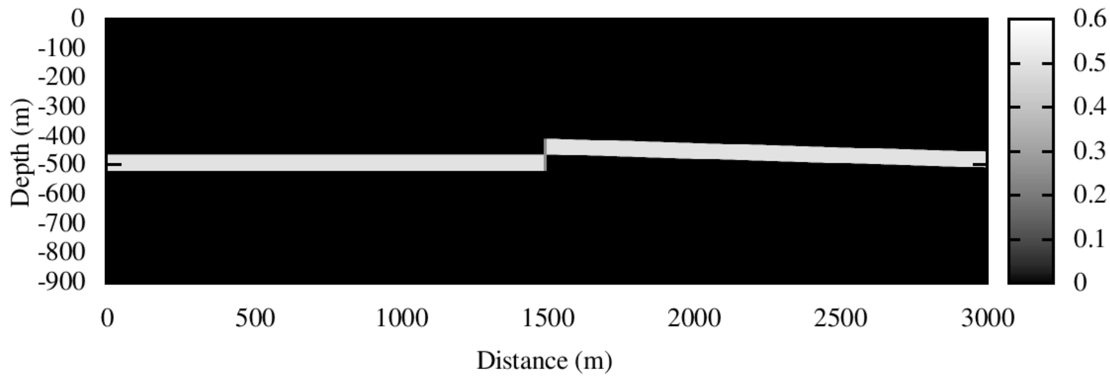

(a)

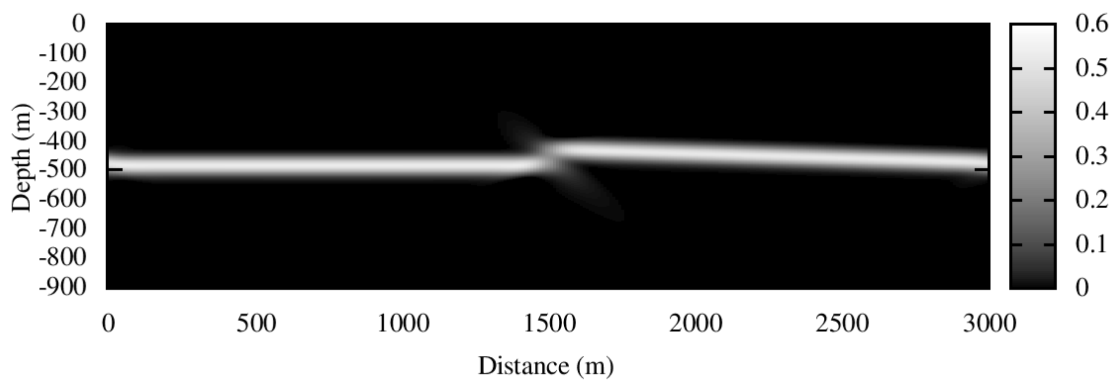

(b)

Figure 5.2: VISS first order result for the steep velocity model plotted against (Depth, Distance). Grayscale bar shows the dimensionless velocity perturbation values. (a) Velocity perturbation $V(x,z) = 1 - c_0^2/c^2(x,z)$ with $c_0 = 2000.0$ m/s and $c_{max} = 2900$ m/s. (b) VISS first order result $V_1(x,z)$.

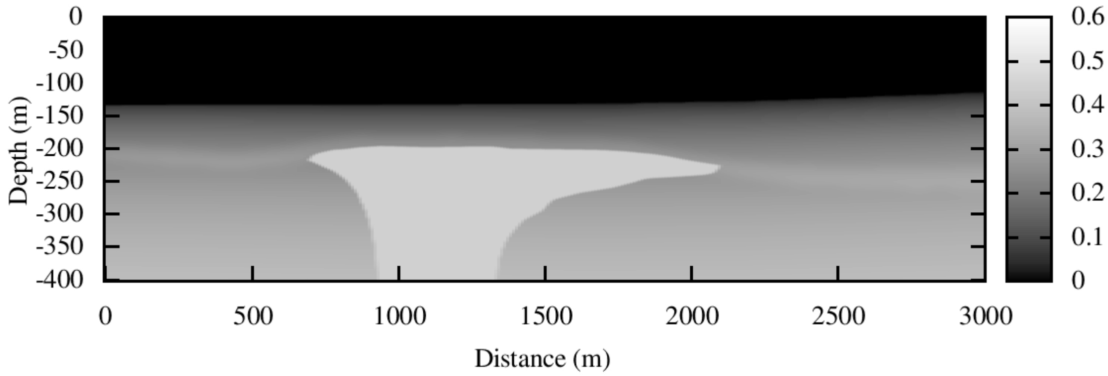

(a)

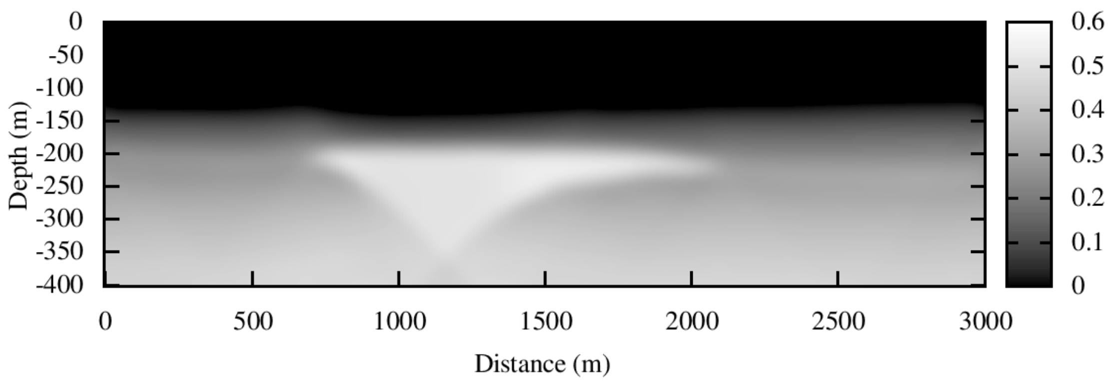

(b)

Figure 5.3: VISS first order result for the BP P-wave velocity model plotted against (Depth, Distance). Grayscale bar shows the dimensionless velocity perturbation values. (a) Velocity perturbation $V(x,z) = 1 - c_0^2/c^2(x,z)$ with $c_0 = 1492.0$ m/s. (b) VISS first order result $V_1(x,z)$.

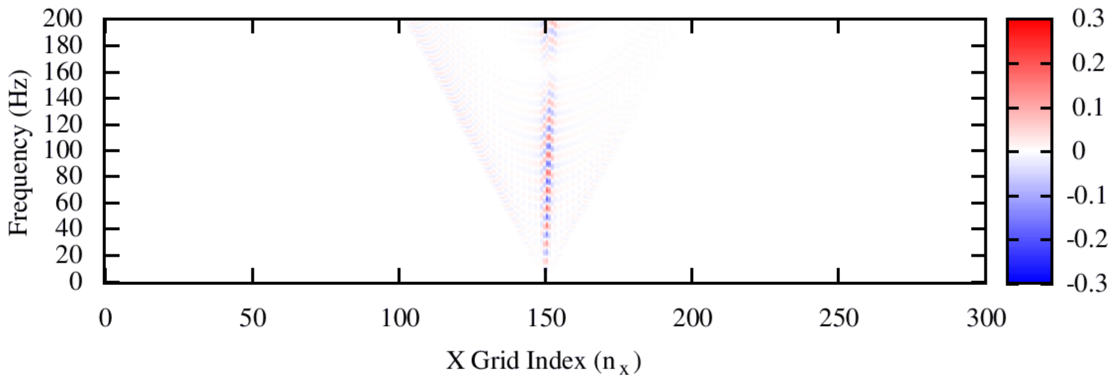

Figure 5.4: Reflection amplitude $\mathbf{r}_{n',n}(\omega)$ plotted against (Frequency, X grid index). Color bar shows the values of dimensionless reflection amplitude $\mathbf{r}_{n',n}(\omega)$. These reflection data correspond to the normally incident waves ($n_x^0 = 0$) at different frequencies.

Chapter 6

Modifications to the New FWPS Approach

6.1 Changing the Reference Velocity with Depth

An important feature of the new FWPS approach is introducing a locally constant reference velocity c_0 and using operator splitting method [42, 43, 44, 77] which leads to an exponential propagator that can be analytically evaluated by phase-shift structure. The complicated remainder of the Helmholtz operator is retained in an inhomogeneous term so that lateral velocity variations can be included. However, there is a major issue concerning the choice of reference velocity (c_0) that is best at any given depth. The initial choice of c_0 is at $z = 0$ is obvious since at that depth, the velocity is homogeneous and remains so for some depth. After some distance, at some depth point z', the acoustic velocity may become inhomogeneous. After that depth point z', the acoustic velocity may not be equal to the initial $c_0(z_0)$ at any point in the subsurface. The result is that the minimum velocity, $c(x, z)$ for $z \geq z'$ will be larger than $c_0(z_0)$. This is indeed the case when dealing with realistic velocity models. For BP P-wave velocity model given in Fig. 3.4(b) the acoustic velocity at the surface of sea level is 1492.0 m/s while inside the salt domain it is 4370.0 m/s, ~2.9 times greater. Therefore, to build an efficient and stable modeling algorithm there should be an effective way to handle these large velocity variations. In the following section we discuss how to modify the new FWPS algorithm to include different reference velocities with depth.

6.1.1 Modifying the Feshbach Projection-operator

We can define a "local wave number" as

$$k(x, z) \;=\; \frac{\omega}{c(x, z)}, \tag{6.1}$$

then evanescent waves or closed channels satisfy

$$\frac{2\pi n_x}{L}^2 \;>\; \frac{\omega^2}{c^2(x, z)}, \tag{6.2}$$

and propagating waves or open channels satisfy

$$\frac{2\pi n_x}{L}^2 \;<\; \frac{\omega^2}{c^2(x, z)}. \tag{6.3}$$

To get best results with a minimum loss of information, we want to choose $c_0(z)$ so as to include all possible propagating components of the pressure at a given depth step z. Consequently, we want to remove the minimum number of growing evanescent waves. Therefore, we need to choose the minimum velocity for that given depth step, resulting in a new reference velocity

$$c_0(z) \quad = \quad min\ c(x,z). \tag{6.4}$$

When the minimum velocity of the given layer $c_0(z)$ exceeds the initial choice of reference velocity $c_0(z_0)$, the number of evanescent waves will clearly increase. Thus, if we continue using the initial $c_0(z_0)$, waves that were propagating up and down become evanescent waves that are either decaying exponentially or growing exponentially. The way a given wave number contributes to the projection-operators Π and $\mathbf{X}$ is solely determined by the value of c_0. Clearly, this defeats the goal of Feshbach projection and hence we need to modify the projection-operators to take account of the dependance on $c_0(z)$ as to which n_x components of the pressure are propagating and which are evanescent.

In our New FWPS approach, we have coupled equations for the z-dependent, n_x components of the pressure

$$\frac{\partial}{\partial z}\mathbf{W} = \mathbf{MW} + \mathbf{VW}, \tag{6.5}$$

$$\mathbf{W} = \begin{pmatrix} \tilde{P} \\ \tilde{Q}, \end{pmatrix} \tag{6.6}$$

$$\tilde{P}_{n_x n'_x} \quad = \quad \tilde{P}_\omega(n_x \mid n'_x \mid z), \tag{6.7}$$

and

$$\tilde{Q}_{n_x n'_x} \quad = \quad \tilde{Q}_\omega(n_x \mid n'_x \mid z). \tag{6.8}$$

The values of n_x range from $-N_x \leq n_x \leq N_x$, so $\tilde{P}$ and $\tilde{Q}$ have $2N_x + 1$ components. Consequently, $\mathbf{W}$ is a $4N_x + 2$ components vector. The projectors Π and $\mathbf{X}$ are matrices. These dimensions are independent of the choice of reference velocity $c_0(z)$. Now we note that the explicit form of Π is

$$\Pi = \begin{pmatrix} \mathbf{I}_1 & 0 \\ 0 & \mathbf{I}_1 \end{pmatrix} + \begin{pmatrix} \frac{1}{2}\mathbf{I}_2 & -\frac{1}{2}\frac{1}{\sqrt{-\frac{\omega^2}{c_0^2}+\left(\frac{2\pi j}{L}\right)^2}}\mathbf{I_2} \\ -\frac{1}{2}\sqrt{-\frac{\omega^2}{c_0^2}+\left(\frac{2\pi j}{L}\right)^2}\,\mathbf{I}_2 & \frac{1}{2}\mathbf{I_2} \end{pmatrix}, \tag{6.9}$$

where $\mathbf{I}_1$ and $\mathbf{I}_2$ are identity operators that only span the imaginary-eigenvalue and real-eigenvalue subspaces respectively. Clearly, the definition of Π and $\mathbf{X}$ depend on the value we assign to c_0. The effect of a specific choice of c_0 is determine which values of n_x obey the propagating or evanescent property and the precise form of Π and $\mathbf{X}$. Therefore, we can change the value of c_0 in the projection matrices and easily construct the projectors $\Pi_{c_0}(z)$ and $\mathbf{X}_{c_0}(z)$, which are now labeled by the value of c_0 at a given depth, z. For every z the form of Π remains the same; only the sizes of $\mathbf{I}_1$ and $\mathbf{I}_2$ change. With the use of modified projection matrix, now we are able to identify the significance of the evanescent waves in realistic earth models.

6.2 Performance of New FWPS Approach Under Parallelization

Seismic wave modeling algorithms used for calculating the seismic response for a given earth model, require large computational resources in terms of speed and memory [78, 79]. Therefore, as supercomputers become more and more powerful, it is very important for computational geoscientists to take advantage of such powerful high performing computer facilities. In the following subsections we describe our parallel implementation of the new FWPS approach to solve the Helmholtz acoustic wave equation in a message passing environment.

6.2.1 Parallelization of New FWPS Code Based on Linearly Independent Solutions

The new FWPS approach requires the solution of $2 \times (2N_x + 1) = 4N_x + 2$ coupled ordinary differential equations, where $2N_x + 1$ is the number of grid points along the x direction. Since the most time consuming part in the algorithm is the computation of propagation $\mathbf{W}(z+\Delta z)$ in the "propagat subroutine", we concentrate on the computational complexity of this step. This computation results in $(4N_x+2)^3$ order scaling due to the computational effort in matrix-matrix multiplications. From the solution to the new FWPS approach

$$\begin{aligned}\Pi(z+\Delta z)\mathbf{W}(z+\Delta z) \;\simeq\; & \Pi(z+\Delta z)\left(\mathbf{I}+\tfrac{\Delta z}{2}\mathbf{V_{Ab}}(z+\Delta z)\right)\Pi(z+\Delta z) \\ & \exp(\Delta z\mathbf{M})\Pi(z)\left(\mathbf{I}+\tfrac{\Delta z}{2}\mathbf{V_{Ab}}(z)\right)\Pi(z)\mathbf{W}(z),\end{aligned} \tag{6.10}$$

it is clearly seen that the solution for each column of $\mathbf{W}(z)$ is linearly independent. Earlier methods used to eliminate the exponentially growing evanescent waves have been a major obstacle in parallelization of the wave propagating algorithms. Feshbach's projection method stabilization has made the new FWPS approach easily parallelizable. We can distribute each column of $\mathbf{W}(z)$ on a different processor and calculate them simultaneously. In this way we can reduce the expensive matrix-matrix multiplication in the propagating equation to a matrix-vector multiplication. Consequently, the computational cost is reduced from $(4N_x+2)^3$ to $(4N_x+2)^2$ for each separate linearly independent solution.

We have used message passing interface (MPI) to parallelize the new FWPS algorithm. It is based on message passing to communicate between processors. A typical method of a parallel job is given below.

```
broadcast data and start job on n processors
do i=1 to j
each processor does some calculation
end do
receive the results of the job
end job
```

In our case we broadcast Π, $\exp(\Delta z\mathbf{M})$, $\mathbf{V}_{Ab}(z)$, $\mathbf{V}_{Ab}(z+\Delta z)$, and $\mathbf{W}(z)$ from the root processor, so they are available on every processor. When each independent matrix-vector computation is done for each column of $\mathbf{W}(z)$ we receive the pressure result for $\mathbf{W}(z+\Delta z)$, where $z+\Delta z$ is the next depth step. There is no need to communicate between the processors while the computation is been done. This is a huge advantage over other algorithms where processors must communicate to achieve the stabilization since in previous methods involved superposing of all the independent solutions was required to remove the exponentially growing evanescent waves.

We have carried out all the calculations on AMD (2.2 GHz) machines using an OpenMPI/1.6.5-Intel compiler. We specified the number of nodes we want to use with processors per node always set to 1. We have also used O3 optimization when compiling the new FWPS algorithm as it provides deeper inner loop unrolling and better loop scheduling. The O3 optimization emphasizes on speed over size; therefore, it can be used when run-time performance is an important factor.

Using the parallelization with respect to independent columns of $\mathbf{W}(z)$, we evaluate the scaling behavior of the new FWPS algorithm. We compare the times to compute the propagation for two different grid sizes of a steep velocity model. In each case the velocity model has the same number of z grid points with $N_z = 601$. The number of x grid points used in test 1 and test 2 are $2N_x+1 = 151$ and $2N_x+1 = 301$, respectively. Those numbers also correspond to the number of Fourier basis set components we used in each test case. Therefore, test 1 and test 2 have 302 $(4N_x+2)$ and 602 linearly independent solutions respectively. According to the $(4N_x+2)^3$

No. of Processors	Time (s) (test1)	Time (s) (test2)
2	549.38	4423.06
4	394.18	1977.82
8	303.16	1182.33
16	255.21	949.38
20	238.75	812.34
21	236.45	714.47
25	235.31	659.38
30	236.69	687.92

Table 6.1: Comparison of performance time for different number of processors. Test 1 and test 2 are for 302 and 602 linearly independent solutions with $N_z = 601$ number of vertical grid points.

order scaling for the non-parallel approach, the ratio of the performance time for propagation for the two test cases should be around 7.92. That means in a single processor test 2 should take 7.92 times performance time as that of test 1. As shown in Table 6.1, the performance time taken by test 2 is about 8.05 times greater than that of test 2 for small number of processors. When we use 21 processors the ratio of performance time is about 3.02. Thus, it indicates that when we increase the number of processors, the total computational time gradually decreases. It also demonstrates the impact of the $(4N_x+2)^2$ order scaling in the new FWPS approach. Our $(4N_x + 2)^2$ scaling behavior of the new FWPS approach can be seen up to 21 processors.

6.2.2 Parallelization Based on Different Frequencies

Another common method of parallelization used in the industry is to divide the frequency range to be computed between the processors. After each processor finishes its frequency set it will send its results to the master processor for output or post-processing. This parallelization is also possible for the new FWPS approach. In this method , we calculate $\mathbf{W}(z)$ values by sending sets of frequencies to different processors. We have also applied frequency based parallelization to our new FWPS approach and have verified its performance . Table 6.2 compares the times to compute the propagation for two different frequency ranges of a steep velocity model. In each case the velocity model has the same grid size with $N_x = 150$ and $N_z = 601$. The number of frequencies used in test 1 and test 2 are 40 and 80, respectively. Data in table 6.2 shows a speedup as we increase the number of processors. For a fixed model size the computational time decreases with the increase in the number of processors. Therefore, if we increase the size of the problem, better speedup can be achieved for large number of processors.

No. of Processors	Time (h:mn:s) (test1)	Time (h:mn:s) (test2)
2	09:38:13	21:59:08
4	10:36:10	19:08:41
8	04:26:30	09:16:35
16	03:27:54	06:04:53
20	04:27:34	05:59:50

Table 6.2: Comparison of performance time for different number of processors. Test 1 and test 2 are for 40 and 80 frequencies respectively.

6.3 Computation of the Perturbation Matrix $V_{n,n'}$

To calculate the solution to the $\mathbf{W}(\mathbf{z}+\Delta\mathbf{z})$, initially we must compute the perturbation matrix terms $\mathbf{V}$ in the Fourier basis expansion. This will give us the following result

$$\begin{aligned}\frac{1}{L}\int_0^L dx e^{-2\pi inx/L}\left(\mathbf{V}\right)e^{2\pi in'x/L} &= \frac{1}{L}\int_0^L dx e^{-2\pi inx/L}\left(\frac{\omega^2}{c_0^2}-\frac{\omega^2}{c^2(x,z)}\right)e^{2\pi in'x/L} \\ &= \omega^2\left(S_0\delta_{nn'}-\sum_{n''=-N_x}^{N_x}\frac{S_{n''}}{\sqrt{L}}\delta_{n,n''+n'}\right) \qquad (6.11)\end{aligned}$$

where

$$S_n=\frac{1}{\sqrt{L}}\int_0^L dx\frac{\exp(-2\pi inx/L)}{c^2(x,z)}. \qquad (6.12)$$

According to the structure of $\mathbf{V}$ in Eqn 2.46, we only need to calculate the lower left submatrix terms as rest of the terms in the matrix are zero:

$$\mathbf{V}=\begin{pmatrix} 0 & 0 \\ \left[\frac{\omega^2}{c_0^2}-\frac{1}{c^2}\left(\omega^2-\gamma^2+i2\omega\gamma\right)\right] & 0\end{pmatrix}. \qquad (6.13)$$

From now on we refer to this submatrix as $\mathbf{V}_{n,n'}$. Here n and n' both run from $-2N_x$ to $2N_x$, yielding a $(2N_x+1)\times(2N_x+1)$ matrix for $\mathbf{V}_{n,n'}$. In the original new FWPS source code, calculation for $\mathbf{V}_{n,n'}$ was done by using loops over n, n' and n'', having $(2N_x+1)^2$ operations to calculate S_n and $\mathbf{V}_{n,n'}$.

We have identified $\mathbf{V}_{n,n'}$ to have a special form with constant diagonal terms. In linear algebra, such a matrix is called a Toeplitz matrix or diagonal-constant matrix. Each descending diagonal from left to right in a Toeplitz matrix is constant. For instance the following matrix is a Toeplitz matrix:

$$V = \begin{pmatrix} v_0 & v_{-1} & v_{-2} & \cdots & \cdots & v_{-n+1} \\ v_1 & v_0 & v_{-1} & \ddots & \ddots & \vdots \\ v_2 & \ddots & \ddots & \ddots & \ddots & \vdots \\ \vdots & \ddots & \ddots & \ddots & v_{-1} & v_{-2} \\ \vdots & \ddots & \ddots & v_1 & v_0 & v_{-1} \\ v_{n-1} & \cdots & \cdots & v_2 & v_1 & v_0 \end{pmatrix}. \tag{6.14}$$

By using this fact, we have introduced a new computing scheme for $\mathbf{V}_{n,n'}$, which only includes $(4N_x + 1) \times (2N_x + 1)$ operations. Since $\mathbf{V}_{n,n'}$ is a Toeplitz matrix, then that matrix has only $2 \times (2N_x + 1) - 1 = 4Nx + 1$ degrees of freedom, reducing the number of operations from $(2N_x + 1)^2$ to $4Nx + 1$. Therefore, we have made the computation of $\mathbf{V}_{n,n'}$ matrix fairly easier and also faster than in the original new FWPS source code.

Chapter 7

Conclusion

In conclusion, the snapshot results and inversion results reported in this dissertation provide compelling evidence that new FWPS approach provides a phase-shift based solution to the full acoustic wave equation. It provides accurate travel times and treats the reflector locations in complex geologic structures correctly, providing kinamatically correct results comparable to FD method. Comparing the snapshot results from Fig. 3.9(a) to Fig. 3.9(d) with Fig. 3.10(a) to Fig. 3.10(d), we can clearly see that the unwanted artifacts are effectively removed using the absorbing boundary conditions, providing a much clearer snapshots.

For the first time, we were able apply new FWPS approach to a realistic earth model. The snapshot results from Fig. 3.12(a) to Fig. 3.12(c) for the BP P-wave model are very encouraging and provide further evidence of the validity of the new FWPS approach. We also modified the use of the Feshbach projection operator so that minimum information is lost when removing the growing evanescent waves.

The new Feshbach projection operator is computed by using the minimum velocity of each separate layer, which is very useful when dealing with realistic velocity models. We were also able to apply a good parallelization scheme to the new FWPS algorithm based on the linearly independent solutions. Earlier methods used to eliminate the exponentially growing evanescent waves have been a major obstacle in parallelization of the wave propagating algorithms but Feshbach's projection operator stabilization has made the new FWPS approach easily parallelizable. While our method is computationally somewhat expensive compared to some similar, but approximate techniques, the quality of the results justifies the effort to develop the new FWPS algorithm for modeling and inversion.

We are currently improving the new FWPS source code to have better optimization in terms of speed by investigating the use of other parallelization methods such as OpenMP. The plan is to develop our approach further and work on making our algorithm competitive with other modeling and imaging methods in terms of speed. We are also carrying out modifications to the FWPS algorithm to include higher order quadrature methods such as Simpson's rule to increase the step size in depth variable z. We also note that extending the new FWPS results to three-dimensional acoustic case is straightforward and it can be done by including another Fourier basis function $\frac{\exp(2\pi i n_y y/L_y)}{\sqrt{L_y}}$ to describe wave motion along the y direction. Finally, the the methods and results on the thesis could benefit not only seismic physics but also other physics fields such as quantum physics and optics.

Bibliography

[1] R. E. Sheriff and L. P. Geldart, *Exploration Seismology.* Cambridge University Press, 2 ed., Aug. 1995.

[2] New York Frac Facts, "Exploration." http://nyfracfacts.org/what-is-hydrofracking/what-happens-before/, 2012. [Online; accessed 05-March-2014].

[3] Wikipedia, "Reflection seismology." http://en.wikipedia.org/wiki/Reflection_seismology, 2012. [Online; accessed 05-March-2014].

[4] L. Santos, J. Schleicher, M. Tygel, and P. Hubral, "Seismic modeling by demigration," *Geophysics*, vol. 65, no. 4, pp. 1281–1289, 2000.

[5] O. Yilmaz, *Seismic Data Processing.* SEG Publishing, Tulsa, OK, 1987.

[6] N. D. Gray, S. H. Whitmore, and A. Gersztenkorn, "Two-dimensional post-stack depth migration - a survey of methods: First break," vol. 06, no. 06, pp. 189–197, 1988.

[7] G. H. F. Gardner and S. of Exploration Geophysicists (U.S.), *Migration of seismic data.* Tulsa, OK, Society of Exploration Geophysicists, 1985.

[8] J. M. Carcione, G. C. Herman, and A. P. E. Kroode, "Seismic modeling," *Geophysics*, vol. 67, no. 4, pp. 1304–1325, 2002.

[9] V. Cerveny, *Seismic Ray Theory*. Cambridge University Press, 2005.

[10] J. Claerbout, "Toward a unified theory of reflector mapping," *Geophysics*, vol. 36, no. 3, pp. 467–481, 1971.

[11] J. F. Claerbout, *Imaging the Earth's Interior*. Cambridge, MA, USA: Blackwell Scientific Publications, Inc., 1985.

[12] J. K. Cohen, F. G. Hagin, and N. Bleistein, "Three-dimensional born inversion with an arbitrary reference," *Geophysics*, vol. 51, pp. 1552–1558, 1986.

[13] A. B. Weglein, F. V. Araújo, P. M. Carvalho, R. H. Stolt, K. H. Matson, R. T. Coates, D. Corrigan, D. J. Foster, S. A. Shaw, and H. Zhang, "Inverse scattering series and seismic exploration," *Inverse Problems*, vol. 19, no. 6, p. R27, 2003.

[14] Z. Alterman and F. C. Karal, "Propagation of elastic waves in layered media by finite difference methods," *Bulletin of the Seismological Society of America*, vol. 58, no. 1, pp. 367–398, 1968.

[15] J. Virieux, "P-sv wave propagation in heterogeneous media: Velocitystress finitedifference method," *Geophysics*, vol. 51, no. 4, pp. 889–901, 1986.

[16] T. J. R. Huygens, *The finite element method*. Prentice-Hall Intenational Inc., 1987.

[17] K. J. Marfurt, "Accuracy of finite-difference and fnite-element modeling of the scalar and elastic wave equations," *Geophysics*, vol. 49, pp. 533–549, 1984.

[18] M. K. Sen and J. D. D. Basabe, "New developments in the finite-element method for seismic modeling," *Geophysics*, vol. 28, no. 5, pp. 562–567, 2009.

[19] J. Gazdag, "Modeling of the acoustic wave equation with transform methods," *Geophysics*, vol. 46, no. 6, pp. 854–859, 1981.

[20] D. D. Kosloff and E. Baysal, "Forward modeling by a fourier method," *Geophysics*, vol. 47, no. 10, pp. 1402–1412, 1982.

[21] H. Gjoystdal, E. I. Einar, I. Lecomte, T.Kaschwich, A. Drottning, and J. Mispel, "Improved applicability of ray tracing in seismic acquisition, imaging, and interpretation," *Geophysics*, vol. 72, no. 5, p. SM261, 2007.

[22] R. Laurain, L. J. Gelius, V. Vinje, and I.Lecomte, "A review of illumination studies," *Journal of Seismic Exploration*, vol. 13, p. 1734, 2004.

[23] J. O. A. Robertsson, B. Bednar, J. Blanch, C. Kostov, and D.-J. van Manen, "Introduction to the supplement on seismic modeling with applications to acquisition, processing, and interpretation," *Geophysics*, vol. 72, no. 5, pp. SM1–SM4, 2007.

[24] S. Gray, J. Etgen, J. Dellinger, and D. Whitmore, "Seismic migration problems and solutions," *Geophysics*, vol. 66, no. 5, pp. 1622–1640, 2001.

[25] C. Chopra and S. Sayers, "Improved applicability of ray tracing in seismic acquisition, imaging, and interpretation," *Introduction to special section: Seismic modeling. The Leading Edge*, no. 28, pp. 528–529, 2009.

[26] A. J. Berkhout, "Wave field extrapolation techniques in seismic migration; a tutorial," *Geophysics*, vol. 46, no. 12, pp. 1638–1656, 1981.

[27] D. Bevc and B. Biondi., "Which depth imaging method should we use? A road map in the maze of 3-d depth imaging," *Expl. Geophys., Expanded Abstracts,72nd Ann. Internat. Mtg., Soc. of Expl. Geophys.*, pp. 1236–1239, 2002.

[28] J. Gazdag and P. Sguazzero, "Migration of seismic data by phase shift plus interpolation," *Geophysics*, vol. 49, no. 2, pp. 124–131, 1984.

[29] P. L. Stoffa, J. T. Fokkema, R. M. de Luna Freire, and W. P. Kessinger, "Split-step fourier migration," *Geophysics*, vol. 55, no. 4, pp. 410–421, 1990.

[30] G. F. Margrave and R. J. Ferguso, "Wavefield extrapolation by nonstationary phase shift:," *Geophysics*, vol. 64, pp. 1067–178, 1999.

[31] J. Shragge, "Riemannian wavefield extrapolation: Nonorthogonal coordinate systems," *Geophysics*, vol. 73, no. 2, pp. T11–T21, 2008.

[32] S. M. Al-Saleh, G. F. Margrave, and S. H. Gray, "Direct downward continuation from topography using explicit wavefield extrapolation," *Geophysics*, vol. 74, no. 6, pp. S105–S112, 2009.

[33] J. Gazdag, "Wave equation migration with the phaseshift method," *Geophysics*, vol. 43, no. 7, pp. 1342–1351, 1978.

[34] D. Kosloff and D. Kessler, "Accurate depth migration by a generalized phaseshift method," *Geophysics*, vol. 52, no. 8, pp. 1074–1084, 1987.

[35] D. D. Kosloff and E. Baysal, "Migration with the full acoustic wave equation," *Geophysics*, vol. 48, no. 6, pp. 677–687, 1983.

[36] H. Tal-Ezer, "Spectral methods in time for hyperbolic equations," *SIAM Journal on Numerical Analysis*, vol. 23, no. 1, pp. 11–26, 1986.

[37] K. Maji, F. Gao, S. K. Abeykoon, and D. J. Kouri, "New full-wave phase-shift approach to solve the helmholtz acoustic wave equation for modeling," *Geophysics*, vol. 77, no. 1, pp. T11–T27, 2012.

[38] W. N. Sams and D. J. Kouri, "Noniterative solutions of integral equations for scattering. i. single channels," *The Journal of Chemical Physics*, vol. 51, no. 11, pp. 4809–4814, 1969.

[39] W. N. Sams and D. J. Kouri, "Noniterative solutions of integral equations for scattering. ii. coupled channels," *The Journal of Chemical Physics*, vol. 51, no. 11, pp. 4815–4819, 1969.

[40] R. S. Judson, D. B. McGarrah, O. A. Sharafeddin, D. J. Kouri, and D. K. Hoffman, "A comparison of three timedependent wave packet methods for calculating electron–atom elastic scattering cross sections," *The Journal of Chemical Physics*, vol. 94, no. 5, pp. 3577–3585, 1991.

[41] H. Feshbach, "A unified theory of nuclear reactions. {II}," *Annals of Physics*, vol. 19, no. 2, pp. 287–313, 1962.

[42] A. Arnold and C. Ringhofer, "Operator splitting methods applied to spectral

descritizations of quantum transport equations," *SIAM*, vol. 32, pp. 1876–1894, 1995.

[43] M. Thalhammer, "High-order exponential operator splitting meyhods for time dependant scrondinger equations," *SIAM*, vol. 46, pp. 2022–2038, 2008.

[44] R. S.Judson, D. B. McGarrah, O. A. Sharafeddin, D. K. Hoffman, and D. J. Kouri, "A comparison of three time-dependent wave packet methods for calculating electron-atom elastic scattering cross sections," *Journal of Chemical Physics*, vol. 94, pp. 3577–3585, 1991.

[45] T. A. Newton, "A simple algorithm for finding eigenvalues and eigenvectors for 2*2 matrices," *American Mathematical Monthly*, vol. 97, pp. 57–60, 1990.

[46] C. Moler, , and C. V. Loan, "Nineteen dubious ways to compute the exponential of a matrix," *SIAM Review*, vol. 94, pp. 801–836, 1978.

[47] E. R. Smith and R. J. W. Henry, "Non iterative integral-equation approach to scattering problems," *Physical Review A*, vol. 7, pp. 1585–1590, 1973.

[48] R. Kosloff and D. Kosloff, "Absorbing boundaries for wave propagation problems," *Journal of Computational Physics*, vol. 63, pp. 363–376, 1986.

[49] K. Aki and P. G. Richards, *Quantitative Seismology.* W. H. Freeman and Co., 2 ed., 1980.

[50] W. N. Sams and D. J. Kouri, "Noniterative solutions of integral equations for scattering. iii. coupled open and closed channels and eigenvalue problems," *Journal of Chemical Physics*, vol. 52, pp. 4114–4118, 1970.

[51] J. Lysmer and G. Kuhlemeyer, "Finite dynamic model for infinite media," *American Society of Civil Engineers*, vol. 95, no. EM4, pp. 859–877, 1969.

[52] J. Lysmer and G. Wass, "Shear wave in plane infinite structure," *American Society of Civil Engineers*, vol. 98, no. EM1, pp. 85–105, 1972.

[53] W. D. Smith, "A nonreflecting plane boundary for wave propagation problems," *Journal of Computational Physics*, vol. 15, pp. 492–503, 1974.

[54] R. G. Keys, "Absorbing boundary conditions for acoustic media," *Geophysics*, vol. 50, pp. 892–902, 1985.

[55] C. J. Randall, "Absorbing boundary conditions for the elastic wave equation," *Geophysics*, vol. 53, pp. 611–624, 1981.

[56] R. L. Higdon, "Absorbing boundary conditions for elastic waves," *Geophysics*, vol. 56, pp. 231–241, 1991.

[57] R. Courant, K. Friedriches, and H. Lewy, "On the partial difference equations of mathematical physics," *IBM Journal of Research and Development*, pp. 215–234, 1967.

[58] F. A. Vivas and R. C. Pestana, "True-amplitude one-way wave equation migration in the mixed domain," *Geophysics*, vol. 75, no. 5, pp. S199–S209, 2010.

[59] Y. Zhang, "The theory of true amplitude one-way wave equation migrations," *Chinese Journal of Geophysics*, vol. 49, pp. 1121–1424, 2006.

[60] S. H. Gray, "True-amplitude seismic migration:a comparison of three approaches," *Geophysics*, vol. 62, no. 3, pp. 929–936, 1997.

[61] K. Sandberg and G. Beylkin, "Full-wave-equation depth extrapolation for migration," *Geophysics*, vol. 74, no. 6, pp. wca121–wca128, 2009.

[62] H. E. Moses, "Calculation of scattering potential from reflection coefficients," *Phys. Rev.*, vol. 102, pp. 559–567, 1956.

[63] R. T. Prosser, "Formal solutions of inverse scattering problems," *Math. Phys.*, vol. 10, pp. 1819–1822, 1969.

[64] J. K. Cohen and N. Bleistein, "An inverse method for determining small variations in propagation speed," *SIAM Journal on Applied Mathematics*, vol. 32, no. 4, pp. 784–799, 1977.

[65] J. K. Cohen and N. Bleistein, "Velocity inversion procedure for acoustic waves," *Geophysics*, vol. 44, no. 6, pp. 1077–1087, 1979.

[66] N. Bleistein, J. K. Cohen, and F. G. Hagin, "Computation and asymptotic of velocity inversion," *Geophysics*, vol. 47, no. 11, pp. 1497–1511, 1982.

[67] R. Clayton and R. Stolt, "A born-wkbj inversion method for acoustic reflection data," *Geophysics*, vol. 46, no. 11, pp. 1559–1567, 1981.

[68] A. Tarantola, "Inversion of seismic reflection data in the acoustic approximation," *Geophysics*, vol. 49, pp. 1259–1266, 1984.

[69] R. G. Pratt, "Seismic waveform inversion in the frequency domain, part 1: Theory and verification in a physical scale model," *Geophysics*, vol. 66, pp. 888–901, 1999.

[70] A. B. Weglein, F. V. Araujo, and P. M. Carvalho, "Inverse scattering series and seismic exploration," *Inverse Problems*, vol. 19, pp. R23–R83, 2003.

[71] R. Jost and W. Kohn, "Construction of a potential from a phase shift," *Phys. Rev.*, vol. 87, pp. 977–992, 1952.

[72] M. Razavy, "Determination of the wave velocity in an inhomogeneous medium from the reflection coefficient," *J. Acoust. Soc. Am.*, vol. 58, pp. 956–957, 1975.

[73] A. Weglein, "A timely and necessary antidote to indirect methods and so-called p-wave fwi," *The Leading Edge*, vol. 32, no. 10, pp. 1192–1204, 2013.

[74] J. Yao, A. C. Lesage, B. J. Bodmann, F. Hussain, and D. J. Kouri, "Direct nonlinear inversion of acoustic media using volterra inverse scattering series. i. one dimensional data," *submitted to Geophysics*.

[75] D. J. Kouri and A. Vijay, "Inverse scattering theory: Renormalization of the lippmann-schwinger equation for acoustic scattering in one dimension," *Phys. Rev. E*, vol. 67, no. 4, p. 046614, 2003.

[76] B. I. Yun, H. C. Kim, and K. S. Rim, "An averaging method for the fourier approximation to discontinuous functions," *Applied Mathematics and Computation*, vol. 183, pp. 272–284, 2006.

[77] M. D. Feit and J. A. F. Jr., "Solution of the schrödinger equation by a spectral method ii: Vibrational energy levels of triatomic molecules," *Journal of Chemical Physics*, vol. 78, pp. 301–308, 1983.

[78] S. Phadke and D. Bhardwaj, “Parallel implementation of seismic modelling algorithms on param openframe,” *Neural, Parallel and Scientific Computation*, vol. 6, no. 4, pp. 469–478, 1998.

[79] S. Phadke, D. Bhardwaj, and S. Yerneni, “3d seismic modeling in a message passing environment,” in *Proceedings of 3 rd Conference and Exposition on Petroleum Geophysics (SPG 2000)*, pp. 168–172, 2000.